ΠΑΝΕΠΙΣΤΗΜΙΟ ΚΡΗΤΗΣ

ΣΧΟΛΗ ΘΕΤΙΚΩΝ ΚΑΙ ΤΕΧΝΟΛΟΓΙΚΩΝ ΕΠΙΣΤΗΜΩΝ

ΤΜΗΜΑ ΜΑΘΗΜΑΤΙΚΩΝ

ΔΙΔΑΚΤΟΡΙΚΗ ΔΙΑΤΡΙΒΗ

Ασθενεις Λυσεις Ιξωδους Για Μη Γραμμικες Διαφορικες Εξισωσεις Με Μερικες Παραγωγους Και Εφαρμογες– Τρισδιαστατη Αναδομηση Εικονας

Χρηστος Ζωχιος

Επιβλέπων Καθηγητής: ΓΕΩΡΓΙΟΣ ΚΟΣΙΩΡΗΣ

ΗΡΑΚΛΕΙΟ, ΔΕΚΕΜΒΡΙΟΣ 2010

UNIVERSITY OF CRETE

SCHOOL OF SCIENCE AND ENGINEERING

DEPARTMENT OF MATHEMATICS

Ph. D. Thesis

Viscosity Solutions For Nonlinear Partial Differential Equations And Applications– Three-Dimensional Image Reconstruction

Christos Zohios

Thesis Advisor: GEORGIOS KOSSIORIS

HERAKLION, DECEMBER 2010

Committees

Thesis Committee

- Georgios Kossioris (advisor): Associate Professor, Dept. of Mathematics, Univ. of Crete
- Panagiotis Kaklis: Professor, Dept. of Naval Architecture and Marine Engineering, NTUA
- Alkis Tersenov: Professor, Dept. of Mathematics, Univ. of Crete

Thesis defense Committee

- Georgios Kossioris (advisor): Associate Professor, Dept. of Mathematics, Univ. of Crete
- Panagiotis Kaklis: Professor, Dept. of Naval Architecture and Marine Engineering, NTUA
- Alkis Tersenov: Professor, Dept. of Mathematics, Univ. of Crete
- Theodoros Katsaounis: Associate Professor, Dept. of Applied Mathematics, Univ. of Crete
- Markos Katsoulakis: Professor, Dept. of Applied Mathematics, Univ. of Crete
- Georgios Makrakis: Associate Professor, Dept. of Applied Mathematics, Univ. of Crete
- Georgios Zouraris: Assistant Professor, Dept. of Mathematics, Univ. of Crete

To Polina

Acknowledgements

This thesis could not have been accomplished without the assistance of many people, whose contributions I gratefully acknowledge.

I am grateful to my thesis advisor, Prof. G. Kossioris, for his valuable suggestions and advice, some of which were crucial, in moments when all gates to the next step seemed to be closed. Our discussions for a wide range of subjects helped me a lot, in many aspects. Also I would like to thank the other two members of the thesis committee, Prof. P. Kaklis and Prof. A. Tersenov for their helpful remarks, as well as all the members of the thesis defense committee. Their friendly suggestions for my future at the end of the presentation concerning thesis defense mean a lot to me.

I want to express my gratitude to Yannis Papaharilaou, researcher at the Institute of Applied and Computational Mathematics, FORTH, and co-author in one of the two papers produced from this research, for helping me a lot to become familiar with Medical Imaging and aneurysms, a world totally unknown to me until then. He also introduced me with the related software, which was of high importance to this work. I wish to thank Prof. G. Zouraris, Prof. M. Karavelas and Prof. A. Katsamouris for the helpful discussions and suggestions. Some of the methods concerning the image segmentation part of the thesis would not have been made without their inspired thoughts. Moreover, I would like to thank E. Georgakarakos from the Department of Vascular Surgery of PAGNI for providing the data sets and manual segmentations used in the experiments.

I owe my deepest gratitude to all the professors of the Department of Mathematics of University of Crete that firstly introduced me to the exciting world of higher mathematics and then encouraged me to go a step further. Their offices were always open for questions and discussion, making the "ship" of this "trip", which lasted over a decade, very hospitable.

This thesis and many other things of my life would not have been possible without the help of my parents, Evangelos and Despoina. They were and are there for me when I need them and the least I can do is to thank them. A special thank you should go to my brother, Makis, whose advice, usually given in a light-hearted way, are always extremely valuable. His experience in writing a Ph. D. thesis helped me a lot. Talking about a brother, I think this is the right moment to thank Giannis. As true friendship is quite rare in our days, Giannis comes to break this rule. Our long discussions, great laughs, his positive thinking, support, friendly suggestions (some of them concerning viscosity solutions) are only a few of the things for which I owe him a big thank you. I would also like to thank Mihalis, Andreas, George and Dimitris for their care and support, although

distance didn't allow us to meet often, during these years.

I try to think which expression should I use to thank Polina, my wife and constant support in this trip. I can't find any, as sometimes, like in this case, words are not enough. I am sure I would not have completed this project if she hadn't been in my life. And if this thesis hadn't been in my life, I wouldn't have met her! The journey is more important than the destination in so many aspects...

I would like to thank the Greek General Secretariat for Research and Technology and the Greek State Scholarships Foundation (IKY) for funding this work. Lastly, I offer my regards to all of those who supported me in any respect during the completion of this project.

This project was funded by the PENED 2003 Programme of the EU and the Greek General Secretariat for Research and Technology. Initial research was funded by a grant from IKY, the Greek State Scholarships Foundation. I would also like to acknowledge partial funding from the Greek General Secretariat for Research and Technology under the research project "Pythagoras 2003".

Abstract

Viscosity solutions are a class of generalized solutions of nonlinear partial differential equations. The great value of this kind of weak solutions is the fact that very general existence, uniqueness and stability results hold for them in many problems of various fields of application. They are used in many kinds of applications, two of which are analyzed in this work.

The Shallow Lake Problem, a non-standard optimal control problem derived from the combination of agricultural activities and ecological services that a shallow lake provides, is the first application studied. The optimal dynamics of the problem, necessary conditions of which are provided by the Pontryagin Maximum Principle, are studied in the beginning for a range of values of the discount factor. The number and the type of the equilibrium points are also investigated. We then prove that the value function of the Shallow Lake Problem is a viscosity solution of an Optimal Hamilton-Jacobi-Bellman (OHJB) equation, a basic for the rest of this work result. To derive this, we study the control problem on a compact control space and we prove monotonicity, semiconvexity and other, related to the subdifferential, properties for the corresponding value function, considered as a viscosity solution of a modified HJB equation. We extract many regularity results for the value (welfare) function, using this result. Furthermore, three different numerical schemes are presented, the "forward", the "backward" and the "upwind" schemes, for the approximation of the viscosity solution, based on a finite difference space discretization. Their convergence is proved using fixed point arguments. For validation of the numerical results, we compare them with the results obtained from the Simple Shooting Method, which we use as the "gold standard". The small mean relative error for all cases (different number of saddle points, different spatial step) proves the accuracy of the numerical approximations.

The second application analyzed is connected with the geometric representation of the Abdominal Aortic Aneurysm (AAA), which is a localized dilatation of the aortic wall. A reliable estimate of AAA rupture risk demands accurate measurements of its geometric characteristics. So, our main objective in this part of our work is the extraction of the thrombus and outer wall boundaries from cross sections of a 3D CTA AAA image data set, using the level set framework and new geometrical methods to address the basic problem of no sufficient intensity contrast between thrombus and surrounding tissue. Tools like the inversion mapping and the convex hull of a closed curve are used to trace and reconstruct these boundaries, exploiting the presence of calcifications, which are detected by combining these tools with a thresholding technique. We also introduce three novel stopping criteria to address the leakage problem that Level Set Methods (LSM's) present and a method

for detecting the leakage regions. A Fast Marching Method (FMM) is initially used to resolve another problem of the LSM's, namely speed, with a proper modification for images difficult to segment. In regions with few or no calcifications, an interpolation distance technique may be used to obtain the two boundaries, if required.

Artificial images which simulate the real cases are then presented to test the versatility of the methods. Sensitivity to the parameter settings and reproducibility are also analyzed and segmentation time is presented. A manual segmentation, created by a medical expert, was performed in the slices of ten patient data sets (450 slices) to compare with our results. Mean distance, area overlap and relative volume error are three of the quantities used to evaluate outer wall segmentation error. For the validation of the thrombus results a method for approximating the mean wall thickness of the AAA is introduced, utilizing another tool, namely the division of a curve into sectors using its centroid.

The results for the outer wall and for the mean wall thickness are comparable with previous values reported in literature, in which, however, there is no segmentation of the thrombus boundary, at least using the level set framework. These results indicate that geometrically accurate 3D reconstructions of AAA anatomy can be produced through LSM based segmentation of image data obtained from currently available imaging technology. This information is quite important for finally obtaining a reliable patient specific measure of AAA rupture risk.

Keywords: viscosity solution, optimal control, Shallow Lake Problem, Hamilton-Jacobi-Bellman (HJB) equation, skiba point, image segmentation, Abdominal Aortic Aneurysm, Level Set Method, calcifications.

Περίληψη (abstract in greek)

Οι λύσεις ιξώδους είναι μία κατηγορία γενικευμένων λύσεων για μη γραμμικές διαφορικές εξισώσεις με μερικές παραγώγους. Η μεγάλη αξία αυτού του είδους των ασθενών λύσεων φαίνεται από το ότι για αυτές υπάρχουν πολύ γενικά αποτελέσματα ύπαρξης, μοναδικότητας και ευστάθειας σε πολλά προβλήματα που προκύπτουν σε διαφορετικά πεδία εφαρμογών. Οι λύσεις ιξώδους χρησιμοποιούνται σε πολλά είδη εφαρμογών, δύο από τα οποία αναλύονται σε αυτήν τη διατριβή.

Το Πρόβλημα της Ρηχής Λίμνης (the Shallow Lake Problem), ένα πρόβλημα βέλτιστου ελέγχου που δεν ανήκει στα κλασικά και προκύπτει από τον συνδυασμό των χρήσεων μίας ρηχής λίμνης για αγροτικές δραστηριότητες αλλά και για οικολογικούς λόγους, είναι η πρώτη από τις εφαρμογές που μελετάμε. Αρχικά μελετούνται τα βέλτιστα δυναμικά του προβλήματος, για τα οποία η Αρχή Μεγίστου του Pontryagin παρέχει κάποιες αναγκαίες συνθήκες, για ένα διάστημα τιμών του παράγοντα έκπτωσης. Επίσης ερευνάται ο αριθμός και το είδος των σημείων ισορροπίας. Στη συνέχεια αποδεικνύουμε ότι η συνάρτηση αξίας του Προβλήματος της Ρηχής Λίμνης είναι λύση ιξώδους μίας Βέλτιστης Hamilton-Jacobi-Bellman (OHJB) εξίσωσης, ένα βασικό αποτέλεσμα για την υπόλοιπη εργασία. Για να προκύψει αυτό, μελετάμε το πρόβλημα ελέγχου σε ένα συμπαγές χώρο ελέγχων και αποδεικνύουμε ιδιότητες της αντίστοιχης συνάρτησης αξίας ως λύση ιξώδους μιας παραλλαγμένης HJB εξίσωσης, οι οποίες σχετίζονται με μονοτονία, ημικυρτότητα, καθώς και με το υποδιαφορικό αυτής. Στη συνέχεια εξάγουμε αρκετά αποτελέσματα ομαλότητας για την αρχική συνάρτηση αξίας (ευημερίας), με χρήση αυτού του αποτελέσματος. Επίσης παρουσιάζουμε τρία διαφορετικά αριθμητικά σχήματα, το ≪προς τα εμπρός≫, το ≪προς τα πίσω≫ και το ≪προσήνεμο≫, για την προσέγγιση της λύσης ιξώδους, στα οποία γίνεται χρήση πεπερασμένων διαφορών για την προσέγγιση των χωρικών παραγώγων. Η σύγκλισή τους αποδεικνύεται με χρήση προτάσεων σταθερών σημείων. Για την πιστοποίηση των αριθμητικών αποτελεσμάτων, τα συγκρίνουμε με τα αποτελέσματα που προκύπτουν από τη λεγόμενη Μέθοδο Απλής Στόχευσης (Simple Shooting Method), την οποία χρησιμοποιούμε ως το ≪χρυσό δεδομένο≫. Το μικρό μέσο σχετικό σφάλμα για όλες τις περιπτώσεις (διαφορετικός αριθμός σαγματικών σημείων, διαφορετικό χωρικό βήμα) αποδεικνύει την ακρίβεια των αριθμητικών προσεγγίσεων.

Η δεύτερη εφαρμογή που αναλύουμε σχετίζεται με την γεωμετρική αναπαράσταση του Ανευρύσματος Κοιλιακής Αορτής (ΑΚΑ), μιας τοπικής διαστολής του τοιχώματος της αορτής. Μια αξιόπιστη εκτίμηση του κινδύνου ρήξης ενός ΑΚΑ απαιτεί ακριβείς μετρήσεις των γεωμετρικών χαρακτηριστικών του. Επομένως, ο βασικός στόχος της μελέτης αυτής της εφαρμογής είναι η εξαγωγή των συνόρων θρόμβου και εξωτερικού τοιχώματος από εγκάρσιες τομές ενός τρισδιάστατου πακέτου εικόνων-δεδομένων του ΑΚΑ (αξονικές τομογραφίες -αγγειογραφίες,

καλούμενες CTA στη διεθνή βιβλιογραφία), με χρήση Μεθόδων Συνόλου Στάθμης (ΜΣΣ, καλούμενες Level Set Methods στη διεθνή βιβλιογραφία) και νέων γεωμετρικών μεθόδων για την αντιμετώπιση του βασικού προβλήματος της μη ύπαρξης κατάλληλης αντίθεσης στη φωτεινότητα μεταξύ του θρόμβου και του περιβάλλοντα ιστού. Εργαλεία όπως η απεικόνιση αντιστροφής και η κυρτή θήκη μίας κλειστής καμπύλης χρησιμοποιούνται για τον εντοπισμό και την ανακατασκευή αυτών των συνόρων, εκμεταλλευόμενοι την ύπαρξη ασβεστώσεων, οι οποίες εντοπίζονται συνδυάζοντας αυτά τα εργαλεία με μία τεχνική οριοθέτησης της έντασης της εικόνας (thresholding). Επίσης, παρουσιάζουμε τρία νέα κριτήρια διακοπής για την αντιμετώπιση των προβλημάτων διαρροής που παρουσιάζουν οι ΜΣΣ και μία μέθοδο για τον εντοπισμό των περιοχών διαρροής. Η Μέθοδος Ταχείας Ανάπτυξης (ΜΤΑ, καλούμενη Fast Marching Method στη διεθνή βιβλιογραφία) χρησιμοποιείται αρχικά για την επίλυση ενός άλλου προβλήματος της ΜΣΣ, της σχετικά μικρής ταχύτητας, με κατάλληλες τροποποιήσεις για την περίπτωση δύσκολων στην κατάτμηση εικόνων. Σε περιοχές με λίγες ή καθόλου ασβεστώσεις προτείνουμε μία τεχνική παρεμβολής αποστάσεων που μπορεί να χρησιμοποιηθεί για να πάρουμε τα δύο σύνορα, αν κρίνεται απαραίτητο.

Στη συνέχεια κατασκευάσαμε και παρουσιάζουμε κάποιες τεχνητές εικόνες που εξομοιώνουν τις πραγματικές περιπτώσεις με σκοπό την εξέταση της ευελιξίας των μεθόδων. Επίσης αναλύεται η ευαισθησία των μεθόδων στις αλλαγές των τιμών των παραμέτρων, καθώς και η αναπαραγωγιμότητά τους, ενώ παρουσιάζεται και ο χρόνος κατάτμησης. Έχοντας ως στόχο την σύγκριση με τα αποτελέσματά μας, ειδικός αγγειοχειρούργος πραγματοποίησε χειροκίνητες κατατμήσεις στις τομές πακέτων δεδομένων δέκα ασθενών (450 τομές). Για την εκτίμηση του σφάλματος στην κατάτμηση του εξωτερικού τοιχώματος χρησιμοποιήσαμε διάφορες ποσότητες, τρεις από τις οποίες είναι η μέση απόσταση, η περιοχή επικάλυψης και το σχετικό σφάλμα του όγκου. Για την πιστοποίηση των αποτελεσμάτων για τον θρόμβο, δημιουργήθηκε μία μέθοδος που προσεγγίζει το μέσο πάχος του τοιχώματος ενός ΑΚΑ, στην οποία γίνεται χρήση ενός άλλου εργαλείου, της διαίρεσης μίας καμπύλης σε τομείς με χρήση του κέντρου βάρους της.

Τα αποτελέσματά μας για το εξωτερικό τοίχωμα και για το μέσο πάχος τοιχώματος είναι συγκρίσιμα με προηγούμενες τιμές που έχουν αναφερθεί στη σχετική βιβλιογραφία, στην οποία, όμως, δεν έχει παρατηρηθεί πουθενά κατάτμηση του συνόρου του θρόμβου, τουλάχιστον όχι με χρήση των ΜΣΣ. Τα αποτελέσματα αυτά δείχνουν ότι γεωμετρικά ακριβείς τρισδιάστατες αναδομήσεις της ανατομίας ενός ΑΚΑ μπορούν να παραχθούν μέσω μεθόδων κατάτμησης βασισμένων στις ΜΣΣ, πάνω σε ιατρικές εικόνες που προέρχονται από την διαθέσιμη τεχνολογία παραγωγής τους. Αυτή η πληροφορία της γεωμετρίας είναι πολύ σημαντική για την τελική επίτευξη ενός αξιόπιστου, προσαρμοσμένου στον ασθενή, μέτρου του κινδύνου ρήξης ενός ΑΚΑ.

Λέξεις -κλειδιά: λύση ιξώδους, βέλτιστος έλεγχος, Πρόβλημα Ρηχής Λίμνης, εξίσωση Hamilton-Jacobi-Bellman (HJB), σημείο Skiba, κατάτμηση εικόνας, Ανεύρυσμα Κοιλιακής Αορτής, Μέθοδος Συνόλου Στάθμης, ασβεστώσεις.

Contents

Chapter 1

Introduction

1.1 The Viscosity Solution

When M. G. Crandall and P. L. Lions (Fields Medalist in 1994) introduced the notion of "viscosity solutions" in [14] (and then, also, in [12], [13]) they probably had not realized the future value of this concept (which is also closely related to some previous work by L. C. Evans [22]) and the kinds of applications in which it would be used. Viscosity solutions are a class of generalized (weak) solutions of nonlinear scalar partial differential equations of the form

$$F(y, u(y), Du(y)) = 0 \quad \text{for } y \in O, \tag{1.1.1}$$

where O is an open set in $\mathbb{R}^n$, $F : O \times \mathbb{R} \times \mathbb{R}^n \to \mathbb{R}$ is continuous and $Du = \left(\frac{\partial u}{\partial y_1}, \ldots, \frac{\partial u}{\partial y_n}\right)$ denotes the gradient of u. The only regularity required in their definition, as we will see, is continuity. They need not be differentiable anywhere and thus are not sensitive to the classical problem of the crossing of characteristics. The authors in [14] utilized this new concept to establish uniqueness, stability and certain existence theorems for a wide class of equations of the form of (1.1.1). Prior to the notion of viscosity solution, there were few more notions of weak solutions, such as Clarke's generalized solution and Subbotin's minimax solution, but these notions are specific to the first order equations, with special dependence on gradient variable. The value of this concept is exactly the fact that very general existence (see [37]), uniqueness and continuous dependence results hold for viscosity solutions of many problems arising in fields of application.

The notion of a "viscosity solution" admits several equivalent formulations. Two of these equivalent criteria (definitions) are most commonly used. For the first one, the notion of super- and subdifferential are introduced in [12] (they were also previously employed in another context in [19]):

Definition 1.1.1. Let u be a function from O into $\mathbb{R}$ and let $x \in O$. Then the superdifferential of u at x is the set, denoted by $D^+u(x)$, of $p \in \mathbb{R}^n$ such that

$$\limsup_{y \to x} \frac{u(y) - u(x) - p \cdot (y - x)}{|y - x|} \leq 0 \tag{1.1.2}$$

holds. Similarly, the subdifferential of u at x is the set, denoted by $D^-u(x)$, of $q \in \mathbb{R}^n$ such that

$$\liminf_{y \to x} \frac{u(y) - u(x) - q \cdot (y - x)}{|y - x|} \geq 0 \tag{1.1.3}$$

holds.

We may now define the concept of the viscosity solution of (1.1.1):

Definition 1.1.2. A viscosity solution of (1.1.1) is a function $u \in C(O)$ satisfying

$$F(y, u(y), p) \leq 0 \quad \forall y \in O,\ \forall p \in D^+u(y), \tag{1.1.4}$$

and

$$F(y, u(y), q) \geq 0 \quad \forall y \in O,\ \forall q \in D^-u(y). \tag{1.1.5}$$

Any u satisfying (1.1.4) will be called a viscosity subsolution of (1.1.1), whereas, if (1.1.4) holds, then u is a viscosity supersolution of (1.1.1).

This definition is equivalent to the following notion of solution of (1.1.1), expressed in terms of test functions:

Definition 1.1.3. $u \in C(O)$ is a viscosity solution of (1.1.1) provided for all $\phi \in C^1(O)$,

if $u - \phi$ attains a local maximum at $x \in O$, then

$$F(x, u(x), D\phi(x)) \leq 0, \tag{1.1.6}$$

which is equivalent to (1.1.4), and

if $u - \phi$ attains a local minimum at $x \in O$, then

$$F(x, u(x), D\phi(x)) \geq 0, \tag{1.1.7}$$

which is equivalent to (1.1.5)

The equivalence of the two definitions is an immediate consequence of the following

Proposition 1.1.1. *Let $u \in C(O)$, $x \in O$, $p \in \mathbb{R}^n$. Then the following are equivalent:*
(i) $p \in D^+u(x)$ (resp. $q \in D^-u(x)$) and
(ii) there exists $\phi \in C^1(O)$ such that $u - \phi$ has a local maximum (resp. minimum) at x and $D\phi(x) = p$ (resp. $D\phi(x) = q$).

For the proof of this, see [12]. A selection of some of the most important properties of viscosity solutions is made in the next Proposition:

Proposition 1.1.2. *1. (i) Let $u \in C^1(O)$ be a classical solution of (1.1.1), that is*

$$F(y, u(y), Du(y)) = 0 \quad \text{in } O,\ u \in C^1(O).$$

Then u is a viscosity solution.

(ii) Let u be a viscosity solution of (1.1.1) which is differentiable at some $x \in O$. Then

$$F(x, u(x), Du(x)) = 0.$$

2. *(i) Let u, v be viscosity subsolutions (resp. supersolutions) of (1.1.1). Then $w = \max(u, v)$ (resp. $w = \min(u, v)$) is a viscosity subsolution (resp. supersolution) of (1.1.1).*

   (ii) Let $(u_n)_{n\geq 1}$ be viscosity subsolutions (resp. supersolutions) of (1.1.1). If $w = \sup_{n\geq 1} u_n$ (resp. $\inf_{n\geq 1} u_n$)$\in C(O)$, then w is a viscosity subsolution (resp. supersolution) of (1.1.1).

3. *Let $F_n(y, t, p)$ be a sequence of continuous functions such that $F_n(y, t, p)$ converges uniformly on compact subsets of $O \times \mathbb{R} \times \mathbb{R}^n$ to some function $F(y, t, p)$. Let u_n be a viscosity solution of $F_n(y, u_n, Du_n) = 0$ in O. We assume that u_n converges uniformly on compact subsets of O to some u. Then u is a viscosity solution of $F(y, u, Du) = 0$.*

4. ***Uniqueness for $\mathbf{u + H(Du) = f}$ in $\mathbb{R}^n$:*** *Let $u, v, f, g, H \in C(\mathbb{R}^n)$. Assume that u,v are bounded and f,g are uniformly continuous on $\mathbb{R}^n$. Assume that u and v are viscosity solutions of, respectively, $u + H(Du) = f$, $v + H(Dv) = g$ in $\mathbb{R}^n$. Then we have*

$$\sup_{\mathbb{R}^n}(u - v)^+ \leq \sup_{\mathbb{R}^n}(f - g)^+. \tag{1.1.8}$$

For the proof of these properties, see [12]. The name of the viscosity solutions (and their existence) is explained in the following theorem (which is proved in Proposition IV.1 of [14] and Theorem 3.1 of [12]):

Theorem 1.1.1. *Let $\varepsilon > 0$ and let $F_\varepsilon(y, t, p)$ be a family of continuous functions such that $F_\varepsilon(y, t, p)$ converges uniformly on compact subsets of $O \times \mathbb{R} \times \mathbb{R}^n$ to some function $F(y, t, p)$, as ε goes to 0. Finally, suppose $u^\varepsilon \in C^2(O)$ is a solution of*

$$-\varepsilon \Delta u^\varepsilon + F_\varepsilon(y, u^\varepsilon, Du^\varepsilon) = 0 \quad in \quad O, \tag{1.1.9}$$

and let us assume that the u^ε converge uniformly on compact subsets of O to some $u \in C(O)$. Then u is a viscosity solution of (1.1.1).

An amazing range of applications of PDE's has been found where viscosity solutions play an essential role. These include first order equations arising in optimal control (the Hamilton-Jacobi-Bellman equation), image processing, differential games (the Isaacs equation), geometrical optics or front evolution problems (see [10], [2], [5], [24]).

1.2 Optimal Control and Viscosity Solutions

In this thesis we will see two applications of the viscosity solutions. The first one, analyzed in the second Chapter, is called "The Shallow Lake Problem" and it is an optimal

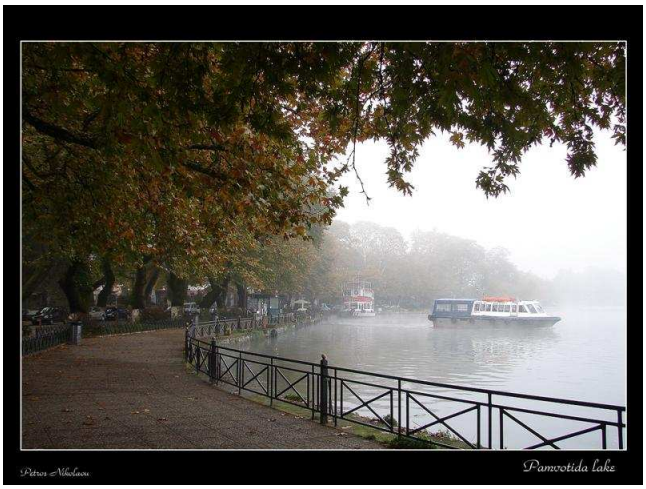

Figure 1.1: The Lake of Ioannina (also Pamvotida): The most famous Shallow Lake of Greece.

control problem concerning the optimization of the use of a shallow lake (Fig. 1.1) taking into consideration its two utilities (see Sec. 2.1). We will now mention the way an optimal control problem is formulated (see [5]):

We consider a control system, governed by the state equation

$$\begin{cases} y'(t) = f(y(t), \alpha(t)), \quad t > 0, \\ y(0) = x. \end{cases} \tag{1.2.1}$$

The control α is any measurable function of $t \in [0, +\infty)$ with values in B, which generally is a topological space and is called the control space. We assume that the dynamics $f : \mathbb{R}^N \times B \to \mathbb{R}^N$ is such that the state equation (1.2.1) has a unique solution defined for all $t \in [0, +\infty)$, for any choice of the control α and of the initial position $x \in \mathbb{R}^N$, denoted by $y_x(t, \alpha)$. A running cost is also included in the model, associated with this controlled evolution, described by a given function $l : \mathbb{R}^N \times B \to \mathbb{R}$. The cost functional to be minimized is

$$J(x, \alpha) = \int_0^{+\infty} l(y_x(t, \alpha), \alpha(t)) e^{-\lambda t} dt, \tag{1.2.2}$$

where $\lambda > 0$ represents a (fixed) discount factor. The welfare (value) function of this optimal control problem is defined by

$$w(x) := \inf_{\alpha \in A} J(x, \alpha), \tag{1.2.3}$$

where A denotes the set of all measurable functions $\alpha : [0, +\infty) \to B$. The characterization of w is the basic question posed and the fundamental idea of dynamic programming is that w satisfies a functional equation, called the Dynamic Programming Principle (DPP, see

[5]) and when w is smooth enough, its infinitesimal version, the Hamilton-Jacobi-Bellman (HJB) equation. This is a first order nonlinear partial differential equation, namely

$$\lambda w(x) + \sup_{a \in B} \{-f(x,a) \cdot Dw(x) - l(x,a)\} = 0, \tag{HJB}$$

where $Dw(x)$ denotes the gradient of w at the point x. The way (HJB) is derived (using the DPP) is a classical result which can be found in many books (see e.g. Chapter III of [5]). Due to the fact that everywhere differentiability is a too restrictive assumption on w, the notion of viscosity solution is used. So we have

Proposition 1.2.1. *If the value function w, defined in (1.2.3), of the optimal control problem defined above is continuous, then it is a viscosity solution of equation (HJB).*

For the proof of this, see [5]. So, in the second Chapter, we prove that the value function of the Shallow Lake Problem can be considered as a viscosity solution of an optimal HJB equation. This result will provide many other results concerning its regularity. In addition, it will help us derive monotone numerical schemes approximating this viscosity solution, based on a finite difference space discretization. Finally, we validate these numerical results by comparing them with another method called the Simple Shooting Method.

1.3 Curve Evolution: The Eulerian Approach

The second application of the viscosity solutions that we will see, presented in the third Chapter of this work, is the 2D image segmentation of the thrombus and outer wall boundaries of an Abdominal Aortic Aneurysm (Fig. 1.2) from cross sections of a 3D CTA image data set, using Level Set Methods. These methods are extracted by the need to formulate the curve and surface evolution problem in an Eulerian framework, that is, one in which the underlying coordinate system remains fixed. The geometric (Lagrangian) approach of interface propagation, linking moving fronts and hyperbolic conservation laws (see the second and third Chapter of [51]) cannot be formally extended to higher dimensions. In addition, it is much more difficult to obtain vanishing viscosity solutions with Lagrangian methods that faithfully follow the characteristics.

In contrast, we work directly with the partial differential equation and add a viscous right-hand side. The solution to this equation is smooth for all time and the limit as the viscosity term goes to zero produces the appropriate weak solution (the viscosity solution, see Theorem 1.1.9). This solution, which allows corners while the curve is evolving, is shown to be equivalent to the classical (smooth) solution, where the solution is smooth. Then, under certain restrictions, it is shown that the viscosity solution is equal to the limit as the viscous term vanishes and this is exactly the theory of viscosity solutions as mentioned earlier. To sum up, the transformation of geometry problems into a partial differential equation setting means that some powerful analytic techniques, including viscosity solutions, could be applied. For more about the connection between curve evolution and viscosity solutions, including many other references on this subject, see [51] and [46].

In the third Chapter of this work, we address the problem of no sufficient contrast between thrombus and surrounding tissue which makes the task of segmentation quite

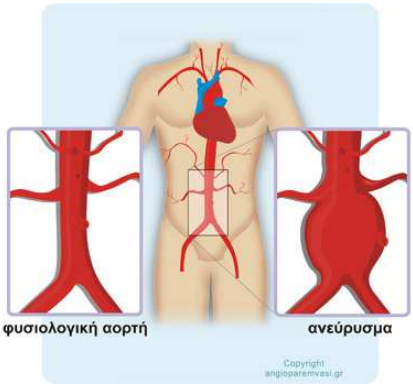

Figure 1.2: Abdominal Aortic Aneurysm: A permanent irreversible localized dilatation of the abdominal section of the aorta (right image).

difficult, by using Level Set and geometrical methods. The main objective, which is not found in the related literature, is to accurately distinguish the thrombus and outer wall boundaries from the cross sections, using the level set framework. The results are then compared with a manual segmentation of the slices of ten patient data sets to quantify the segmentation quality. Finally, the fourth Chapter includes the general conclusions extracted from the analysis of the two applications of the viscosity solutions presented in the previous two Chapters.

Chapter 2

The Shallow Lake Problem

The economic analysis of a shallow lake ecological system requires the study of a non-standard optimal control problem due to the conflicting services it provides. The physical and the control problem are described in the first section of this Chapter. In Sec. 2.2 we study the optimal dynamics of the problem given by Pontryagin Maximum Principle for all values of the discount factor ρ in $(0, 0.4]$ and investigate the number and the form of the equilibrium points. In Sec. 2.3 we show that we can consider the value function of the Shallow Lake Problem as a viscosity solution of an optimal HJB equation. We also study the regularity of the value function. In Sec. 2.4 we derive monotone numerical schemes approximating the viscosity solution, based on a finite difference space discretization. The convergence of these schemes is also proved in this section. In Sec. 2.5 we compare the numerical results produced by these schemes with the results obtained by the Simple Shooting Method.

2.1 Introduction-Description Of The Problem

Shallow lakes form one of the most fragile ecosystem types on earth and they are generally the first to perish under development activities. Millions of people live near the shores of shallow lakes and their lives depend on conditions of those lakes. Furthermore, shallow lakes are generally situated on farmable lowlands, which makes them more vulnerable to human disturbances. So, it is easily understood why there is a special research on shallow lakes, which, nevertheless, has been intensified only recently (for more about this research, see [25]).

Pollution of shallow lakes is a phenomenon which is quite often observed, due to a heavy use of fertilizers on surrounding land and an increased inflow of waste water from human settlements and industries. Phosphorus is the most usual limiting nutrient. The flow of phosphorus into a lake effects the growth of algae. The result is that sun light is not able to penetrate the water. So, a clear, blue lake with green plants changes to a lake with very little visibility, with hardly any green plants and with a general reduction in fish stocks (see [42]).

The problem of optimal control that is studied here comes from the combination of two factors, the utility of the agricultural activities and the utility of a clear lake with many

ecological services (for recent papers which have explored some fundamental issues of the optimal level of pollution in a lake with competing uses, see [18]). The economic issue that lakes are usually common property resources and therefore suffer from sub-optimal use by many communities, is also considered. The dynamic system of the problem is

$$\begin{cases} y'(t) = \alpha(t) - b \cdot y(t) + \frac{y^2(t)}{y^2(t)+1}, & t > 0, \\ y(0) = x_0, \end{cases} \tag{2.1.1}$$

where $\alpha(t) = \sum_{i=1}^{n} \alpha_i(t)$ and α_i is the loading of phosphorus that every community loads in the lake, $y(t)$ is the amount of phosphorus in algae and b is the rate of loss, consisting of sedimentation, outflow and sequestration in other biomass. The function $k(y) = \frac{y^2}{y^2+1}$ is a positive feedback term, which has to do with the role of the green plants in controlling the bottom of the lake: As the amount of green plants is reduced, the bottom sediments become more vulnerable to winds, waves and bottom eating fishes. As a result, sedimented phosphorus will be released into the water and contribute to further grow of algae. So, this function has to be non-decreasing in y. In addition, it has to be convex for small y and concave for large y because when the stock of algae reaches a certain size, blue green algae or cyano-bacteria will take over and eventually dominate the stock of algae. So, ecologists usually approximate this feedback with the sigmoid function $\frac{y^2}{y^2+1}$ (see [42]).

We assume that $\alpha_i(t) > 0,\ t \in [0, +\infty)$, and we have that the running cost for the $i-$th community is $\ln(\alpha_i) - cy^2$. The lake has value as a waste sink for agriculture ($\ln(\alpha_i)$) and it provides ecological services that decrease with the amount of phosphorus ($-cy^2$). The parameter c reflects the relative weight of these welfare components (large c means great weight to the ecological services of the lake). We suppose that the problem has an infinite horizon, so that the objectives become

$$W_i = \int_0^{\infty} e^{-\rho t} \left[\ln(\alpha_i(t)) - c y_{x_0}^2(t, \alpha)\right] dt, \quad i = 1, \ldots, n \tag{2.1.2}$$

where $\rho > 0$ is the discount factor. Optimal management of the lake (which is the approach adopted in this work) requires to maximize the sum of the objectives W_i, subject to the above dynamic system (for the literature on the different approaches used to analyze the Shallow Lake Problem, see [28]). This is an optimal control problem and its welfare function, which represents this maximization of the intertemporal welfare subject to these dynamics of the lake, is

$$W(x_0) = \sup_{(\alpha_1,\ldots,\alpha_n)\in A} \int_0^{\infty} e^{-\rho t} \left[\sum_{i=1}^{n} ln(\alpha_i(t)) - n c y_{x_0}^2(t, \alpha)\right] dt. \tag{2.1.3}$$

The Hamiltonian, in this case, is

$$H(x, \lambda) = \sup_{(a_1,\ldots,a_n)\in B} \left\{ \left(a - bx + \frac{x^2}{x^2+1}\right)\lambda + \sum_{i=1}^{n} ln(a_i) - ncx^2 \right\}, \tag{2.1.4}$$

where $a = \sum_{i=1}^{n} a_i$, A is the set of all measurable functions $(\alpha_1, \ldots, \alpha_n) : [0, +\infty) \to B$ and $B \subseteq \mathbb{R}^n$. Supposing that W is smooth enough, it satisfies the (HJB) equation

$$\rho W(x) = H(x, DW). \tag{HJB}$$

This is a result of the Dynamic Programming Principle, as it is already mentioned in Sec. 1.2. In general, W is not expected to be differentiable. This is the case for various values of the discount factor, where a vortex in the optimal control-space phase diagram appears. A Skiba point is present and the optimal path jumps from an upper trajectory to a lower one, or the opposite (see [43], [54]). As a result, the welfare function is expected to undergo a change of slope and this makes W non-smooth at the Skiba point. Thus, equation (HJB) should be considered in a generalized sense. Since the welfare (value) function (2.1.3) is expected to be continuous and bounded, viscosity solutions provide the right framework to study (HJB).

In this Chapter, which is a great part of [33], we first study our control problem on a compact control space and we prove monotonicity properties for the corresponding value function as a viscosity solution of a modified Hamilton-Jacobi equation. These properties are inherited in the limit to the value function (2.1.3). We exploit these properties to show that (HJB) reduces to the following Hamilton-Jacobi equation

$$\rho W(x) - \left(\frac{x^2}{x^2+1} - bx\right) DW + 2\left(\ln(-DW) + x^2 + 1\right) = 0. \tag{OHJB}$$

We further study the regularity of (2.1.3) as the viscosity solution of (OHJB) and relate it with the dynamics of the optimal control problem. We finally approximate (2.1.3) by means of monotone convergent schemes and present various numerical results.

2.2 Control Problem Analysis For Different Discount Factor Values

We consider $n = 2$ and $c = 1$. The Pontryagin Maximum Principle is the most classical and useful necessary condition of optimality, in optimal control theory (see [50]). In our case, this Maximum Principle states that, if $c(t) = (\alpha_1(t), \alpha_2(t))$ is an optimal control for the initial state $x_0 \in \mathbb{R}$ and $x(t) := y_{x_0}(t, \alpha)$ is the associated optimal path, where $\alpha(t) = \alpha_1(t) + \alpha_2(t)$, then there exists a continuous and piecewise continuously differentiable function $\tilde{\lambda}(t)$, called adjoint function or adjoint variable, such that, if

$$\bar{H}(x, c, \tilde{\lambda}, t) = \left(\alpha - bx + \frac{x^2}{x^2+1}\right)\tilde{\lambda} + [\ln(\alpha_1) + \ln(\alpha_2) - 2x^2]e^{-\rho t}$$

then

$$\max_{(u_1,u_2)\in B} \bar{H}(x(t), (u_1, u_2), \tilde{\lambda}(t), t) = \bar{H}(x(t), c(t), \tilde{\lambda}(t), t) \tag{2.2.1}$$

and

$$\tilde{\lambda}'(t) = -\bar{H}_x(x(t), c(t), \tilde{\lambda}(t), t). \tag{2.2.2}$$

From (2.2.1) we deduce that

$$\begin{aligned}
&\frac{\partial \bar{H}}{\partial u_1}(x(t), c(t), \tilde{\lambda}(t), t) = \frac{\partial \bar{H}}{\partial u_2}(x(t), c(t), \tilde{\lambda}(t), t) = 0 \\
\Rightarrow \quad & \tilde{\lambda}(t) + \frac{1}{\alpha_i(t)} e^{-\rho t} = 0, \quad i = 1, 2 \\
\Rightarrow \quad & \tilde{\lambda}(t) e^{\rho t} + \frac{1}{\alpha_i(t)} = 0, \quad i = 1, 2 \\
\Rightarrow \quad & \lambda(t) + \frac{1}{\alpha_i(t)} = 0, \quad i = 1, 2
\end{aligned} \tag{2.2.3}$$

where $\lambda(t) := \tilde{\lambda}(t) e^{\rho t}$. From (2.2.2) we have :

$$\begin{aligned}
&\tilde{\lambda}'(t) = \left(b - \frac{2x(t)}{(x^2(t)+1)^2} \right) \tilde{\lambda}(t) + 4x(t) e^{-\rho t} \\
\Rightarrow \quad & \tilde{\lambda}'(t) e^{\rho t} = \left(b - \frac{2x(t)}{(x^2(t)+1)^2} \right) \tilde{\lambda}(t) e^{\rho t} + 4x(t) \\
\Rightarrow \quad & \lambda'(t) - \tilde{\lambda}(t) e^{\rho t} \rho = \left(b - \frac{2x(t)}{(x^2(t)+1)^2} \right) \tilde{\lambda}(t) e^{\rho t} + 4x(t) \\
\Rightarrow \quad & \lambda'(t) - \lambda(t) \rho = \left(b - \frac{2x(t)}{(x^2(t)+1)^2} \right) \lambda(t) + 4x(t) \\
\Rightarrow \quad & \lambda'(t) = \left((b+\rho) - \frac{2x(t)}{(x^2(t)+1)^2} \right) \lambda(t) + 4x(t).
\end{aligned} \tag{2.2.4}$$

By relation (2.2.3) we deduce that

$$\alpha_1(t) = \alpha_2(t) = -\frac{1}{\lambda(t)} = \frac{\alpha(t)}{2} \tag{2.2.5}$$

Equation (2.2.4) using (2.2.5) is written

$$\begin{aligned}
& 2\frac{\alpha'(t)}{\alpha^2(t)} = \left((b+\rho) - \frac{2x(t)}{(x^2(t)+1)^2} \right) \left(-\frac{2}{\alpha(t)} \right) + 4x(t) \\
\Rightarrow \quad & \alpha'(t) = -\left((b+\rho) - \frac{2x(t)}{(x^2(t)+1)^2} \right) \cdot \alpha(t) + 2x(t)\alpha^2(t).
\end{aligned} \tag{2.2.6}$$

From equations (2.1.1) and (2.2.6) we take the following O.D.E. autonomous system

$$\begin{cases}
x'(t) = \alpha(t) - b \cdot x(t) + \frac{x^2(t)}{x^2(t)+1}, \\
\alpha'(t) = -\left((b+\rho) - \frac{2x(t)}{(x^2(t)+1)^2} \right) \alpha(t) + 2x(t)\alpha^2(t).
\end{cases} \tag{2.2.7}$$

In the following, we will refer to the first and the second right-hand sides of (2.2.7) as $f_1(x, \alpha)$ and $f_2(x, \alpha)$, respectively. The dynamics of the optimal control problem are described through the stable manifolds described in (2.2.7) as we will show later, at the end of this section. This problem can be studied for arbitrary values of ρ and b. If α is

constant the first equation of (2.2.7) has one stable equilibrium for high values of α. For low values of α, three situations can occur depending on the value of the parameter b: this equation can have one stable equilibrium or two equilibria (in this case the third root of the right-hand side of the equation determines the domains of attraction) or low values of α can yield one stable equilibrium again, followed by a range of α's with two equilibria. In the following, the problem is studied for $\rho \in (0, 0.4]$ and $b = 0.6$. The discount factor usually takes small positive values, so this domain is appropriate for ρ. In addition, for this value of b we are in the third situation mentioned above. We choose this value so that the lake displays hysteresis but a flip from the oligotrophic state to a eutrophic state is reversible (the lake can flip back to an oligotrophic state if α is reduced further than the flip point, see [43]). Let us note that, if we considered an arbitrary value for b, all the results that are produced below would be similar. We will also consider that $x \in [0, 2]$ at the rest of this Chapter.

We now have the following lemmas (see the Appendix A for their proof):

Lemma 2.2.1. *For $\rho \in (0, 0.4]$ and $b = 0.6$ the autonomous system (2.2.7) has only one or three equilibrium points for $x \in [0, 2]$.*

Lemma 2.2.2. *In case we have only one equilibrium point for system (2.2.7), under the conditions described in Lemma 2.2.1, this is a saddle point. In case we have three equilibrium points, the first and third are saddle-point stable and the point in the middle is a vortex, that is, unstable with complex eigenvalues for the stability matrix of the system (with the exception of degeneracies, which appear when ρ is near the boundary of the range in which we have three equilibrium points).*

In Fig. 2.1 we can see the equilibrium points (the intersection points of the curves $f_1(x, \alpha) = 0$ and $f_2(x, \alpha) = 0$) for different values of ρ. For a graphical approximation of the range of ρ in which each of the two cases described in Lemma 2.2.1 occur, see the Appendix A.2.

As it is already mentioned, the classic way of solving the problem and finding the welfare function is through the stable manifolds, the graphs of which can be made by using the Simple Shooting Method (see Sec. 2.5). In the case of one saddle point (x_{s0}, α_{s0}), there are two stable (and two unstable) manifolds. This case is presented in Fig. 2.2, where the curves representing the steady-states for x ($f_1(x, \alpha) = 0$) and the steady-states for α ($f_2(x, \alpha) = 0$) are also shown.

Using the definition of the saddle point, we have

$$\begin{aligned} W(x_{s0}) &= \max_{(\alpha_1,\alpha_2)\in A} \int_0^\infty e^{-\rho t} \left[\ln(\alpha_1(t)) + \ln(\alpha_2(t)) - 2y^2_{x_{s0}}(t,\alpha)\right] dt \\ &= \int_0^\infty e^{-\rho t} \left[2\ln\left(\frac{\alpha_{s0}}{2}\right) - 2{x_{s0}}^2\right] dt \\ &= \left(2\ln\left(\frac{\alpha_{s0}}{2}\right) - 2{x_{s0}}^2\right) \int_0^\infty e^{-\rho t} dt \end{aligned}$$

$$\Rightarrow W(x_{s0}) = \left(2\ln\left(\frac{\alpha_{s0}}{2}\right) - 2{x_{s0}}^2\right) \cdot \frac{1}{\rho} \tag{2.2.8}$$

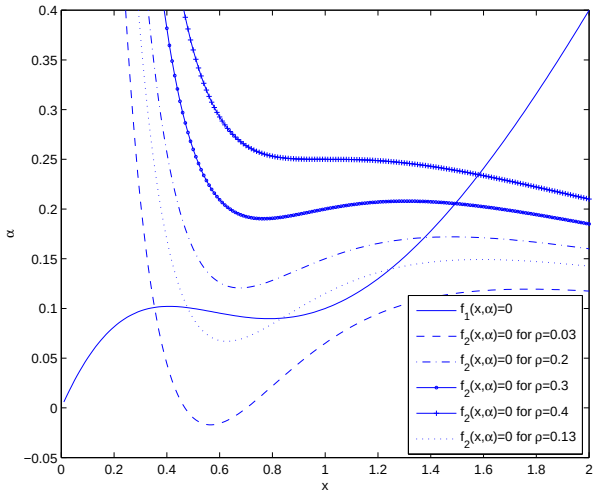

Figure 2.1: The $x-\alpha$ diagram for different values of ρ (b=0.6). The two cases of one and of three equilibrium points (which are the intersection points of the curves $f_1(x,\alpha)=0$ and $f_2(x,\alpha)=0$) are depicted.

So, the welfare function at a point x can be found via the stable manifolds through integration, as

$$W(x)=W(x_{s0})+\int_{x_{s0}}^{x}DW(k)dk=W(x_{s0})+\int_{x_{s0}}^{x}\lambda(k)dk\overset{(2.2.5)}{=}W(x_{s0})+\int_{x_{s0}}^{x}-\frac{2}{\alpha(k)}dk. \tag{2.2.9}$$

Figure 2.3 shows the welfare function in the one saddle point case, calculated through the stable manifolds provided by the Simple Shooting Method.

In the case of two saddle points x_{s1},x_{s2} and a vortex x_{s3}, there are four stable manifolds (see Fig. 2.4). In this case it can be proved that there is a point $x_s\in[x_1,x_2]$, where x_1 and x_2 are the x- coordinates of the intersection points of the outer upper curl and the outer lower curl with the curve representing the steady-states for x, respectively, such that

$$\Delta W(x_s)=0;\ \Delta W(x)<0, x\in[x_1,x_s);\ \Delta W(x)>0, x\in(x_s,x_2]. \tag{2.2.10}$$

Let us note that this point exists only in the case this curve ($f_1(x,\alpha)=0$) intersects both the outer upper and the outer lower curves (i.e. if $[x_1,x_2]\neq\emptyset$) and this is not always the case (see [61]). Following our notation, ΔW is the difference of the welfare functions obtained by integrating the upper trajectory leading to the steady-state on the right (W_r) and the lower trajectory leading to the steady-state on the left (W_l) by means of equation (2.2.9). The point x_s (see the Appendix of [43] for the proof of the existence of this point) is called a Skiba point and it can be approximated as the intersection point of W_r and W_l

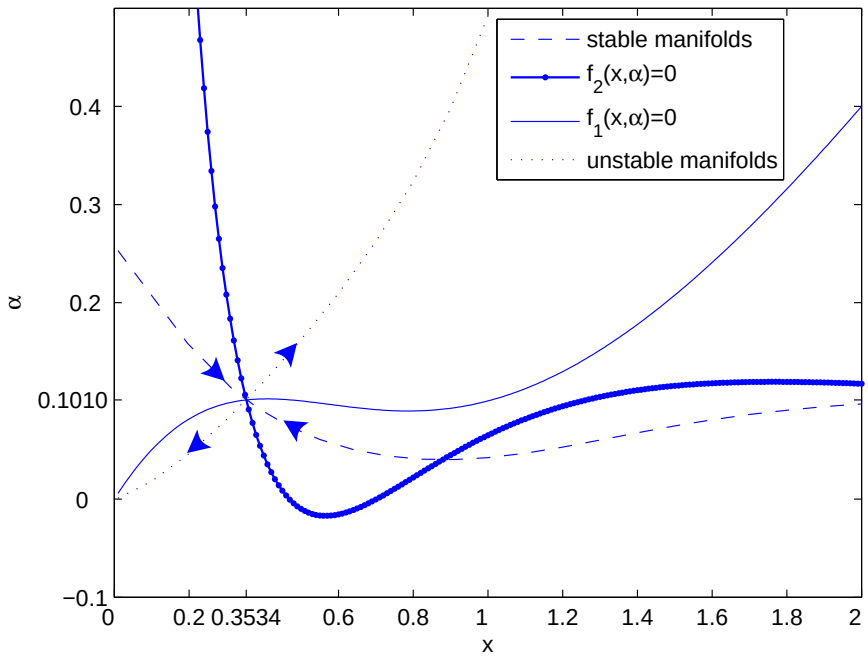

Figure 2.2: Example of an x-α diagram in the case of one saddle point. In this case, b=0.6 and ρ=0.03. The curves $f_1(x,\alpha) = 0$ and $f_2(x,\alpha) = 0$ represent the steady-states for x and the steady-states for α, respectively.

(W is multi-valued in $[x_1, x_2]$, see Fig. 2.5). Relation (2.2.10) implies that if the initial amount of phosphorus x_0 is on the left-hand side of the Skiba point, the equilibrium jumps to the lower trajectory and moves towards the steady-state on the left and if the initial amount of phosphorus x_0 is on the right-hand side of the Skiba point, the equilibrium jumps to the upper trajectory and moves towards the steady-state on the right. The optimal trajectory provided by the Simple Shooting Method and the jump of the control at x_s are depicted in Fig. 2.6.

In the work of this Chapter, we study the problem through the HJB equation using the viscosity solutions framework. This is presented in the following section.

2.3 Study Of The Value Function (Welfare Function)

2.3.1 Consideration Of The Value Function As A Viscosity Solution

In our problem, Definition 1.1.3 of the viscosity solution is written as follows:

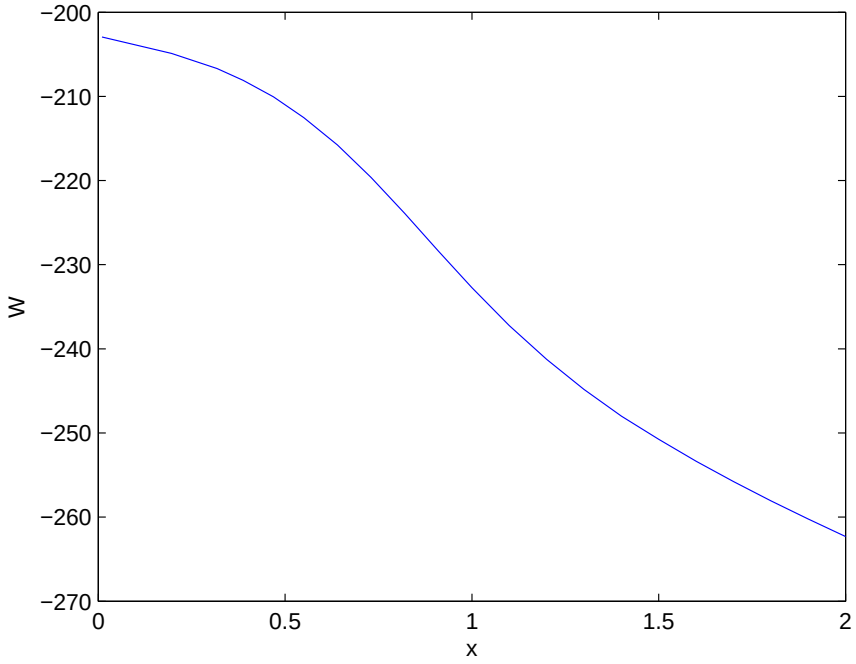

Figure 2.3: The welfare function provided by the Simple Shooting Method in the one saddle point case ($b = 0.6, \rho = 0.03$).

Definition 2.3.1. A continuous function V is a viscosity solution of our (HJB) equation in $O \subseteq \mathbb{R}$, where O is an open interval, if the following conditions are satisfied:

(i) For any $\phi \in C^1(O)$, if $y \in O$ is a local maximum point for $V - \phi$, then

$$\rho V(y) \leq H(y, D\phi(y)).$$

(ii) For any $\phi \in C^1(O)$, if $y \in O$ is a local minimum point for $V - \phi$, then

$$\rho V(y) \geq H(y, D\phi(y)).$$

Any V satisfying (i) is called a viscosity subsolution of our (HJB) equation in O, whereas, if (ii) holds, then V is a viscosity supersolution in O.

As mentioned in Sec. 1.1, there is an equivalent way to formulate conditions (i) and (ii) in terms of the superdifferential and the subdifferential of V at a point x (Definition 1.1.2). But first, let us see how Definition 1.1.1 of super- and subdifferentials is simplified in the case of a real function:

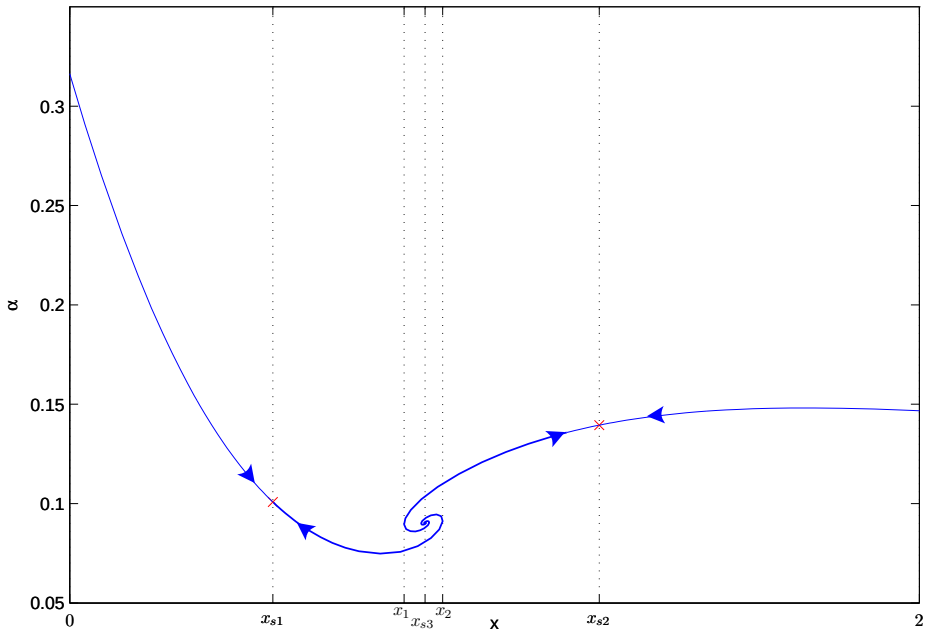

Figure 2.4: Example of an x-α diagram, where the stable manifolds are shown, in the case of three equilibrium points. x_{s1} and x_{s2} are the two saddle points, x_{s3} is the vortex and $[x_1, x_2]$ is the domain where the set of spirals appear. In this case, b=0.6 and ρ=0.13.

Definition 2.3.2. Let V be a function from (a, b) into $\mathbb{R}$ and let $x_0 \in (a, b)$. Then the superdifferential of V at x_0 is the set of $p_0 \in \mathbb{R}$, denoted by $D^+V(x_0)$, such that

$$V(x) \leq V(x_0) + p_0(x - x_0) + o\left(|x - x_0|\right) \tag{2.3.1}$$

holds. Similarly the subdifferential of V at x_0 is the set of $p_0 \in \mathbb{R}$, denoted by $D^-V(x_0)$, such that

$$V(x) \geq V(x_0) + p_0(x - x_0) + o\left(|x - x_0|\right) \tag{2.3.2}$$

holds.

So, in our case, viscosity subsolutions and supersolutions can also be defined as follows:

Definition 2.3.3. Condition (i) holds if and only if

(j) $\rho V(y) \leq H(y, \lambda) \quad \forall y \in O, \forall \lambda \in D^+V(y)$.

Similarly, (ii) holds if and only if

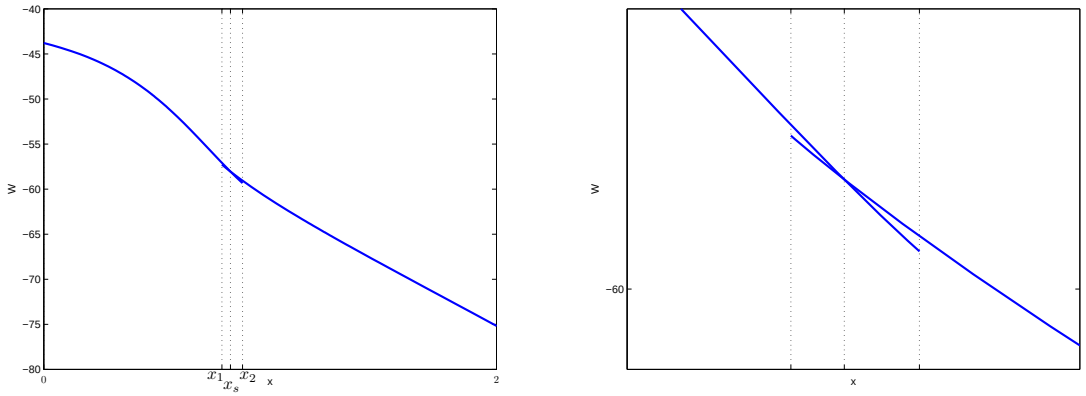

Figure 2.5: The welfare function W provided by the Simple Shooting Method in the case of three equilibrium points. It is multi-valued in $[x_1, x_2]$ and there is an intersection point of W_l and W_r in this domain, which is the Skiba point x_s. In (b) there is a zoom in this domain.

(jj) $\rho V(y) \geq H(y, \mu) \quad \forall y \in O, \forall \mu \in D^- V(y)$.

Our aim is to show that the value function is a viscosity solution of an Optimal HJB equation in $(0, 2)$. To prove this, we take $B = (0, M]^2$, $M > 0$, as it is enough to constraint ourselves to that domain due to physical reasons (this domain captures the physical description of the problem), and we consider the following HJB equation:

$$\rho V_M(x) - H_M(x, DV_M) = 0, \tag{2.3.3}$$

where

$$H_M(x, \lambda) = \sup_{(a_1,a_2)\in(0,M]^2} \left\{ \left(a_1 + a_2 - bx + \frac{x^2}{x^2+1} \right) \lambda + \ln(a_1) + \ln(a_2) - 2x^2 \right\}. \tag{2.3.4}$$

We have the following proposition :

Proposition 2.3.1. *V_M is a viscosity solution of equation (2.3.3) in $(0, 2)$ and this equation admits a Comparison Principle.*

Proof: It can be easily proved using calculus that $f(x, c) = a - bx + \frac{x^2}{x^2+1}$ and $h(x, c) = \ln(a_1) + \ln(a_2) - 2x^2$, where $x \in (0, 2), c = (a_1, a_2) \in (0, M]^2$ and $a = a_1 + a_2$, are continuous in $(0, 2) \times (0, M]^2$, Lipschitz continuous with respect to x, uniformly to c and bounded for all $x \in (0, 2)$ and $c \in (0, M]^2$. Then, using these properties for f and h it is standard theory to prove that the problem is well-posed and that $V_M \in BUC(0, 2)$ (see [5], page 99). From this, using the Dynamic Programming Principle, we deduce that V_M satisfies

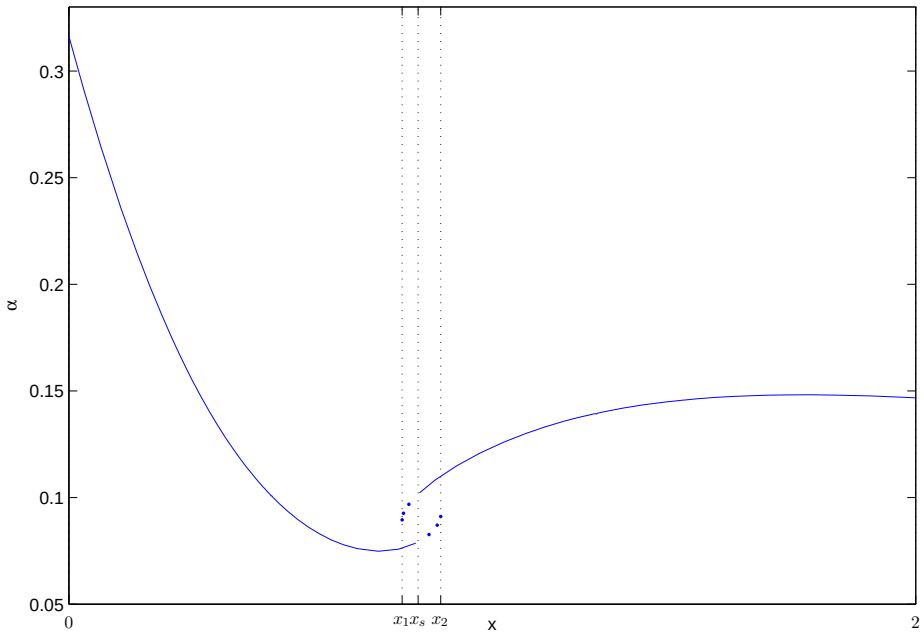

Figure 2.6: Due to the existence of a Skiba point x_s, only the upper trajectory (at the right side of x_s) and the lower trajectory (at the left side of x_s) are kept. The dots show the domain $[x_1, x_2]$ in which α is multi-valued.

equation (2.3.3) in the viscosity sense (see [5], page 104). Finally, there is a Comparison Principle for this equation between viscosity sub- and supersolutions (for its proof see [5], pages 51-54) which is the following: Let J be a bounded, open subset of $(0, 2)$. Assume that $V_{M_1}, V_{M_2} \in C(\bar{J})$ are, respectively, viscosity sub- and supersolution of (2.3.3) in J and $V_{M_1} \leq V_{M_2}$ on ∂J. Then

$$V_{M_1} \leq V_{M_2} \quad \text{in} \quad \bar{J}. \qquad \square$$

Hamiltonian H_M takes a special form depending on the choice of λ, as the following lemma shows:

Lemma 2.3.1.

$$H_M(x,\lambda) = \begin{cases} \left(\frac{x^2}{x^2+1} - bx\right)\lambda - 2\left(\ln(-\lambda) + x^2 + 1\right), & \lambda \leq -\frac{1}{M}, \quad x \in (0,2) \\ \left(2M - bx + \frac{x^2}{x^2+1}\right)\lambda + 2\ln(M) - 2x^2, & \lambda > -\frac{1}{M}, \quad x \in (0,2) \end{cases}.$$

Proof of Lemma: Let

$$g(a_1,a_2)=\left(a_1+a_2-bx+\frac{x^2}{x^2+1}\right)\lambda+\ln(a_1)+\ln(a_2)-2x^2,\quad (a_1,a_2)\in\mathbb{R}^2.$$

The point $\left(-\frac{1}{\lambda},-\frac{1}{\lambda}\right)$ is the only critical point of g in $\mathbb{R}^2$. We consider the following cases:

- $\lambda\le -\frac{1}{M},\quad x\in(0,2)$. Then $-\frac{1}{\lambda}\le M$, so $\left(-\frac{1}{\lambda},-\frac{1}{\lambda}\right)\in(0,M]^2$. Let's suppose that there exist $a_1,a_2\in(0,M]$ such that $g(a_1,a_2)>g\left(-\frac{1}{\lambda},-\frac{1}{\lambda}\right)$. Then

$$\begin{aligned}
&\left(a_1+a_2-bx+\frac{x^2}{x^2+1}\right)\lambda+\ln(a_1)+\ln(a_2)-2x^2>\\
&>\left(-\frac{2}{\lambda}-bx+\frac{x^2}{x^2+1}\right)\lambda+\ln(-\frac{1}{\lambda})+\ln(-\frac{1}{\lambda})-2x^2\\
\Rightarrow\quad &(a_1+a_2)\,\lambda+\ln(a_1)+\ln(a_2)>-2-2\ln(-\lambda)\\
\Rightarrow\quad &a_1\lambda+a_2\lambda+\ln(a_1)+\ln(-\lambda)+\ln(a_2)+\ln(-\lambda)>-2\\
\Rightarrow\quad &a_1\lambda+\ln(-a_1\lambda)+a_2\lambda+\ln(-a_2\lambda)>-2 \qquad (2.3.5)
\end{aligned}$$

We have that $\ln(x)\le x-1\quad\forall x>0$. So,

$$\ln(-a_1\lambda)\le -a_1\lambda-1\Rightarrow\ln(-a_1\lambda)+a_1\lambda\le -1, \qquad (2.3.6)$$

$$\ln(-a_2\lambda)\le -a_2\lambda-1\Rightarrow\ln(-a_2\lambda)+a_2\lambda\le -1. \qquad (2.3.7)$$

Adding (2.3.6) and (2.3.7) we get

$$\ln(-a_1\lambda)+a_1\lambda+\ln(-a_2\lambda)+a_2\lambda\le -2,$$

so, due to (2.3.5), we have a contradiction. We deduce that

$$g(a_1,a_2)\le g\left(-\frac{1}{\lambda},-\frac{1}{\lambda}\right)\quad\forall(a_1,a_2)\in(0,M]^2.$$

We derive that $\left(-\frac{1}{\lambda},-\frac{1}{\lambda}\right)$ is the maximum point for g in $(0,M]^2$. So,

$$\begin{aligned}
H_M(x,\lambda) &= \sup_{(a_1,a_2)\in(0,M]^2} g(a_1,a_2)=\max_{(a_1,a_2)\in(0,M]^2} g(a_1,a_2)=g\left(-\frac{1}{\lambda},-\frac{1}{\lambda}\right)=\\
&= \left(\frac{x^2}{x^2+1}-bx\right)\lambda-2\left(\ln(-\lambda)+x^2+1\right).
\end{aligned}$$

- $\lambda\ge 0,\quad x\in(0,2)$. Then, it is obvious that g is increasing as either a_1 or a_2 is increasing. This means that the maximum point for g in $(0,M]^2$ is obtained for $a_1=a_2=M$, so

$$H_M(x,\lambda)=g(M,M)=\left(2M-bx+\frac{x^2}{x^2+1}\right)\lambda+2\ln(M)-2x^2.$$

- $0 > \lambda > -\frac{1}{M}, \quad x \in (0,2)$. Then $M < -\frac{1}{\lambda}$, so $\left(-\frac{1}{\lambda}, -\frac{1}{\lambda}\right) \notin (0,M]^2$. We have that

$$\sup_{(a_1,a_2)\in(0,M]^2} g(a_1,a_2) = \max_{(a_1,a_2)\in[\varepsilon,M]^2} g(a_1,a_2), \quad \varepsilon > 0 \text{ small}, \tag{2.3.8}$$

because $\lim_{(a_1,a_2)\to(0,0)} g(a_1,a_2) = -\infty$. We deduce that the maximum point of g in $(\varepsilon,M]^2$ will be at the boundary of $[\varepsilon,M]^2$. Using simple calculus, we deduce that

$$\max_{(a_1,a_2)\in[\varepsilon,M]^2} g(a_1,a_2) = g(M,M) = \left(2M - bx + \frac{x^2}{x^2+1}\right)\lambda + 2\ln(M) - 2x^2. \tag{2.3.9}$$

From (2.3.8) and (2.3.9) we deduce that

$$H_M(x,\lambda) = g(M,M) = \left(2M - bx + \frac{x^2}{x^2+1}\right)\lambda + 2\ln(M) - 2x^2. \qquad \square$$

Using Proposition 2.3.1 we have that V_M is a viscosity solution of the following Dirichlet problem:

$$\begin{cases} \rho V_M(x) - H_M(x, DV_M) = 0, & x \in (0,2), \\ V_M(0) = v_0, \quad V_M(2) = v_1, & v_0, v_1 < 0, \end{cases} \tag{2.3.10}$$

where H_M is given by Lemma 2.3.1 ($v_0, v_1 < 0$ due to the physical description of the problem). Some important properties of V_M, which will be used to prove that the value function is a viscosity solution of an Optimal HJB equation in $(0,2)$, are mentioned in the following theorem:

Theorem 2.3.1. *The viscosity solution V_M of the Dirichlet problem (2.3.10) has the following properties:*

1. *The family of functions $\{V_M\}_{M>0}$ is uniformly bounded in $[0,2]$.*
2. *V_M is locally semiconvex in $(0,2)$ for every $M > 0$.*
3. *$D^- V_M(x) \neq \emptyset$ for all $x \in (0,2)$, for all $M > 0$.*
4. *There exists $M_0 \in \mathbb{R}$ such that for every $M \in \mathbb{R}$, $M \geq M_0$, and for every $x \in (0,2)$ we have that, if $\lambda_M \in D^- V_M(x)$ then $\lambda_M \leq -\frac{1}{M}$.*
5. *For every $M \geq M_0$, V_M is a strictly decreasing function on $(0,2)$.*

Proof: 1. Choosing $V_c = c \leq v_0, v_1$ we have:

$$\begin{aligned} & \rho V_c - H_M(x, DV_c) = \rho c - H_M(x,0) = \\ = \;& \rho c - \left(2M - bx + \frac{x^2}{x^2+1}\right)\cdot 0 - 2\ln(M) + 2x^2 = \\ = \;& \rho c - 2\ln(M) + 2x^2 < 0, \end{aligned}$$

taking M sufficiently large ($x \in (0,2)$). We deduce that V_c is a classical subsolution of (2.3.10) ($V_c(0) = c \leq v_0$, $V_c(2) = c \leq v_1$). By the Comparison Principle we deduce that

$$c \leq V_M \quad \text{in } [0,2]. \tag{2.3.11}$$

We now choose $0 < M_0 \leq M$ and $\tilde{V} = \tilde{u}_0 - \frac{1}{M_0}x$, where $\tilde{u}_0$ is a constant (which we will later choose sufficiently large). We have $M_0 \leq M \Rightarrow -\frac{1}{M_0} \leq -\frac{1}{M}$, so

$$\begin{aligned} & \rho\tilde{V} - H_M(x, D\tilde{V}) = \rho\left(\tilde{u}_0 - \frac{1}{M_0}x\right) - H_M\left(x, -\frac{1}{M_0}\right) = \\ = \quad & \rho\left(\tilde{u}_0 - \frac{1}{M_0}x\right) - \left(\frac{x^2}{x^2+1} - bx\right)\left(-\frac{1}{M_0}\right) + 2\ln\left(\frac{1}{M_0}\right) + 2x^2 + 2. \end{aligned}$$

Terms which depend on x are bounded as $x \in (0,2)$, so, choosing $\tilde{u}_0$ sufficiently large we take that $\rho\tilde{V} - H_M(x, D\tilde{V}) > 0$. In addition, $\tilde{u}_0$ is taken sufficiently large so that $\tilde{u}_0 > v_0$ and $\tilde{u}_0 - \frac{2}{M_0} > v_1$. Then, $\tilde{V}(0) = \tilde{u}_0 > v_0$ and $\tilde{V}(2) = \tilde{u}_0 - \frac{2}{M_0} > v_1$. We deduce that $\tilde{V}$ is a classical supersolution of (2.3.10). By the Comparison Principle,

$$V_M \leq \tilde{V} \quad \text{in } [0,2] \Rightarrow V_M \leq \tilde{u}_0 - \frac{1}{M_0}x \leq \tilde{u}_0 \quad \text{in } [0,2]. \tag{2.3.12}$$

From (2.3.11) and (2.3.12) we have that

$$\begin{aligned} & c \leq V_M(x) \leq \tilde{u}_0 \quad \forall x \in [0,2] \ \ \forall M > 0 \Rightarrow \\ \Rightarrow \quad & \{V_M\}_{M>0} \text{ uniformly bounded in } [0,2]. \end{aligned}$$

2. Let $M > 0$. It is sufficient to show that

$$N(x) = -V_M(x) = \inf_{(\alpha_1,\alpha_2)\in A} \int_0^\infty e^{-\rho t} h\left(y_x(t,c), (\alpha_1(t), \alpha_2(t))\right) dt$$

is locally semiconcave in (0,2). Let us recall that $f(x,(a_1,a_2)) = a_1 + a_2 - bx + \frac{x^2}{x^2+1}$, $h(x,(a_1,a_2)) = -\left(\ln(a_1) + \ln(a_2) - 2x^2\right)$ and $B = (0,M]^2$. It can be proved using simple calculus that there is $K_1 > 0$ ($K_1 = b + 4$) such that

$$|f(x_2,c) - f(x_1,c)| \leq K_1|x_2 - x_1|, \quad \forall x_1, x_2 \in [0,2], \ \ \forall c \in (0,M]^2 \tag{2.3.13}$$

and

$$|f_x(x_2,c) - f_x(x_1,c)| \leq 114|x_2 - x_1|, \quad \forall x_1, x_2 \in [0,2], \ \ \forall c \in (0,M]^2. \tag{2.3.14}$$

Moreover, it can easily be proved that

$$\forall R > 0, \quad |h(x_2,c) - h(x_1,c)| \leq 8|x_2 - x_1|, \quad \forall x_1, x_2 \in B_R, \ \ \forall c \in (0,M]^2. \tag{2.3.15}$$

In addition, simple calculations provide that

$$\forall R > 0, \quad h(x,c) + h(y,c) - 2h\left(\frac{x+y}{2}, c\right) \leq |x-y|^2, \quad x, y \in B_R, \ \ c \in (0,M]^2. \tag{2.3.16}$$

The rest of the proof is based on [8] and the proof of Theorem 7.4.11, where a semiconcavity result is obtained for the Bolza problem. Our problem is slightly different (the terminal time is $T = +\infty$ and there is a discount factor ρ), so, in the following, we adjust the proof

to our case. Let $r > 0$ be fixed and let $R > 0$ be such that all trajectories starting from B_r for $t = 0$ ($x = y_x(0, c) \in B_r$) stay inside B_R in $[0, +\infty)$ ($y_x(t, c) \in B_R \ \ \forall t \in [0, +\infty)$). The existence of such R is proven in Lemma 7.1.2 (i) of [8] and the hypotheses of this lemma are satisfied, due to (2.3.13) and to the fact that the control set B can be set equal to $[\varepsilon, M]^2$ for $\varepsilon > 0$ small (as there are no optimal controls near 0), meaning that B is compact. Given x, h such that $x \pm h \in B_r$, let $\tilde{c} : [0, +\infty) \to (0, M]^2$ be an optimal control for x. Let us set

$$y(\cdot) = y_x(\cdot, \tilde{c}), \quad y_-(\cdot) = y_{x-h}(\cdot, \tilde{c}) \quad y_+(\cdot) = y_{x+h}(\cdot, \tilde{c}).$$

Using Lemma 7.1.2 ((ii) and (iii)) of [8] (its hypotheses are satisfied due to (2.3.13), (2.3.14) and the fact that B is compact, as stated before) we have

$$|y_+(s) - y_-(s)| \leq c|h|, \qquad |y_+(s) + y_-(s) - 2y(s)| \leq c|h|^2 \tag{2.3.17}$$

for some constant $c > 0$. Using (2.3.15), (2.3.16) and (2.3.17) and following the proof of Theorem 7.4.11 of [8], we have

$$h\left(y_+(t), \tilde{c}(t)\right) + h\left(y_-(t), \tilde{c}(t)\right) - 2h\left(y(t), \tilde{c}(t)\right) \leq c^2|h|^2 + 8c|h|^2 = C|h|^2, \tag{2.3.18}$$

where C is any constant depending only on r. Thus, the definition of $N(x)$, the optimality of $\tilde{c}$ and (2.3.18) imply that

$$\begin{aligned}
& N(x+h) + N(x-h) - 2N(x) \leq \\
\leq \ & \int_0^{+\infty} e^{-\rho t} \left[h\left(y_+(t), \tilde{c}(t)\right) + h\left(y_-(t), \tilde{c}(t)\right) - 2h\left(y(t), \tilde{c}(t)\right)\right] dt \leq \\
\leq \ & \int_0^{+\infty} e^{-\rho t} \cdot C|h|^2 dt = \frac{C}{\rho}|h|^2 \Rightarrow \\
\Rightarrow \ & N(x+h) + N(x-h) - 2N(x) \leq C_1|h|^2, \quad \text{for every } \ x, h \ \text{ such that } \ x \pm h \in B_r,
\end{aligned}$$

which proves that N is locally semiconcave in $(0, 2)$.

3. Let $M > 0$. From **2** we deduce that V_M is semiconvex in every compact subset of $(0, 2)$. Let $[a, b] \subset (0, 2)$. We consider the set

$$D^* V_M(x) = \left\{ p \in \mathbb{R} : p = \lim_{n \to +\infty} DV_M(x_n), x_n \to x \right\}.$$

Due to the fact that V_M is semiconvex in $[a, b]$, it is a well-known result in nonsmooth analysis (see [3],[9]) that

$$D^- V_M(x) = co D^* V_M(x), \quad \forall x \in [a, b], \tag{2.3.19}$$

where $co D^* V_M(x)$ is the convex hull of $D^* V_M(x)$. In addition, V_M is locally Lipschitz continuous in (a, b) due to its semiconvexity property in $[a, b]$ (see [3],[5] and [8]). By the classical Rademacher theorem, V_M is differentiable almost everywhere in (a, b) with locally bounded gradient. From this we deduce that $D^* V_M(x) \neq \emptyset \ \ \forall x \in (a, b)$. Consequently, $D^- V_M(x) \neq \emptyset \ \ \forall x \in (a, b)$, due to (2.3.19). We conclude that

$$D^- V_M(x) \neq \emptyset \quad \forall x \in (0, 2).$$

4. From **1** we have that there exists $\Lambda > 0$ such that

$$|V_M(x)| \leq \Lambda, \quad \forall x \in (0,2), \ \ \forall M > 0. \tag{2.3.20}$$

V_M is a viscosity solution of (2.3.10) so for $M > 0$, $x \in (0,2)$ and $\lambda_M \in D^- V_M(x)$ we deduce using (2.3.10) and (2.3.20) that there exists $\Lambda_1 > 0$ such that

$$H_M(x, \lambda_M) \leq \Lambda_1. \tag{2.3.21}$$

We now suppose that,

$$\left\{ \begin{array}{c} \forall r \in \mathbb{R} \ \ \exists M_r \in \mathbb{R}, M_r \geq r, \text{ and } \exists x_{M_r} \in (0,2) \text{ and } \lambda_{M_r} \in D^- V_{M_r}(x_{M_r}) \\ \text{such that } \ \lambda_{M_r} > -\frac{1}{M_r}. \end{array} \right. \tag{2.3.22}$$

We have that $a_r = -b x_{M_r} + \frac{{x_{M_r}}^2}{{x_{M_r}}^2+1}$ is bounded $\forall r \in \mathbb{R}$, as $x_{M_r} \in (0,2) \ \ \forall r \in \mathbb{R}$. This means that we can choose r_0 sufficient large so that, due to (2.3.22), M_{r_0} is sufficient large to obtain that $2M_{r_0} - b x_{M_{r_0}} + \frac{{x_{M_{r_0}}}^2}{{x_{M_{r_0}}}^2+1} > 0$. So, from (2.3.22) we deduce that

$$2M_r - b x_{M_r} + \frac{{x_{M_r}}^2}{{x_{M_r}}^2+1} > 0 \quad \forall r \geq r_0. \tag{2.3.23}$$

For $r \geq r_0$ we now have, using Lemma 2.3.1:

$$\begin{aligned} & H_{M_r}(x_{M_r}, \lambda_{M_r}) = \\ \overset{(2.3.22)}{=} \ & \left(2M_r - b x_{M_r} + \frac{{x_{M_r}}^2}{{x_{M_r}}^2+1}\right)\lambda_{M_r} + 2\ln(M_r) - 2{x_{M_r}}^2 \geq \\ \overset{(2.3.23),(2.3.22)}{\geq} \ & \left(2M_r - b x_{M_r} + \frac{{x_{M_r}}^2}{{x_{M_r}}^2+1}\right)\left(-\frac{1}{M_r}\right) + 2\ln(M_r) - 2{x_{M_r}}^2 = \\ = \ & -2 + \frac{1}{M_r}\left(b x_{M_r} - \frac{{x_{M_r}}^2}{{x_{M_r}}^2+1}\right) + 2\ln(M_r) - 2{x_{M_r}}^2 = \\ = \ & -2 + \frac{b x_{M_r}}{M_r} - \frac{1}{M_r}\frac{{x_{M_r}}^2}{{x_{M_r}}^2+1} + 2\ln(M_r) - 2{x_{M_r}}^2 \geq \\ \geq \ & -2 - \frac{1}{M_r} + 2\ln(M_r) - 8. \end{aligned} \tag{2.3.24}$$

Since by (2.3.22)

$$\lim_{r \to +\infty} M_r = +\infty,$$

by taking $r \to +\infty$ in (2.3.24) we have that

$$\lim_{r \to +\infty} H_{M_r}(x_{M_r}, \lambda_{M_r}) = +\infty,$$

which contradicts (2.3.21). So the statement is proved.

5. Let $M \geq M_0$. From **3** we deduce that for $x \in (0,2)$ and $\lambda_M \in D^- V_M(x)$ we have that $\lambda_M \leq -\frac{1}{M} < 0$. So,

$$\lambda_M < 0 \quad \forall x \in (0,2), \ \ \forall \lambda_M \in D^- V_M(x). \tag{2.3.25}$$

Let $x_0 \in (0,2)$. For $x < x_0$, using Definition 2.3.2 of subdifferential, we take that for every $\lambda_{M_0} \in D^- V_M(x_0)$,

$$\begin{aligned} & V_M(x) \geq V_M(x_0) + \lambda_{M_0}(x - x_0) + o(|x - x_0|) \\ \Rightarrow \quad & \frac{V_M(x) - V_M(x_0)}{x - x_0} \leq \lambda_{M_0} - \frac{o(|x - x_0|)}{|x - x_0|} \\ \Rightarrow \quad & \limsup_{x \to x_0^-} \frac{V_M(x) - V_M(x_0)}{x - x_0} \leq \lambda_{M_0}. \end{aligned}$$

Using (2.3.25) we deduce that $\limsup_{x \to x_0^-} \frac{V_M(x) - V_M(x_0)}{x - x_0} < 0$. This means that there exists $\varepsilon > 0$ such that, for every $\delta \in (0, \varepsilon)$, $\frac{V_M(x) - V_M(x_0)}{x - x_0} < 0$ holds for $x \in (x_0 - \delta, x_0)$. So we have that there exists $\delta > 0$ such that $V_M(x) > V_M(x_0)$, $\forall x \in (x_0 - \delta, x_0)$. The choice of $x_0 \in (0,2)$ was arbitrary and we deduce that,

$$\forall x_0 \in (0,2)\ \exists \delta > 0 \text{ such that } V_M(x) > V_M(x_0) \quad \forall x \in (x_0 - \delta, x_0). \tag{2.3.26}$$

We suppose now that V_M is not a strictly decreasing function on $(0,2)$. So, there exist $x_1, x_2 \in (0,2), x_1 < x_2$, such that $V_M(x_1) \leq V_M(x_2)$. According to (2.3.26), $\exists \delta' > 0$ such that $V_M(x) > V_M(x_2)$ $\forall x \in (x_2 - \delta', x_2)$. This means that there exists $x_3 \in (x_2 - \delta', x_2)$ such that $V_M(x_3) > V_M(x_2)$. Obviously $x_1 \notin (x_2 - \delta', x_2)$, so $x_1 < x_2 - \delta' < x_3 \Rightarrow x_1 < x_3$. In addition we have

$$V_M(x_1) < V_M(x_3). \tag{2.3.27}$$

V_M is continuous at $[x_1, x_3]$, so there exists $x_m \in [x_1, x_3]$ such that $V_M(x_m) \geq V_M(x)$ $\forall x \in [x_1, x_3]$. From (2.3.27) we see that $x_m \neq x_1$, so $x_m \in (x_1, x_3]$. This means that, there exists $\theta > 0$ such that $(x_m - \theta, x_m) \subseteq (x_1, x_3]$. From this we deduce that

$$V_M(x_m) \geq V_M(x) \quad \forall x \in (x_m - \theta, x_m). \tag{2.3.28}$$

Applying relation (2.3.26) for x_m, we have that there exists $\sigma > 0$ such that $V_M(x) > V_M(x_m)$, $\forall x \in (x_m - \sigma, x_m)$. Due to (2.3.28) we come to a contradiction. So we conclude that V_M is a strictly decreasing function on $(0,2)$. □

The main result of this section is presented in the following proposition:

Proposition 2.3.2. *The value function is a viscosity solution of*

$$\begin{cases} \rho V(x) - \left(\frac{x^2}{x^2+1} - bx\right) DV + 2\left(\ln(-DV) + x^2 + 1\right) = 0 \quad \textit{in } (0,2), \\ V(0) = v_0, \quad V(2) = v_1. \end{cases} \tag{OHJB}$$

Proof: We will first prove that, $\forall M \geq M_0$, $M \in \mathbb{R}^+$, V_M is a viscosity solution of

$$\begin{cases} \rho V_M(x) - \left(\frac{x^2}{x^2+1} - bx\right) DV_M + 2\left(\ln(-DV_M) + x^2 + 1\right) = 0 \quad \text{in } (0,2), \\ V_M(0) = v_0, \quad V_M(2) = v_1. \end{cases} \tag{2.3.29}$$

Let $x \in (0,2)$. Then, from 3 of Theorem 2.3.1 we have that $D^- V_M(x) \neq \emptyset$. Let $\lambda_M \in D^- V_M(x)$. Then, from 4 of Theorem 2.3.1 we get that

$$\lambda_M \leq -\frac{1}{M}. \tag{2.3.30}$$

We have the following cases:

- $D^+V_M(x) \neq \emptyset$. Then $D^+V_M(x) = D^-V_M(x) = \{DV_M(x)\} = \{\lambda_M\}$. So, V_M is differentiable at x and $DV_M(x) = \lambda_M \leq -\frac{1}{M}$ from (2.3.30). From Proposition 2.3.1 and using Lemma 2.3.1 we conclude that V_M is a viscosity solution of (2.3.29) at x.

- $D^+V_M(x) = \emptyset$. Then it is explicit that V_M is a viscosity subsolution of (2.3.29) at x. From Proposition 2.3.1 we have that V_M is a viscosity supersolution of equation $\rho V_M(x) - H_M(x, DV_M) = 0$ in $(0, 2)$. So, using condition (jj) of Definition 2.3.3 we have that $\rho V_M(x) - H_M(x, \lambda_M) \geq 0$. Using Lemma 2.3.1 and (2.3.30) we get that

$$\rho V_M(x) - \left(\frac{x^2}{x^2+1} - bx\right)\lambda_M - 2\left(\ln(-\lambda_M) + x^2 + 1\right) \geq 0. \tag{2.3.31}$$

  The choice of $\lambda_M \in D^-V_M(x)$ is arbitrary, so from (2.3.31) we deduce that V_M is a viscosity supersolution of (2.3.29) at x. We conclude that V_M is a viscosity solution of (2.3.29) at x.

These two cases cover all $x \in (0, 2)$, so V_M is a viscosity solution of (2.3.29) at $(0, 2)$.
The next step is to show that (OHJB) has a unique viscosity solution in $(0, 2)$. For this, it is sufficient to prove a comparison theorem for

$$\begin{cases} \rho V(x) + H(x, DV) = 0 \quad \text{in } (0, 2), \\ V(0) = v_0, \quad V(2) = v_1, \end{cases} \tag{2.3.32}$$

where

$$H(x, \lambda) = -\left(\frac{x^2}{x^2+1} - bx\right)\lambda + 2\left(\ln(-\lambda) + x^2 + 1\right). \tag{2.3.33}$$

From Theorem 3.1 and Remark 3.3 of Sec. II of [5] we have that, it is sufficient to show that

$$|H(x, p) - H(y, p)| \leq \omega_1\left(|x - y|(1 + |p|)\right), \tag{2.3.34}$$

for $x, y \in (0, 2),\ p \in \mathbb{R}^-$, where $\omega_1 : [0, +\infty) \to [0, +\infty)$ is continuous, nondecreasing, with $\omega_1(0) = 0$.

Let $x, y \in (0, 2),\ p \in \mathbb{R}^-$. Then we have:

$$\begin{aligned}
&|H(x,p) - H(y,p)| = \left|p\left(\frac{y^2}{y^2+1} - by - \frac{x^2}{x^2+1} + bx\right) + 2(x^2 - y^2)\right| \leq \\
\leq\ & |p|b|x-y| + |p|\left|\frac{y^2x^2 + y^2 - x^2y^2 - x^2}{(y^2+1)(x^2+1)}\right| + 2\left|(x-y)(x+y)\right| = \\
=\ & |p|b|x-y| + |p|\left|\frac{(y-x)(y+x)}{(y^2+1)(x^2+1)}\right| + 2|x-y|(x+y) = \\
=\ & |p|b|x-y| + |p|\frac{|y-x|(y+x)}{(y^2+1)(x^2+1)} + 2|x-y|(x+y) \leq \\
\leq\ & |p|b|x-y| + |p||y-x|(y+x) + 2|x-y|(x+y) \leq \\
\leq\ & |p|b|x-y| + 4|p||y-x| + 8|x-y| \leq \\
\leq\ & 8|p|b|x-y| + 8|p||y-x| + 8(b+1)|x-y| = \\
=\ & 8|p||x-y|(b+1) + 8(b+1)|x-y| = \\
=\ & 8(b+1)|x-y|(|p|+1).
\end{aligned} \tag{2.3.35}$$

For $\omega_1 : [0,+\infty) \to [0,+\infty)$, $\omega_1(x) = 8(b+1)x$, we have that ω_1 is continuous, nondecreasing and $\omega_1(0) = 0$. Due to (2.3.35) we get that

$$|H(x,p) - H(y,p)| \leq \omega_1 \left(|x-y|(1+|p|)\right), \qquad \forall x, y \in (0,2), \;\; \forall p \in \mathbb{R}^-$$

and the uniqueness of the viscosity solution of the (OHJB) in $(0,2)$ is proven.
We conclude that, if V is the unique viscosity solution of the (OHJB) in $(0,2)$ satisfying the boundary conditions, then

$$V_M \equiv V \quad \forall M \geq M_0,$$

(which means that $V = \lim_{M \to +\infty} V_M$). Considering $B = (0,M]^2$ for some $M \geq M_0$ from the beginning, in the definition of the optimal control problem and of the welfare function W, we conclude that W is independent of M and $W = V$. The statement is proven. □

Remark 2.3.1. The same conclusion can also be drawn for an arbitrary domain $(0,d)$ instead of $(0,2)$, as the proof does not depend on the boundary of this domain.

2.3.2 Qualitative Analysis Of The Value Function

The value function W is characterized by various properties. We have already mentioned that it is continuous, bounded, locally semiconvex, strictly decreasing on $(0,2)$ and it is a viscosity solution of the (OHJB) equation. Some additional properties are mentioned in the next propositions :

Proposition 2.3.3. *Value function W of the optimal control problem mentioned, has the following properties :*

1. *W is concave at $[0,x_b]$, where x_b (which depends on b) is characterized as follows : If $x'(t) = \alpha(t) - k(x(t))$ is the dynamic system of the specific optimal control problem, then $(0,x_b)$ is the maximal interval for which we have $k'(x) \geq 0$ and $k''(x) < 0$.*
2. *W is $C^1[0,x_b]$ (it is smooth in the area where it is concave).*

Remark 2.3.2. From the properties of x_b it is clear that this is the flip point of the lake, that is, the point at which the lake flips from an oligotrophic state to a eutrophic state, with high equilibrium level of phosphorus and with low level of ecological services.

Remark 2.3.3. In general, if the value function is

$$W(x_0) = \sup_{\alpha \in A} \int_0^\infty e^{-\rho t} \left[U(\alpha(t)) - D(y(t))\right] dt$$

and the dynamic system is in the form of Proposition 2.3.3, then assuming that

- k is nondecreasing and concave at $(0,y_0)$
- U is strictly concave at B

- D is convex and nondecreasing at $(0, y_0)$

we have that W is concave and C^1 at $[0, y_0]$ (see Proposition 1 and Theorem 1 of [31]).

Proof: We have that $k(x) = bx - \frac{x^2}{x^2+1}$ and, using calculus, we deduce that, for every $b \geq 0$ there is a point x_b for which we have $k'(x) \geq 0$ and $k''(x) < 0$ for $x \in (0, x_b)$. The value function is

$$W(x_0) = \max_{(\alpha_1,\alpha_2)\in A} \int_0^\infty e^{-\rho t} \left[\ln(\alpha_1(t)) + \ln(\alpha_2(t)) - 2y^2(t)\right] dt.$$

If $U(a_1, a_2) = \ln(a_1)+\ln(a_2)$ and $D(x) = 2x^2$, then U is strictly concave for every $(a_1, a_2) \in \mathbb{R}^+ \times \mathbb{R}^+$ (proved using the definition of concavity) and D is convex and nondecreasing at $(0, +\infty)$. Using Proposition 1 and Theorem 1 of [31] (see Remark 2.3.3), we deduce claims 1 and 2. □

The next proposition refers to the smoothness of W in the whole domain of definition:

Proposition 2.3.4. *1. The value function W is Lipschitz continuous in $(0, 2)$.*

2. In addition, for every $x_0 \in (0, 2)$, W is either differentiable or it has left and right derivatives $W_x^-(x_0)$ and $W_x^+(x_0)$ at x_0, respectively. For H given in (2.3.33) and $W_x^+(x_0) \neq W_x^-(x_0)$, we have

$$\begin{cases} H(x_0, W_x^-(x_0)) = H(x_0, W_x^+(x_0)) = -\rho W(x_0) \quad \textit{and} \\ H(x_0, l)(W_x^+(x_0) - W_x^-(x_0)) \geq -\rho W(x_0)(W_x^+(x_0) - W_x^-(x_0)) \\ \textit{for every } l \in [\min(W_x^-(x_0), W_x^+(x_0)), \max(W_x^-(x_0), W_x^+(x_0))]. \end{cases} \tag{A}$$

3. For every $x_0 \in (0, 2)$ there exists an $a = a(x_0) > 0$ such that :

(a) If $-\rho W(x_0)$ is not a local extremum value of H, then $W|_{(x_0-a,x_0]} \in C^1((x_0 - a, x_0])$ and $W|_{[x_0,x_0+a)} \in C^1([x_0, x_0 + a))$.

(b) If $-\rho W(x_0)$ is a local extremum value of H, then the following are true on $(x_0-a, x_0]$ (respectively $[x_0, x_0+a)$). Either $W|_{(x_0-a,x_0]} \in C^1((x_0 - a, x_0])$ (respectively $W|_{[x_0,x_0+a)} \in C^1([x_0, x_0 + a))$) or $W_x(x)$ exists for every $(x_0 - a, x_0]$ (respectively $[x_0, x_0 + a)$) except perhaps a sequence $x_n \to x_0$ where $W_x^-(x_n) \neq W_x^+(x_n)$. In this last case, however, we have

$$\lim_{\substack{x\uparrow x_0 \\ x\in(x_0-a,x_0]}} p(x) = W_x^-(x_0) \quad \Big(\textit{respectively} \quad \lim_{\substack{x\downarrow x_0 \\ x\in[x_0,x_0+a)}} p(x) = W_x^+(x_0)\Big),$$

where $p(x) \in \{W_x^-(x), W_x^+(x)\}$.

Proof: 1. Value function W is viscosity solution of the (OHJB) equation. If we write this equation in the form of (2.3.32) with H given in (2.3.33), then, using that $\frac{x^2}{x^2+1} - 0.6x < 0$ for $x \in (0, 2)$, we have that

$$H(x, \lambda) \to -\infty \quad \text{as} \quad \lambda \to -\infty. \tag{2.3.36}$$

Now, for fixed $x \in (0,2)$ consider the function

$$\phi(y) = W(y) + C|y - x|$$

where $C > 0$ is a constant to be chosen later. The fact that W is bounded and continuous in $(0,2)$ implies the existence of $\bar{y} \in (0,2)$ such that

$$\phi(\bar{y}) = \min_{y \in (0,2)} \phi(y).$$

Let $y_1 \in (0,2),\ y_1 \leq x$. Choosing $y_2 \in (0,2),\ y_2 \geq x$ with $|y_2 - x| \leq |y_1 - x|$ we have that

$$\begin{aligned} \phi(y_2) &= W(y_2) + C|y_2 - x| \leq W(y_2) + C|y_1 - x| \leq \\ &\leq W(y_1) + C|y_1 - x| = \phi(y_1) \Rightarrow \\ \Rightarrow \quad & \phi(y_2) \leq \phi(y_1), \end{aligned}$$

using the fact that W is strictly decreasing in $(0,2)$. We deduce that, for every $y_1 \in (0,x]$ there is $y_2 \in [x,2)$ such that $\phi(y_2) \leq \phi(y_1)$, so we have that $\bar{y} \geq x$.

The claim is that $\bar{y} = x$ for C large. If not, then $\bar{y} > x$ and we would have

$$\rho W(\bar{y}) + H(\bar{y}, -C) \geq 0 \tag{2.3.37}$$

since W is a viscosity supersolution of (OHJB) and $y \longrightarrow -C|y - x|$ is differentiable at $y = \bar{y} > x$. We have that $-C \to -\infty$ as $C \to +\infty$, so for sufficiently large C, independent of x, due to (2.3.36) we have that

$$\rho W(\bar{y}) + H(\bar{y}, -C) < 0,$$

which is in contradiction to (2.3.37). Therefore, for such C, x is the point where ϕ has its minimum, so

$$\begin{aligned} & \phi(x) \leq \phi(y) \quad \forall y \in (0,2) \\ \Rightarrow \quad & W(x) \leq W(y) + C|y - x| \quad \forall y \in (0,2) \\ \Rightarrow \quad & W(y) - W(x) \geq -C|y - x| \quad \forall y \in (0,2). \end{aligned}$$

By interchanging the roles of x and y the proof is complete.

2. We can prove, using simple calculus, that :

(i) $H : [0,2] \times \mathbb{R}^- \longrightarrow \mathbb{R}$ is continuous.

(ii) For every $c, M \in \mathbb{R}$ the set

$$H^{-1}(\{c\}) \cap ([-M, M] \times [-M, 0))$$

is either empty or finite.

(iii) The local extremum values (i.e. the local minimum and maximum values) of H are isolated.

Using claims (i)-(iii) and following the proof of Theorem 1 of [30], with minor changes due to the fact that here H is a function of two variables, we prove this claim. So, we apply a similar "blow-up" argument to the equation

$$\rho W(x) + H(x, DW) = 0, \quad x \in (0,2). \tag{2.3.38}$$

More precisely, for $x_0 \in (0,2)$ and $\delta > 0$ sufficiently small, let $W^\delta, x^\delta : [-1,1] \to \mathbb{R}$ be defined by

$$W^\delta(x) = \frac{W(x_0 + \delta x) - W(x_0)}{\delta} \quad \text{and}$$

$$x^\delta(x) = x_0 + \delta x.$$

It turns out that W^δ is a viscosity solution of

$$\delta\rho W^\delta + H\left(x^\delta, W^\delta_x\right) = -\rho W(x_0) \quad \text{in} \quad (-1,1). \tag{2.3.39}$$

So, focusing in a neighborhood of x_0, we pass from equation (2.3.38) to equation (2.3.39) building W^δ, which possesses all the nice properties of W and will help us to reach our aim. Then we show that the family $\left\{W^\delta : \delta > 0\right\}$ converges uniformly, along subsequences, to $W^\infty : [-1,1] \to \mathbb{R}$ and W^∞ inherits all the nice properties of W^δ. From (2.3.39) we deduce that W^∞ satisfies equation

$$H(x_0, W^\infty_x) = -\rho W(x_0) \quad \text{in} \quad (-1,1)$$

which is the analogous of relation (0.5) of [30]. Finally we use lemmas 1.2 and 1.3 of [30] (the fact that here H is a two-variable function does not vary their proofs much) to obtain that W^∞ is unique and either linear or piecewise linear with only one corner at $x = 0$, hence the existence of $W^\pm_x(x_0)$. The first part of (A) is immediate from the properties of W^∞ and the second part is straightforward from the definition of the viscosity solution.
3. Proof of 3. is very similar with the proof of Theorem 2 of [30], with slight changes due to the fact that here H is a two-variable function. □

Remark 2.3.4. An interesting result which occurs from the analytical proof of this theorem (see [30]) in our case is that we have the following sufficient condition for the differentiability of W at x_0 : If

$$A = \{(x,\lambda) \in [x_0 - \delta, x_0 + \delta] \times [-L, 0) : H(x,\lambda) = -\rho W(x_0)\}$$

is a singleton, then W is differentiable at x_0.

Another result concerning the smoothness of W and the Skiba point comes from the next theorem:

Theorem 2.3.2. *If system (2.2.7) has three equilibrium points, we can construct the value function through relation (2.2.9) so that it is a viscosity solution of the (OHJB) in (0,2), with the boundary conditions given in Proposition 2.3.2.*

Proof: Let us recall from Sec. 2.2 that the value function provided by relation (2.2.9) is multi-valued in $[x_1, x_2]$ (W_l and W_r) and the Skiba point x_s is the intersection point of W_l and W_r in this domain (see Fig. 2.5). We construct $\tilde{W}$ so that it is continuous and equals W_l on the left side of x_s and W_r on the right side of x_s, that is,

$$\tilde{W} = \begin{cases} W_l, & x \leq x_s, \\ W_r, & x \geq x_s, \end{cases}$$

(see Fig. 2.7). We have

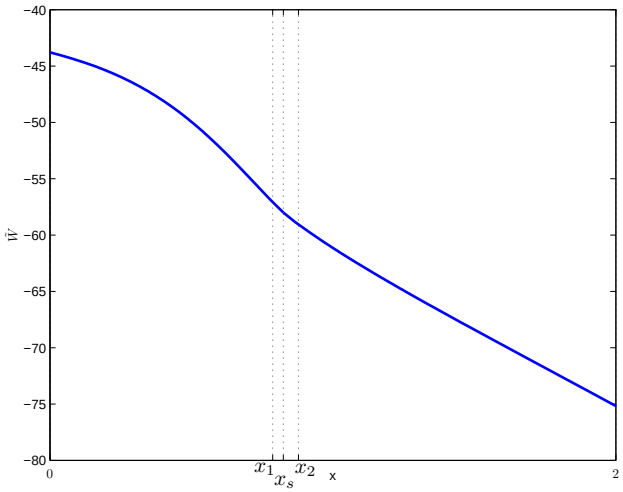

Figure 2.7: The value function is chosen equal to W_l on the left side of x_s and W_r on the right side of x_s (W_l and W_r are calculated by (2.2.9), see Figure 2.5).

$$\begin{cases} \rho W_l(x) + H(x, W_{lx}) = 0, \\ \rho W_r(x) + H(x, W_{rx}) = 0, \end{cases} \tag{2.3.40}$$

where $H(x, \mu)$ is given in (2.3.33). So, W_l and W_r are viscosity solutions of the (OHJB) equation, as they are classical solutions of the (OHJB) in $(0, 2)$. The only thing that remains to show is that $\tilde{W}$ satisfies the viscosity criterion at the Skiba point x_s (where there is a corner due to the jump of the gradient of $\tilde{W}$ at this point). From Fig. 2.7 and using the definition of $D^+\tilde{W}(x)$ we have $D^+\tilde{W}(x_s) = \emptyset$, so $\tilde{W}$ is viscosity subsolution of the (OHJB) at x_s (see condition (j) of Definition 2.3.3). We have $D^-\tilde{W}(x_s) = \left[\tilde{W}_x^-(x_s), \tilde{W}_x^+(x_s)\right]$, as shown in Fig. 2.7 so, in order to prove that $\tilde{W}$ is also a viscosity supersolution of the (OHJB) at x_s, we have to show that $\rho\tilde{W}(x_s) + H(x_s, \mu) \geq 0 \ \forall \mu \in \left[\tilde{W}_x^-(x_s), \tilde{W}_x^+(x_s)\right]$, using condition (jj) of Definition 2.3.3. It can easily be shown that $H(x_s, \mu)$ is concave with respect to μ and, using this property of H, we have:

Let $\mu \in D^-\tilde{W}(x_s) = \left[\tilde{W}_x^-(x_s), \tilde{W}_x^+(x_s)\right]$. Then, there exists $\lambda \in [0,1]$ such that $\mu = \lambda\tilde{W}_x^-(x_s) + (1-\lambda)\tilde{W}_x^+(x_s)$. Now, we have:

$$\begin{aligned}
& \rho\tilde{W}(x_s) + H(x_s,\mu) = \rho\tilde{W}(x_s) + H(x_s, \lambda\tilde{W}_x^-(x_s) + (1-\lambda)\tilde{W}_x^+(x_s)) \geq \\
\geq\ & \rho\tilde{W}(x_s) + \lambda H(x_s, \tilde{W}_x^-(x_s)) + (1-\lambda)H(x_s, \tilde{W}_x^+(x_s)) = \\
=\ & \lambda\rho\tilde{W}(x_s) + (1-\lambda)\rho\tilde{W}(x_s) + \lambda H(x_s, \tilde{W}_x^-(x_s)) + (1-\lambda)H(x_s, \tilde{W}_x^+(x_s)) \Rightarrow \\
\Rightarrow\ & \rho\tilde{W}(x_s) + H(x_s,\mu) \geq \lambda\left(\rho\tilde{W}(x_s) + H(x_s, \tilde{W}_x^-(x_s))\right) + \\
& \qquad +(1-\lambda)\left(\rho\tilde{W}(x_s) + H(x_s, \tilde{W}_x^+(x_s))\right) \qquad (2.3.41)
\end{aligned}$$

Using the definition of $\tilde{W}$ and (2.3.40) we derive that

$$\begin{cases} \rho\tilde{W}(x_s) + H(x_s, \tilde{W}_x^-(x_s)) = 0, \\ \rho\tilde{W}(x_s) + H(x_s, \tilde{W}_x^+(x_s)) = 0. \end{cases} \qquad (2.3.42)$$

From (2.3.41) and (2.3.42) we conclude that

$$\rho\tilde{W}(x_s) + H(x_s,\mu) \geq 0,$$

so $\tilde{W}$ is a viscosity supersolution of (OHJB) at x_s. □

Remark 2.3.5. As values of $\tilde{W}$ at the two saddle points are known (see (2.2.8)) there is a boundary condition for $\tilde{W}$, so there is a unique viscosity solution in the domain between them (see the proof of Proposition 2.3.2). From Theorem 2.3.2 and Proposition 2.3.2 we conclude that the value function W is differentiable at $[x_{s1}, x_{s2}]\backslash\{x_s\}$.

2.4 Numerical Investigation Of The Control Problem By Discretizing The Viscosity Solution

2.4.1 Numerical Schemes

As we have explained in Sec. 2.2, the classical way to obtain the welfare function (2.1.3) is by first constructing the stable manifolds of the optimal dynamical system (2.2.7) and then integrating the function $-\frac{2}{\alpha(x)}$, see (2.2.9). The scope of this section is to present an alternative, more robust, method of approximating numerically the welfare function through convergent monotone schemes by approximating the viscosity solution of the (OHJB). Given that the only boundary conditions available are the welfare values at the saddle points given by (2.2.8), we construct three different finite difference schemes: The "forward" scheme which is

$$\begin{cases} W_{i+1} = \Delta x \cdot \frac{\rho W_{i+1} + 2\left(\ln\left(-\frac{W_{i+1}-W_i}{\Delta x}\right) + {x_{i+1}}^2 + 1\right)}{\frac{{x_{i+1}}^2}{{x_{i+1}}^2+1} - 0.6x_{i+1}} + W_i, \quad i = 0, 1\ldots, N-1, \\ W_0 = W(x_{s0}), \end{cases} \qquad (2.4.1)$$

where $\Delta x = \frac{2-x_{s0}}{N}$ and $x_{i+1} = x_i + \Delta x,\ i = 0, \dots, N-1,\ \ (x_0 = x_{s0})$. The "backward" scheme, which is

$$\begin{cases} W_i = \Delta y \cdot e^{\frac{\left(\frac{{x_i}^2}{{x_i}^2+1} - 0.6x_i\right)(W_{i+1}-W_i) - \rho\Delta y \cdot W_i - 2\left({x_i}^2+1\right)\Delta y}{2\Delta y}} + W_{i+1}, \quad i = -1, -2, \dots, -M, \\ W_0 = W(x_{s0}), \end{cases} \tag{2.4.2}$$

where $\Delta y = \frac{x_{s0}-0}{M}$ and $x_{i-1} = x_i - \Delta y,\ i = 0, -1, \dots, -M+1,\ \ (x_0 = x_{s0})$. In these two schemes, we approximate $W(x_i)$ with $W_i,\ i = -M, \dots, 0, 1, \dots, N$. The "upwind" scheme, which is

$$\begin{cases} W_i^{(l+1)} = \dfrac{a_i \frac{W_i^{(l+1)} - W_{i-1}^{(l)}}{\Delta z} - 2\left(\ln\left(-\frac{W_{i+1}^{(l)} - W_i^{(l+1)}}{\Delta z}\right) + \beta_i\right)}{\rho}, \quad i = 1, 2, \dots, L-1,\ \ l = 0, 1, 2, \dots \\ W_0^{(r)} = W(x_{s1}), \quad W_L^{(r)} = W(x_{s2}), \quad r = 0, 1, 2, \dots \\ W_i^{(0)},\ i = 1, 2, \dots, L-1 \quad \text{is linear interpolation of} \quad W_0^{(0)}, W_L^{(0)}, \end{cases} \tag{2.4.3}$$

where $\Delta z = \frac{x_{s2}-x_{s1}}{L}$.

In the case of one saddle point $x_{s0} \in (0, 2)$, we use the backward scheme in $(0, x_{s0}]$ and the forward scheme in $[x_{s0}, 2]$. In the case of two saddle points $x_{s1}, x_{s2} \in (0, 2)$ we use the upwind scheme in $[x_{s1}, x_{s2}]$ and the forward and backward schemes in the intervals $[x_{s2}, 2)$ and $(0, x_{s1}]$, respectively.

The above three implicit schemes can be iteratively solved and their convergence is guaranteed by fixed point arguments which are presented on Sec. 2.4.2. We next explain the way the above numerical schemes are derived.

First we calculate the saddle points and the initial condition of the (OHJB) equation. For the forward scheme, derivative $DW(x_{i+1})$ in (OHJB) is replaced by the backward finite-difference approximation $DW(x_{i+1}) \simeq \frac{W(x_{i+1})-W(x_i)}{\Delta x}$, so (OHJB) at x_{i+1} becomes

$$\rho W_{i+1} = \left(\frac{{x_{i+1}}^2}{{x_{i+1}}^2+1} - 0.6x_{i+1}\right)\frac{W_{i+1}-W_i}{\Delta x} - 2\left(\ln\left(-\frac{W_{i+1}-W_i}{\Delta x}\right) + {x_{i+1}}^2 + 1\right)$$

and, solving this to the first W_{i+1} of the right part, we take (2.4.1). For the backward scheme, derivative $DW(x_i)$ in (OHJB) is replaced by the forward finite-difference approximation $DW(x_i) \simeq \frac{W(x_{i+1})-W(x_i)}{\Delta y}$, so (OHJB) at x_i becomes

$$\rho W_i = \left(\frac{{x_i}^2}{{x_i}^2+1} - 0.6x_i\right)\frac{W_{i+1}-W_i}{\Delta y} - 2\left(\ln\left(-\frac{W_{i+1}-W_i}{\Delta y}\right) + {x_i}^2 + 1\right)$$

and, solving this to the second W_i of the right part, we take (2.4.2).

For the upwind difference scheme, the first from the left derivative $DW(x_i)$ in (OHJB) is replaced by the backward finite-difference approximation $DW(x_i) \simeq \frac{W(x_i)-W(x_{i-1})}{\Delta z}$, while the other derivative $DW(x_i)$ is replaced by the forward finite-difference approximation $DW(x_i) \simeq \frac{W(x_{i+1})-W(x_i)}{\Delta z}$. So, (OHJB) at x_i becomes

$$\rho W_i = \left(\frac{{x_i}^2}{{x_i}^2+1} - 0.6x_i\right)\frac{W_i-W_{i-1}}{\Delta z} - 2\left(\ln\left(-\frac{W_{i+1}-W_i}{\Delta z}\right) + {x_i}^2 + 1\right).$$

Solving this to the W_i of the left part and putting $a_i = \frac{{x_i}^2}{{x_i}^2+1} - 0.6x_i$ and $\beta_i = {x_i}^2 + 1$, we result in (2.4.3).

We now have the following convergence theorem:

Theorem 2.4.1. *The numerical schemes derived above are consistent and monotone schemes. In addition, they are stable and converge to the correct viscosity solution limit.*

Proof: The proof of this theorem consists of the following steps :

- First, we show that numerical schemes (2.4.1), (2.4.2) and (2.4.3) are consistent. This is done with the classical way for finite difference methods. We write scheme (2.4.1) with $W(x_{i+1})$ in place of W_{i+1}, so we have an error r_{i+1} added at the end of this equation. Subtracting this from (OHJB) equation and using Taylor expansion and inequality $\ln(x) \leq x - 1,\ x \in \mathbb{R}$, we deduce that

$$\max_{0\leq i\leq N-1} |r_{i+1}| \leq Ch^2,$$

  where C is a constant. The same procedure is followed for schemes (2.4.2), (2.4.3), as well. This relation shows the consistency of the schemes.

- Numerical scheme (2.4.1) is an approximation scheme of the form

$$S\left(r, x, u^r(x), u^r\right) = 0 \quad \text{in } \bar{\Omega},$$

  where $S : \mathbb{R}^+ \times \bar{\Omega} \times \mathbb{R} \times B(\bar{\Omega}) \longrightarrow \mathbb{R}$ is locally bounded ($\mathbb{R}^+ \equiv [0, \infty)$ and $\Omega \subseteq \mathbb{R}^n$ is open and bounded). Here, $r = \Delta x, x = x_{i+1}$ and u^r is a function defined on $\Delta_{\Delta x} = \{x_i : i = 0, \ldots, N\}$ by $u^r(x_{i+1}) = W_{i+1}$. Then, numerical scheme (2.4.1) is written as

$$S\left(\Delta x, x_{i+1}, W_{i+1}, W\right) = 0,$$

  where

$$S(k, y, t, u) = t - u_i - k\frac{\rho t + 2\left[\ln\left(-\frac{t-u_i}{k}\right) + y^2 + 1\right]}{\frac{y^2}{y^2+1} - 0.6y},$$

  with $k \geq 0, y \in \Delta_{\Delta x}, t \in \mathbb{R}$ and $u \in B(\Delta_{\Delta x})$. The same is done for numerical schemes (2.4.2), (2.4.3).

- Numerical scheme (2.4.1) is monotone. For this we must show that

$$S(k, y, t, u) \leq S(k, y, t, w) \quad \text{if } u \geq w,$$

  for all $k \geq 0, y \in \Delta_{\Delta x}, t \in \mathbb{R}$ and $u, w \in B(\Delta_{\Delta x})$. We have :

$$\frac{dS}{du_i} = -1 - \frac{2k}{\frac{y^2}{y^2+1} - 0.6y}\left(-\frac{k}{t-u_i}\right)\frac{1}{k} = -1 + \frac{2k}{\left(\frac{y^2}{y^2+1} - 0.6y\right)(t-u_i)}. \tag{2.4.4}$$

  An a priori restriction for $W_i, i = 0, \ldots, N$ that we will accept now and also use later is that

$$W_{i+1} - W_i < \frac{(2+\varepsilon)\Delta x}{\frac{{x_{i+1}}^2}{{x_{i+1}}^2+1} - 0.6x_{i+1}},$$

$\varepsilon > 0$ small. So, using this we have

$$t - u_i < \frac{(2+\varepsilon)k}{\frac{y^2}{y^2+1} - 0.6y} \Rightarrow \frac{1}{t-u_i} > \frac{\frac{y^2}{y^2+1} - 0.6y}{(2+\varepsilon)k}$$

$$\Rightarrow \quad \frac{2k}{\left(\frac{y^2}{y^2+1} - 0.6y\right)(t-u_i)} < \frac{2}{2+\varepsilon} < 1 \Rightarrow \frac{2k}{\left(\frac{y^2}{y^2+1} - 0.6y\right)(t-u_i)} - 1 < 0.$$

From (2.4.4) we deduce that scheme (2.4.1) is monotone. The same is done for numerical schemes (2.4.2), (2.4.3).

- Consistent and monotone schemes for the H-J equations are stable and converge to the correct viscosity solution (see [51], page 104).

The theorem is proved. □

From the above theorem, we have that

$$W_i{}^{\Delta x} \to W(x_i),\ i = 1, 2, \ldots, N, \text{ as } \Delta x \to 0,$$

$$W_i{}^{\Delta y} \to W(x_i),\ i = -1, -2, \ldots, -M, \text{ as } \Delta y \to 0.$$

$$W_i{}^{\Delta z} \to W(x_i),\ i = 1, 2, \ldots, L, \text{ as } \Delta z \to 0.$$

2.4.2 Iterative Method

We next try to find $W_i,\ i = -M, \ldots, -1, 1, \ldots, N$ in the case of one equilibrium point. For this case, we have the following theorem :

Proposition 2.4.1. *Function* $g_1 : \left[W_{lb}, W_i + \frac{(2+\varepsilon)\Delta x}{a_{i+1}}\right] \to \left[W_{lb}, W_i + \frac{(2+\varepsilon)\Delta x}{a_{i+1}}\right]$, *where*

$$g_1(x) = \frac{\Delta x}{a_{i+1}}\left(\rho x + 2\left[\ln\left(-\frac{x - W_i}{\Delta x}\right) + \beta_{i+1}\right]\right) + W_i$$

is a contraction mapping for $i = 0, 1, \ldots, N-1$ *and function* $g_2 : \left[W_{i+1}, W_{i+1} - \frac{2\Delta y}{a_i}\right] \to \left[W_{i+1}, W_{i+1} - \frac{2\Delta y}{a_i}\right]$, *where*

$$g_2(x) = \Delta y \cdot e^{\frac{a_i(W_{i+1} - x) - \rho\Delta y \cdot x - 2\beta_i \Delta y}{2\Delta y}} + W_{i+1}$$

is a contraction mapping for $i = -1, -2, \ldots, -M$, *where* $a_{i+1} = \frac{{x_{i+1}}^2}{{x_{i+1}}^2+1} - 0.6x_{i+1}$, $\beta_{i+1} = {x_{i+1}}^2 + 1,\ i = -M-1, \ldots, 0, 1, \ldots, N-1$ *for specific* $\Delta x, \Delta y,\ \varepsilon > 0$ *small and* W_{lb} *the lower bound of* $W_i,\ i = -M, \ldots, 0, 1, \ldots, N$, *if the following conditions are satisfied :*

- $\rho \le \frac{k + (2+\varepsilon) - 2\ln\left(-\frac{2+\varepsilon}{a_{i+1}}\right) - 2\beta_{i+1}}{W_i}$ $(\varepsilon, k > 0$ *arbitrary small),*
  $i = 0, \ldots, N-1$ $\qquad (A)$

- $\rho < \min\left\{ \frac{(-2)\left[\ln\left(-\frac{2}{a_i}\right)+1-\beta_i\right]}{W_{i+1}}, -\frac{a_i}{\Delta y} \right\} \quad i = -M, \ldots, -1$ (B)

- $\Delta x \leq -\frac{a_{i+1}}{\rho} \cdot \frac{2\ln\left(-\frac{2+\varepsilon}{a_{i+1}}\right)+2\beta_{i+1}-(2+\varepsilon)+\rho W_i}{2+\varepsilon} \quad i = 0, \ldots, N-1$ (C)

- $W_{lb} = \frac{\rho W_0 - 2}{\rho}$ (D)

Then, ${W_{i+1}}^{(k+1)} = g_1\left({W_{i+1}}^{(k)}\right) \in \left[W_{lb}, W_i + \frac{(2+\varepsilon)\Delta x}{a_{i+1}}\right] \quad \forall k \in \mathbb{N},\ i = 0, 1, \ldots, N-1,$ *with* ${W_{i+1}}^{(0)} = W_i + \frac{(2+\varepsilon)\Delta x}{a_{i+1}}$ *and the sequence* ${W_{i+1}}^{(k+1)}$ *converges to* W_{i+1} *and* ${W_i}^{(k+1)} = g_2\left({W_i}^{(k)}\right) \in \left[W_{i+1}, W_{i+1} - \frac{2\Delta y}{a_i}\right] \quad \forall k \in \mathbb{N},\ i = -1, -2, \ldots, -M,$ *with* ${W_i}^{(0)} = W_{i+1}$ *and the sequence* ${W_i}^{(k+1)}$ *converges to* W_i*, as long as the following inequalities hold:*

- $|W_{i+1} - W_i| > -\frac{(2+\varepsilon)\Delta x}{a_{i+1}},\ i = 0, 1, \ldots, N-1$ *and*
  $|W_{i+1} - W_i| \leq -\frac{2\Delta y}{a_i},\ i = -1, -2, \ldots, -M.$ $(E1)$

- $W_N - W_{lb} \geq -\frac{25\Delta x}{\max\{a_{i+1}\}} > 0$ $(E2)$

Proof: We will prove the result for the forward scheme, i.e. for function g_1. We take $x, y \in \left[W_{lb}, W_i + \frac{(2+\varepsilon)\Delta x}{a_{i+1}}\right]$ with $x < y$. Then

$$g_1(x) - g_1(y) = \frac{\Delta x}{a_{i+1}} \left(\rho(x-y) + 2\ln\left(\frac{-x+W_i}{-y+W_i}\right)\right). \tag{2.4.5}$$

If $f(x) = \frac{x^2}{x^2+1} - 0.6x$ then, using calculus, we deduce that $f(x) < 0,\ \forall x > 0$. So,

$$a_i < 0, \quad i = 0, \ldots, N. \tag{2.4.6}$$

We will prove that $g_1(x)$ is increasing in $\left[W_{lb}, W_i + \frac{(2+\varepsilon)\Delta x}{a_{i+1}}\right]$:
We have ${g_1}'(x) = \frac{\rho(x-W_i)\Delta x + 2\Delta x}{a_{i+1}(x-W_i)}$ and

$$\begin{aligned} \rho(x-W_i)\Delta x + 2\Delta x &= \Delta x\left(\rho(x-W_i)+2\right) \geq \Delta x\left(\rho(W_{lb}-W_0)+2\right) \\ &\overset{(D)}{=} \Delta x\left(\rho\left(\frac{\rho W_0 - 2}{\rho} - W_0\right) + 2\right) \\ &= \Delta x\left(\rho W_0 - 2 - W_0\rho + 2\right) = 0 \\ &\Rightarrow \rho(x-W_i)\Delta x + 2\Delta x \geq 0. \end{aligned}$$

In addition $a_{i+1}(x - W_i) > 0$ due to (2.4.6), so ${g_1}'(x) \geq 0$ in $\left[W_{lb}, W_i + \frac{(2+\varepsilon)\Delta x}{a_{i+1}}\right]$. Using inequality $\ln(x) \leq x - 1,\ x \in \mathbb{R}^+$, we have from (2.4.5), (2.4.6):

$$\begin{aligned} g_1(x) - g_1(y) &\geq \frac{2\Delta x}{a_{i+1}} \ln\left(\frac{-x+W_i}{-y+W_i}\right) \geq \frac{2\Delta x}{a_{i+1}}\left(\frac{-x+W_i}{-y+W_i} - 1\right) \\ &= \frac{2\Delta x}{a_{i+1}}\left(\frac{y-x}{-y+W_i}\right). \end{aligned}$$

Since function g_1 is increasing, we have

$$\begin{aligned} -|g_1(x) - g_1(y)| &\geq \frac{2\Delta x}{a_{i+1}} \left(\frac{|y-x|}{-y+W_i} \right) \\ \Rightarrow \quad |g_1(x) - g_1(y)| &\leq -\frac{2\Delta x}{a_{i+1}(-y+W_i)} |y-x|. \end{aligned} \tag{2.4.7}$$

If $m(x) = -\frac{2\Delta x}{a_{i+1}(-x+W_i)}$, then $m'(x) = -\frac{2\Delta x}{a_{i+1}} \left(\frac{1}{(-x+W_i)^2} \right) > 0$ for $x \in \left[W_{lb}, W_i + \frac{(2+\varepsilon)\Delta x}{a_{i+1}} \right]$, due to (2.4.6). So,

$$\begin{aligned} y &\leq W_i + \frac{(2+\varepsilon)\Delta x}{a_{i+1}} \\ \Rightarrow m(y) &\leq m\left(W_i + \frac{(2+\varepsilon)\Delta x}{a_{i+1}} \right) = -\frac{2\Delta x}{a_{i+1}\left(-W_i - \frac{(2+\varepsilon)\Delta x}{a_{i+1}} + W_i \right)} = \frac{2}{2+\varepsilon} \\ \Rightarrow m(y) &\leq \frac{2}{2+\varepsilon}. \end{aligned} \tag{2.4.8}$$

So, from (2.4.7) using (2.4.8) we have

$$|g_1(x) - g_1(y)| \leq \frac{2}{2+\varepsilon} |x-y|.$$

If $x > y$ following the previous techniques, we end up with the same inequality. So we have that

$$|g_1(x) - g_1(y)| \leq \frac{2}{2+\varepsilon} |x-y| \quad \forall x, y \in \left[W_{lb}, W_i + \frac{(2+\varepsilon)\Delta x}{a_{i+1}} \right].$$

We conclude that g_1 is a contraction in $\left[W_{lb}, W_i + \frac{(2+\varepsilon)\Delta x}{a_{i+1}} \right]$. We next show that

$$g_1\left(\left[W_{lb}, W_i + \frac{(2+\varepsilon)\Delta x}{a_{i+1}} \right] \right) \subseteq \left[W_{lb}, W_i + \frac{(2+\varepsilon)\Delta x}{a_{i+1}} \right]. \tag{2.4.9}$$

Because g_1 is increasing and continuous, it is sufficient to show that

$$\left[g_1(W_{lb}), g_1\left(W_i + \frac{(2+\varepsilon)\Delta x}{a_{i+1}} \right) \right] \subseteq \left[W_{lb}, W_i + \frac{(2+\varepsilon)\Delta x}{a_{i+1}} \right].$$

For this, it is sufficient to show that

$$g_1(W_{lb}) \geq W_{lb} \tag{2.4.10}$$

and

$$g_1\left(W_i + \frac{(2+\varepsilon)\Delta x}{a_{i+1}} \right) \leq W_i + \frac{(2+\varepsilon)\Delta x}{a_{i+1}} \tag{2.4.11}$$

$\Big($then, $g_1\left(W_i+\frac{(2+\varepsilon)\Delta x}{a_{i+1}}\right)\geq g_1(W_{lb})\geq W_{lb}$ and $g_1(W_{lb})\leq g_1\left(W_i+\frac{(2+\varepsilon)\Delta x}{a_{i+1}}\right)\leq W_i+\frac{(2+\varepsilon)\Delta x}{a_{i+1}}\Big)$. Relation (2.4.10) is written as

$$\begin{aligned}
&\frac{\Delta x}{a_{i+1}}\left(\rho W_{lb}+2\left[\ln\left(-\frac{W_{lb}-W_i}{\Delta x}\right)+\beta_{i+1}\right]\right)+W_i\geq W_{lb}\\
\Leftrightarrow\quad &\frac{W_{lb}-W_i}{\Delta x}\leq\frac{1}{a_{i+1}}\left(\rho W_{lb}+2\left[\ln\left(-\frac{W_{lb}-W_i}{\Delta x}\right)+\beta_{i+1}\right]\right)\\
\Leftrightarrow\quad &2\ln\left(\frac{W_i-W_{lb}}{\Delta x}\right)+2\beta_{i+1}+\rho W_{lb}+\frac{W_i-W_{lb}}{\Delta x}a_{i+1}\leq 0\\
\Leftrightarrow\quad &2\ln\left(\frac{W_i-W_{lb}}{\Delta x}\right)+a_{i+1}\frac{W_i-W_{lb}}{\Delta x}+\rho W_{lb}+2\beta_{i+1}\leq 0. \qquad (2.4.12)
\end{aligned}$$

If $h(x)=2\ln(x)+a_{i+1}x+10,\ x>0$, then h has global maximum at $x_0=-\frac{2}{a_{i+1}}$ and is decreasing for $x\geq x_0$. In addition, $\lim_{x\to+\infty}h(x)=-\infty$. If $h(x_0)\leq 0$ then $h(x)\leq 0\ \forall x>0$ and (2.4.12) holds (as the left part of it is smaller than $h(x)$). If $h(x_0)>0$, then we have: Supposing that $h\left(-\frac{25}{a_{i+1}}\right)\geq 0$, then

$$\begin{aligned}
&2\ln\left(-\frac{25}{a_{i+1}}\right)+a_{i+1}\left(-\frac{25}{a_{i+1}}\right)+10\geq 0\Rightarrow\ln\left(-\frac{25}{a_{i+1}}\right)\geq 7.5\\
\Rightarrow\quad &-\frac{25}{a_{i+1}}\geq e^{7.5}\Rightarrow a_{i+1}\geq-\frac{25}{e^{7.5}}\approx-0.014,
\end{aligned}$$

which is a contradiction, because we can easily see that $\max_{0\leq i\leq N}\{a_i\}\approx-0.0897$. So, $h\left(-\frac{25}{a_{i+1}}\right)<0$ and $-\frac{25}{a_{i+1}}>x_0$ which means that $h(x)<0\ \forall x\geq-\frac{25}{a_{i+1}}$. This means that (2.4.12) holds if $\frac{W_i-W_{lb}}{\Delta x}\geq-\frac{25}{a_{i+1}}$. But this is true, because

$$\frac{W_i-W_{lb}}{\Delta x}\geq\frac{W_N-W_{lb}}{\Delta x}\overset{(E2)}{\geq}-\frac{25}{\max\{a_{i+1}\}}\geq-\frac{25}{a_{i+1}}.$$

So, (2.4.12) is true and so is (2.4.10). Relation (2.4.11) is written

$$\begin{aligned}
&\frac{\Delta x}{a_{i+1}}\left(\rho W_i+\frac{(2+\varepsilon)\rho\Delta x}{a_{i+1}}+2\left[\ln\left(-\frac{2+\varepsilon}{a_{i+1}}\right)+\beta_{i+1}\right]\right)+W_i\leq\\
&\leq W_i+\frac{(2+\varepsilon)\Delta x}{a_{i+1}}\\
\Leftrightarrow\quad &\rho W_i+\frac{(2+\varepsilon)\rho\Delta x}{a_{i+1}}+2\ln\left(-\frac{2+\varepsilon}{a_{i+1}}\right)+2\beta_{i+1}\geq 2+\varepsilon\\
\Leftrightarrow\quad &2\ln\left(-\frac{2+\varepsilon}{a_{i+1}}\right)+\frac{(2+\varepsilon)\rho\Delta x}{a_{i+1}}+\rho W_i+2\beta_{i+1}-(2+\varepsilon)\geq 0
\end{aligned}$$

Using condition (C), the left-hand side of the above inequality is greater than

$$2\ln\left(-\frac{2+\varepsilon}{a_{i+1}}\right)+(2+\varepsilon)\left(\frac{-2\ln\left(-\frac{2+\varepsilon}{a_{i+1}}\right)-2\beta_{i+1}+(2+\varepsilon)-\rho W_i}{2+\varepsilon}\right)+\rho W_i+2\beta_{i+1}-(2+\varepsilon),$$

which is equal to 0. We thus conclude that (2.4.11) holds. So, relation (2.4.9) holds and we showed that $g_1 : \left[W_{lb}, W_i + \frac{(2+\varepsilon)\Delta x}{a_{i+1}}\right] \to \left[W_{lb}, W_i + \frac{(2+\varepsilon)\Delta x}{a_{i+1}}\right]$ is a contraction mapping for $i = 0, 1, \ldots, N-1$. This means that g_1 has a unique fixed point at this domain, which is W_{i+1} (because W_{i+1} is a fixed point for g_1, due to relation (2.4.1) and $W_{i+1} \in \left[W_{lb}, W_i + \frac{(2+\varepsilon)\Delta x}{a_{i+1}}\right]$, due to inequality (E1)). In addition, ${W_{i+1}}^{(k+1)} = g_1\left({W_{i+1}}^{(k)}\right) \in \left[W_{lb}, W_i + \frac{(2+\varepsilon)\Delta x}{a_{i+1}}\right] \quad \forall k \in \mathbb{N},\ i = 0, 1, \ldots, N-1$ with ${W_{i+1}}^{(0)} = W_i + \frac{(2+\varepsilon)\Delta x}{a_{i+1}}$ and converges to that unique fixed point of g_1 at this domain, which is W_{i+1}.
In a very similar way and using condition (B) instead of (A) and (C), it can be proved that $g_2 : \left[W_{i+1}, W_{i+1} - \frac{2\Delta y}{a_i}\right] \to \left[W_{i+1}, W_{i+1} - \frac{2\Delta y}{a_i}\right]$ is a contraction mapping for $i = -1, -2, \ldots, -M$, and that, similarly, ${W_i}^{(k+1)} = g_2\left({W_i}^{(k)}\right) \in \left[W_{i+1}, W_{i+1} - \frac{2\Delta y}{a_i}\right] \forall k \in \mathbb{N},\ i = -1, -2, \ldots, -M$, with ${W_i}^{(0)} = W_{i+1}$ and converges to W_i. □

Remark 2.4.1. Condition (A) shows that

$$\rho W_i - (2+\varepsilon) + 2\ln\left(-\frac{2+\varepsilon}{a_{i+1}}\right) + 2\beta_{i+1} \geq k, \quad k > 0 \text{ small},$$

so it ensures that the right part of (C) is positive and we can select Δx small enough so that (C) is satisfied. In addition, it is easily seen that, for $k, \varepsilon > 0$ small enough, the right part of (A) is positive, so we can find $\rho > 0$ which satisfies it.

So, the iterative methods that we have in the case of one saddle point, are:

$$\begin{cases} {W_{i+1}}^{(k+1)} = \frac{\Delta x}{a_{i+1}}\left(\rho {W_{i+1}}^{(k)} + 2\left[\ln\left(-\frac{{W_{i+1}}^{(k)} - W_i}{\Delta x}\right) + \beta_{i+1}\right]\right) + W_i, \\ {W_{i+1}}^{(0)} = W_i + \frac{(2+\varepsilon)\Delta x}{a_{i+1}}, \quad i = 0, 1, \ldots, N-1 \end{cases} \tag{2.4.13}$$

which is for the forward scheme and

$$\begin{cases} {W_i}^{(k+1)} = \Delta y \cdot e^{\frac{a_i({W_{i+1}} - {W_i}^{(k)}) - \rho\Delta y \cdot {W_i}^{(k)} - 2\beta_i\Delta y}{2\Delta y}} + W_{i+1} \\ {W_i}^{(0)} = W_{i+1}, \quad i = -1, -2, \ldots, -M \end{cases} \tag{2.4.14}$$

which is for the backward scheme. From the above theorem we have that

$$\lim_{k\to\infty} {W_{i+1}}^{(k)} = W_{i+1}, \quad i = -M-1, \ldots, 0, 1, \ldots, N-1.$$

For the case of two saddle points, we have the following theorem:

Proposition 2.4.2. *The finite difference equation (2.4.3) has a unique solution with respect to $W_i^{(l+1)}$, if Δz satisfies the following condition:*

$$\Delta z \leq \min_{i=1,\ldots,L-1}\left\{\left(W_{i-1}^{(l)} - W_{i+1}^{(l)}\right)e^{\frac{\rho\cdot W_{i-1}^{(l)}}{2} + \beta_i}\right\} \quad \textit{for} \quad l = 0, 1, 2, \ldots \tag{2.4.15}$$

Proof: It is sufficient to show that the function

$$g_3(x) = \frac{1}{\rho}\left[\frac{a_i}{\Delta z}(x - W_{i-1}) - 2\left(\ln\left(-\frac{W_{i+1}-x}{\Delta z}\right) + \beta_i\right)\right],$$

where $a_i = \frac{{x_i}^2}{{x_i}^2+1} - 0.6x_i$ and $\beta_i = {x_i}^2 + 1$, has a unique fixed point in (W_{i+1}, W_{i-1}). The function g_3 is strictly decreasing in this domain $\left(g_3{}'(x) = \frac{a_i(x-W_{i+1})-2\Delta z}{\rho\Delta z(x-W_{i+1})} < 0 \text{ in } (W_{i+1}, W_{i-1}), \text{ as } a_i < 0 \text{ and W is strictly decreasing}\right)$ and $\lim_{x\to W_{i+1}} g_3(x) = +\infty$. Due to these properties of g_3, it can easily be seen that to prove our goal, it is sufficient to show that $g_3(W_{i-1}) \le W_{i-1}$. We have

$$\begin{aligned}
& g_3(W_{i-1}) \le W_{i-1} \\
\Leftrightarrow\ & -\frac{2}{\rho}\left(\ln\left(\frac{W_{i-1}-W_{i+1}}{\Delta z}\right) + \beta_i\right) \le W_{i-1} \\
\Leftrightarrow\ & -\ln\left(\frac{W_{i-1}-W_{i+1}}{\Delta z}\right) - \beta_i \le \frac{\rho\cdot W_{i-1}}{2} \\
\Leftrightarrow\ & \ln\left(\frac{W_{i-1}-W_{i+1}}{\Delta z}\right) + \beta_i \ge -\frac{\rho\cdot W_{i-1}}{2} \\
\Leftrightarrow\ & \ln\left(\frac{W_{i-1}-W_{i+1}}{\Delta z}\right) \ge -\frac{\rho\cdot W_{i-1}}{2} - \beta_i \\
\Leftrightarrow\ & \frac{W_{i-1}-W_{i+1}}{\Delta z} \ge e^{-\frac{\rho\cdot W_{i-1}}{2}-\beta_i} \\
\Leftrightarrow\ & \frac{\Delta z}{W_{i-1}-W_{i+1}} \le e^{\frac{\rho\cdot W_{i-1}}{2}+\beta_i} \\
\Leftrightarrow\ & \Delta z \le (W_{i-1}-W_{i+1})e^{\frac{\rho\cdot W_{i-1}}{2}+\beta_i}.
\end{aligned}$$

The last inequality holds for all $i = 1, \ldots, L-1$ due to (2.4.15), so g_3 has a unique fixed point in (W_{i+1}, W_{i-1}). □

The unique solution of this scheme can be calculated using the Bisection Method.

2.5 Comparison With The Simple Shooting Method

The Simple Shooting Method (see [57]) has been applied to our problem for both cases described above, taking $b = 0.6$. So, for a specific $x_0 \in (0, 2)$, O. D. E. system (2.2.7) is solved for several different values of α_0, where (x_0, α_0) is the initial point. If the solution trajectory reaches near one of the saddle points at a distance less than 2mm, we accept that this is a stable manifold of the corresponding saddle point. Tests showed that this distance occurs when α_0 is approximated up to the 7th decimal digit. The application of this method and, generally, all the codes used in this work, are written in MATLAB.

The values that this method produces (W_1) were compared to the values of the above numerical schemes (W_2). If we denote the points of a discretization of the comparison

domain as $x_i,\ i = 1 \dots N$, then the Absolute Error (AE) ant the Relative Error (RE) at x_i are defined as follows:

$$AE = |W_1(x_i) - W_2(x_i)| \quad \text{and} \quad RE = \frac{AE}{|W_1(x_i)|}, \quad i = 1, \dots, N. \tag{2.5.1}$$

For $\rho = 0.03$ we have one equilibrium point, saddle-stable, which is $(0.3534, 0.1010)$. The initial condition for W is $W(0.3534) = -207.369$. For $\Delta x = \Delta y = 0.03$, the mean and the max RE between the two methods are 0.06% and 0.15%, respectively (see Table 2.1 and Fig. 2.8(a)).

Table 2.1: Results of the comparison between the Simple Shooting Method and the corresponding, depending on the case, numerical scheme. Mean and maximum values over the discretization points for the Absolute Error (AE) and for the Relative Error (RE) are provided.

No. of equilibrium points	Step	Error	[mean,max]
one	$\Delta x = \Delta y = 0.03$	AE	[0.150,0.332]
one	$\Delta x = \Delta y = 0.03$	RE(%)	[0.06,0.15]
three	$\Delta z = 0.01$	AE	[0.081,0.199]
three	$\Delta z = 0.01$	RE(%)	[0.15,0.34]
three	$\Delta z = 0.001$	AE	[0.011,0.069]
three	$\Delta z = 0.001$	RE(%)	[0.02,0.12]

For $\rho = 0.13$ we have three equilibrium points (two saddle points and a vortex). The two saddle points are $(0.4783, 0.1008)$ and $(1.2465, 0.1395)$ and the vortex is $(0.8366, 0.0902)$. The two boundary conditions are $W(0.4783) = -49.4852$ and $W(1.2465) = -64.8708$. The stopping criterion we used when applying the algorithm was $||W - W'||_\infty < 5 \cdot 10^{-4}$, where W' is the result 100 iterations after the result W. For $\Delta z = 0.01$ the algorithm stopped after 1000 iterations. The mean and the max RE between the two methods for this Δz are 0.15% and 0.34%, respectively (see Table 2.1 and Fig. 2.8(b) for this comparison). For $\Delta z = 0.001$, 7100 iterations are required and the results are much better: The above two errors are 0.02% and 0.12%, respectively.

2.6 Conclusion

The theoretical study and the numerical approximation of the welfare function provided by the economic analysis of the Shallow Lake Problem is the main problem of the work of this Chapter. In our approach, the welfare function is proved to be a viscosity solution of an Optimal Hamilton-Jacobi-Bellman equation. This result provides important properties of this function concerning its smoothness and its graphical representation. It also allows for its numerical approximation through convergent monotone schemes. Three different numerical schemes are presented, the "forward", the "backward" and the "upwind" schemes and the decision of which to use depends on the desired domain of the approximation. Fixed point arguments which guarantee the convergence of these schemes are presented.

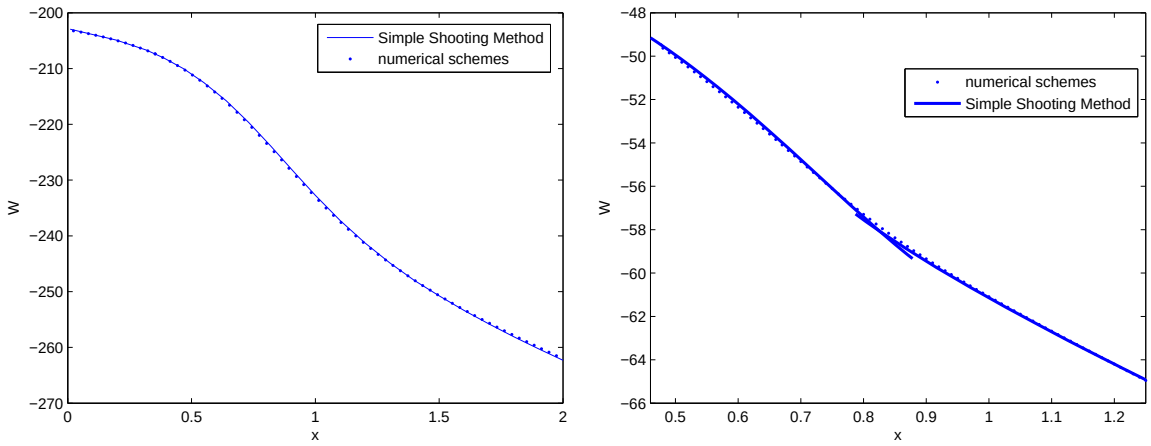

(a) (b)

Figure 2.8: Comparison between the Simple Shooting Method and the result of the numerical schemes. The case of one equilibrium point is depicted in (a) ($b = 0.6, \rho = 0.03, \Delta x = \Delta y = 0.03$) and the case of three equilibrium points is depicted in (b) ($b = 0.6, \rho = 0.13, \Delta z = 0.01$).

The Simple Shooting Method is used as a "gold standard" to test the accuracy of the numerical schemes results. The mean Relative Error calculated was 0.06% in the case of one saddle point ($\Delta x = \Delta y = 0.03$) and 0.02% in the case of two saddle points (in the domain between them and for spatial step $\Delta z = 0.001$). These results can be considered satisfactory and prove the accuracy of the numerical approximations. In addition, all the above results depict the importance of the extraction of the (OHJB) and of the consideration of the welfare function as its viscosity solution.

Chapter 3

Abdominal Aortic Aneurysm 2D Image Segmentation

Abdominal Aortic Aneurysm (AAA) is a localized dilatation of the aortic wall. Accurate measurements of its geometric characteristics are critical for a reliable estimate of AAA rupture risk. However, current imaging modalities do not provide sufficient contrast between thrombus and surrounding tissue thus making the task of segmentation quite challenging. The main objective of the work of this Chapter is to address this problem and accurately extract the thrombus and outer wall boundaries from cross sections of a 3D AAA image data set (CTA). New geometrical methods applying tools like the inversion mapping and the convex hull of a closed curve are used to trace these boundaries exploiting the presence of calcifications and to address the problem of leakage of a moving front into sectors of similar intensity. They are applied to the boundary curve obtained by a Level Set Method (LSM). A Fast Marching Method (FMM) is used initially to resolve the problem of speed that LSM's present. The versatility of the methods is tested by creating artificial images which simulate the real cases. Segmentation quality is quantified by comparing the results with a manual segmentation of the slices of ten patient data sets. Sensitivity to the parameter settings and reproducibility are analyzed. This is the first work to our knowledge that utilises the level set framework to extract both the thrombus and external AAA wall boundaries.

3.1 Introduction

The aorta is the largest artery in the human body and the main blood vessel leading away from the heart. An Abdominal Aortic Aneurysm (AAA) is a permanent and irreversible localized dilatation of the abdominal section of this vessel. In clinical practice, diagnostic information of the 3D anatomy of an AAA is extracted non-invasively in-vivo, through Computed Tomography Angiography (CTA). AAA can grow progressively larger and may eventually rupture if not diagnosed and treated. Accurate estimation of AAA rupture risk remains an open problem. There are numerous indicators which have been suggested, such as wall stress, wall stiffness, intraluminal thrombus thickness and wall

tension. Their existence is due to the fact that the standard procedure according to which there is intervention (open repair or stent) when the maximal diameter is greater than 5.5cm, is not as reliable as it should be. For the study of the above indicators and for a reliable patient specific estimate of AAA rupture risk, accurate geometric characterization of the aneurysm is critical. That is why a construction of a 3D model of the aorta is required.

3D reconstruction of the complex anatomy of an AAA from medical imaging data can be achieved through either a slice-by-slice 2D segmentation of the structures of interest and the subsequent application of a 3D surface reconstruction method [27, 39] on the extracted boundary points, or by utilization of a 3D segmentation approach that extracts the surfaces of interest in one step [58, 40, 17, 55]. A manual 2D segmentation is a rather time-consuming procedure with the additional drawback of large intra- and inter-observer variability. An automatic segmentation method, which is accurate and robust, would alleviate these problems. Level Set Methods (LSM's) [51, 46] have been used in this direction due to their advantages compared to other methods, such as the formulation of the level set without a parametrization, resulting to a free transform and change of its topology, and the relative ease in extending the method to 3D problems. Unfortunately, AAA segmentation is a rather complicated task for this type of methods, due to the low image contrast between thrombus and surrounding tissue that current imaging modalities provide and due to the strong edges that many neighboring structures present. As LSM's are based on the modulus of the intensity gradient, the basic problem that arises is the distinction between the thrombus and the outer wall boundaries. Other drawbacks of these methods are the leakage of the advancing front into regions of similar intensity, not stopping at the outer wall boundary, and the fact that they are computationally expensive and thus slow. These problems explain the fact that LSM's have been used in the past mainly for lumen (the interior of the aorta through which blood flows) segmentation.

Level Set Methods have been employed several times in the past for AAA outer wall segmentation. Subasic *et al.* [58] implemented a 3D LSM. Loncaric *et al.* [38] used a 2D LSM with a narrow band extension and introduced a stopping criterion curve. Magee *et al.* [40] combined the 3D deformable model, which is based on a triangulated mesh, for an initial segmentation, with an efficient level set implementation. Zhuge *et al.* [63] performed segmentation of the outer wall of AAA in five steps: preprocessing, global region analysis, surface initialization, local feature analysis and level set segmentation. Sonka *et al.* [55] applied a novel 4D optimal border detection algorithm for automatic surface segmentation of the aortic lumen.

Many other methods have been used for segmenting an AAA. De Bruijne *et al.* [16] presented an interactive method for aneurysm sac segmentation which relies on the fitting of a shape model to points with high correlation with the reference contour. De Bruijne *et al.* [15] proposed a method based on Active Shape Models (ASMs) [11], for automated delineation of the outer aneurysm boundary in multiple MR sequences. Olabarriaga *et al.* [45] introduced a new method for deformable model-based segmentation of thrombus in AAA based on a 3D discrete deformable model (DM). Bodur *et al.* [6] computed a centerline and presented an automatic segmentation of the aortic border of the orthogonal slices using a novel variation of the isoperimetric algorithm which incorporates circular

constraints. Borghi *et al.* [7] reconstructed patient-specific aneurysm models, combining information from two different sets of MR imaging sequences. A manual segmentation and a semi-automatic approach based on the region growing method were used. De Putter *et al.* [17] created an initial 3D active object from the lumen centerline. This is iteratively deformed via a time-discretized second order Newtonian-evolution equation. Tam *et al.* [60] combined simple cropping and percentage classification to create smooth and accurate boundaries between the metal tynes that support the stent graft and the aorta and between the aneurysm and air.

In all the above works, there is no distinction between thrombus and wall, except from Borghi *et al.* [7], where the wall was assumed to have a constant thickness along the entire aneurysm. To our knowledge, there is only one recent work extracting the wall thickness of the AAA wall using, however, a completely different approach: Martufi *et al.* [41] used intensity histograms for the thrombus segmentation and a neural network for the outer wall segmentation.

In the work of this Chapter, a great part of which can be found in [64] and [32], we utilize the level set framework and geometrical methods for a semi-automatic 2D segmentation of the thrombus and outer wall boundaries from cross sections of a 3D AAA image data set (CTA). The main objective of this work is to accurately distinguish the thrombus and the outer wall boundaries whenever there is adequate information provided by the CTA scans for the arterial wall. This is the case when calcifications, which appear in AAA CTA images as very high intensity regions, are present, or there is sufficient intensity gradient or when information can be extracted from neighboring regions through interpolation. An example of such a slice of an AAA CTA scan is shown in Fig. 3.1, where the two boundaries have been obtained by a manual segmentation. We present two geometrical methods which exploit the presence of calcifications. These methods reconstruct the thrombus and wall boundaries from the toothed-shaped, due to the presence of calcifications or weak intensity gradient change, boundary curve obtained by LSM. Our algorithms have been applied to ten patient data sets (450 slices) and the extracted results have been compared with a manual segmentation obtained from a medical expert.

3.2 Overview Of The Methods

The basic steps of the segmentation framework proposed in this work, which combines the level set framework with geometrical methods, are shown in Fig. 3.2. Initially, a suitable cropping is performed to the selected slice of the AAA CTA scan to extract the region of interest in order to reduce segmentation time. The FMM is first applied with a proper modification. The user is interactively asked to enter up to four pairs of starting and ending points in order to obtain an optimized initialization used for the thrombus and the outer wall segmentations. For the thrombus boundary segmentation, the LSM is applied to the thrombus initialization to obtain a boundary curve to which the thrombus boundary reconstruction method is then applied.

In the outer wall boundary reconstruction, the leakage issues of the advancing front are resolved by using the LSM to the thrombus initialization accompanied by one or more, if required, of the three stopping criteria introduced in this work. These are the

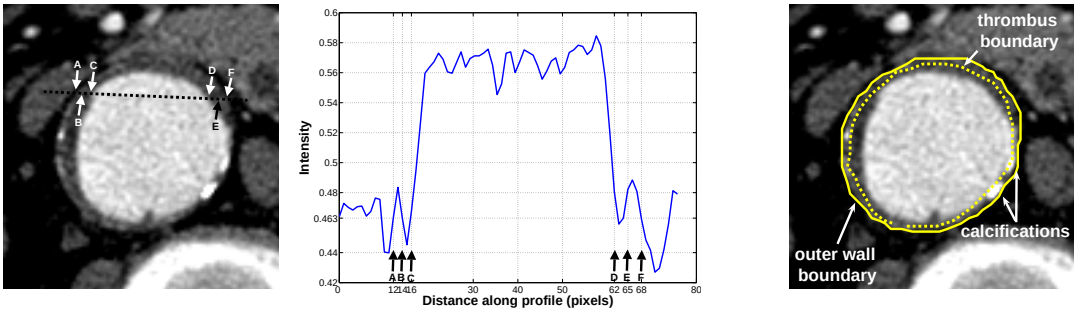

(a) (b) (c)

Figure 3.1: Example of a slice of an AAA CTA scan in (a). The window width is properly adjusted, so that the AAA wall is visible. (b) presents the intensity profile along the dashed line of (a). This shows that there is intensity difference inside the wall (regions A-B and E-F). The possible existence of such information and, mainly, the existence of calcifications, are exploited in our segmentation methods. This is one of the slices used in our experiments and the manual segmentation of the two boundaries provided by an expert is depicted in (c).

Sector Criterion (SC), the Length Difference Rate Criterion (LDRC) and the Internal-External Contact Criterion (IECC). The leakage region of a slice can be also detected if it is desired by the user, using the Detection of Leakage Region (DLR) method. The outer wall boundary reconstruction method is then applied to the stopped boundary curve. As part of the method, the user is interactively asked to apply an appropriate thresholding to the image in order to locate the existing calcifications. In case the resulting thrombus and outer wall boundaries coincide in some regions, due to lack of calcifications and low intensity gradient, the Thrombus and Wall Boundaries Distance (TWBD) method is performed to the thrombus boundary to set a proper distance by an interpolation technique.

3.3 Level Set Framework

3.3.1 First Phase Of The Model-Fast Marching Method (FMM)

3.3.1.1 The Fast Marching Method Equation

The application of the level set framework consists of two phases. In the first phase we use the FMM. In this method, the position of the expanding front is characterized by computing the arrival time $T(x, y)$ of the front as it crosses each point (x, y) [51]. If Γ is the initial location of the interface then $T = 0$ on Γ. At time t the moving front is given by

$$\Gamma(t) = \left\{(x, y) \in \mathbb{R}^2 | T(x, y) = t\right\} \quad . \tag{3.3.1}$$

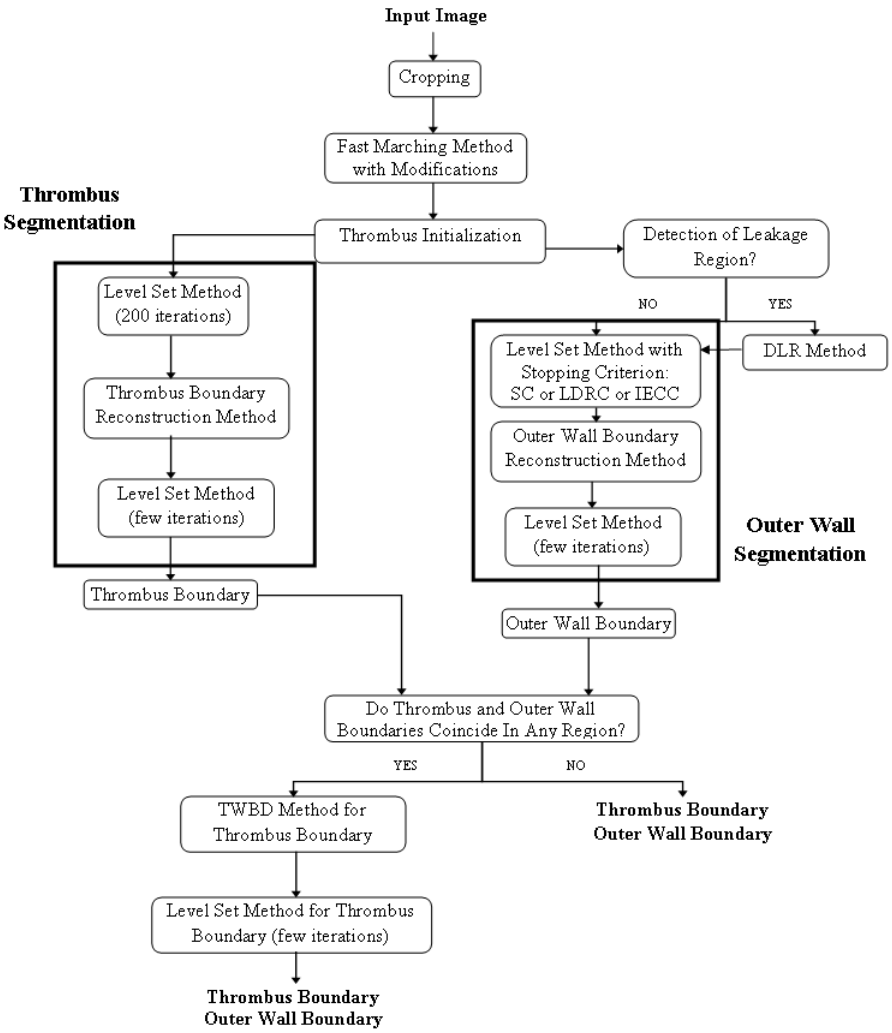

Figure 3.2: Diagram of the segmentation methods.

The front is moving with a speed function in the normal direction $g_I > 0$, so the equation for the arrival function $T(x, y)$ is

$$g_I|\nabla T| = 1 \ . \tag{3.3.2}$$

Here, the proposed edge-indicator function, which restrains the evolving front from leaking out of the desired region is

$$g_I(x, y) = \frac{1}{1 + \lambda|\nabla G_s * I(x, y)|^2} \ . \tag{3.3.3}$$

I is the image intensity and for $\alpha \in \mathbb{R}^2$, $G_s(\alpha)$ is the Gaussian with width s,

$$G_s(\alpha) = \frac{1}{4\pi s} e^{-\frac{|\alpha|^2}{4s}} \ , \tag{3.3.4}$$

which is used to reduce possible noise effects in the image. λ is a positive parameter. g_I is close to unity away from the boundaries and drops to zero near sharp changes in the image gradient. These changes presumably correspond to the edges of the desired shape.

3.3.1.2 Numerical Schemes For The FMM

For the numerical solution of the Eikonal equation

$$F|\nabla T| = 1, \tag{3.3.5}$$

which is the general form of (3.3.2), where $F > 0$ is the speed in the normal outward direction of the curve/surface, the following upwind scheme (written for the 3D case) turns out to be very convenient (see [51])

$$\left[\begin{array}{rl} & \max(D^{-x}_{ijk}T, -D^{+x}_{ijk}T, 0)^2 \\ + & \max(D^{-y}_{ijk}T, -D^{+y}_{ijk}T, 0)^2 \\ + & \max(D^{-z}_{ijk}T, -D^{+z}_{ijk}T, 0)^2 \end{array} \right]^{1/2} = \frac{1}{F_{ijk}}. \tag{3.3.6}$$

The reason for using this scheme deals with the basic idea of the FMM, according to which solution T is systematically built using upwind values (opposed to the direction of information flow) only. This scheme allows for outward flow of information, from smaller to larger values of T. So, the FMM rests on building the solution outward from the smallest T value, stepping away from the boundary condition in a downwind direction.

An explanation of (3.3.6) (this equation shows that for the calculation of T_{ijk} we choose its smallest neighbors (if they exist) in each of the three directions) can be given with the help of optimal control theory. Equation $|\nabla T| = \frac{1}{F}$ is equivalent to

$$\sup_{|q|\leq 1} \left\{ \nabla T(x) \cdot q - \frac{1}{F(x)} \right\} = 0 \quad \forall x \in \Omega, \tag{3.3.7}$$

where $\Omega \subseteq \mathbb{R}^3$. T is the value function of the following optimal control problem :

$$\left\{ \begin{array}{ll} y'_x(s) = -q(s), & s \geq 0 \\ y_x(0) = x \end{array} \right. \tag{3.3.8}$$

where

$$q \in A_{adm} = \left\{ q : \mathbb{R}_+ \to \mathbb{R}^2 \quad \text{measurable/ } |q(s)| \leq 1 \right\}.$$

The functional cost is

$$J(x, q(\cdot)) = \int_0^T \frac{1}{F(y_x(s))} ds + \phi(y_x(T)),$$

where $T = \min\{t \geq 0 | y_x(t) \in \partial\Omega\}$. So, the value function of this problem is

$$T(x) = \inf_{q(\cdot) \in A_{adm}} J(x, q(\cdot))$$

and, following optimal control theory, (see [5]), it satisfies the corresponding HJB equation as a viscosity solution, namely (3.3.7). Using (3.3.7) it is obvious that $q = \frac{\nabla T}{|\nabla T|}$, so, the optimal trajectory of the problem (the one which is connected with the optimal control) can be calculated from

$$\begin{cases} y_x'(s) = -\frac{\nabla T}{|\nabla T|}, \\ y_x(0) = x \end{cases} .$$

So, starting from point x, we have to move in the direction of the largest reduction of T (which is $-\frac{\nabla T}{|\nabla T|}$), namely to the neighbor of T_{ijk} with the smallest value.

A convenient algorithm for the solution of the 3D upwind numerical scheme (3.3.6) can be found in the second Chapter of [20] and is based on the fact that this equation is a quadratic equation for T_{ijk}, assuming that the neighboring grid values for T are given. Thus, one solution for (3.3.5) comes from updating the value of T at each grid point according to this quadratic, for some number of steps/iterations:

For iter=1,n
  For $i, j, k = 1, \dim$
    Solve Quadratic for $T_{ijk}^{\text{iter}+1}$, given
      $T_{i-1,j,k}^{\text{iter}}, T_{i+1,j,k}^{\text{iter}}, T_{i,j-1,k}^{\text{iter}}, T_{i,j+1,k}^{\text{iter}}, T_{i,j,k-1}^{\text{iter}}, T_{i,j,k+1}^{\text{iter}}$
  EndFor
EndFor.

Assuming N points in each direction and an optimistic guess of roughly N steps to converge, the computational cost of the above is of order $O(N^4)$. The above numerical scheme is monotone, stable, consistent and admits a Maximum Principle, so it converges (see [48]). In addition, there exists a fast and explicit algorithm (also found in [48]) which makes it converge in very few iterations.

A non-iterative procedure can be used for the calculation of values of T at the grid points, using the central idea of the FMM. This is extensively described in [51],[20] and we here describe its basic steps. Solution T is systematically constructed using the smaller values only. We sweep the front along by considering points in a thin zone around the existing front, and marching this thin zone forward, freezing the values of existing points and bringing new ones into the narrow band structure. The key is in the selection of which grid point in the narrow band to update.

We consider a two-dimensional version of the Eikonal equation $F|\nabla T| = 1$ and we analyze the procedure with the help of Fig. 3.3, taken from [51]. The boundary value is known at the origin (black sphere in the first image of Fig. 3.3). The black spheres in Fig. 3.3 (called *Known*) are the grid points at which their value has been found and will not be changed. The dark gray spheres (called *Trial*) are the next grid points to be examined and for which an estimate of T has been computed using equation (3.3.6). Finally, the light gray spheres (called *Far*) is the set of all other grid points for which there is not yet an estimation for T. The steps of the loop are the following:

(i) Put the boundary value to the black sphere (*Known*) and value ∞ to all the other spheres (*Far*).

(ii) Tag as *Trial* the four neighbors of the black sphere and compute their values by solving the quadratic equation (3.3.6). If there are two solutions, keep the larger one (due to the central idea of the FMM as mentioned before).

(iii) Freeze (add to *Known*) the *Trial* point with the smallest T value (A in Fig. 3.3).

(iv) Tag as *Trial* all neighbors of A that are not *Known* and compute their values by solving the quadratic equation (3.3.6).

(v) Add the smallest among all *Trials* to *Known*.

(vi) Return to step (ii).

Due to the fact that the recomputation of the values of T at the neighboring points cannot provide a smaller than any of the *Known* points value, we need never go back and "revisit" a point with a known value. A narrow band LSM (see [51]) can be used to find the initial values for the method. Some other additional characteristics of this procedure concern an efficient scheme with the use of a binary tree for a fast detection of the grid point in the narrow band with the smallest value T among all the *Trials*, the reduction of the overall computational cost from $O(N^4)$ to $O(N^3 \log N)$, the fact that no CFL condition is required for the time step Δt and, finally, the possibility of increasing the order of accuracy (from one to two) by using an appropriate scheme. For a detailed presentation of all these characteristics, see [51].

3.3.2 Second Phase Of The Model-Level Set Method (LSM)

3.3.2.1 The Level Set Method Equation

In the second phase we embed the initial position of the front as the zero level set of a higher-dimensional function ϕ and we link the evolution of this function to the propagation of the front itself through a time-dependent initial value problem. At any time, the front is given by the zero level set of the time-dependent level set function ϕ. So, at time $t \geq 0$, the front is

$$\Gamma(t) = \left\{(x, y) \in \mathbb{R}^2 | \phi(x, y, t) = 0\right\} \quad , \tag{3.3.9}$$

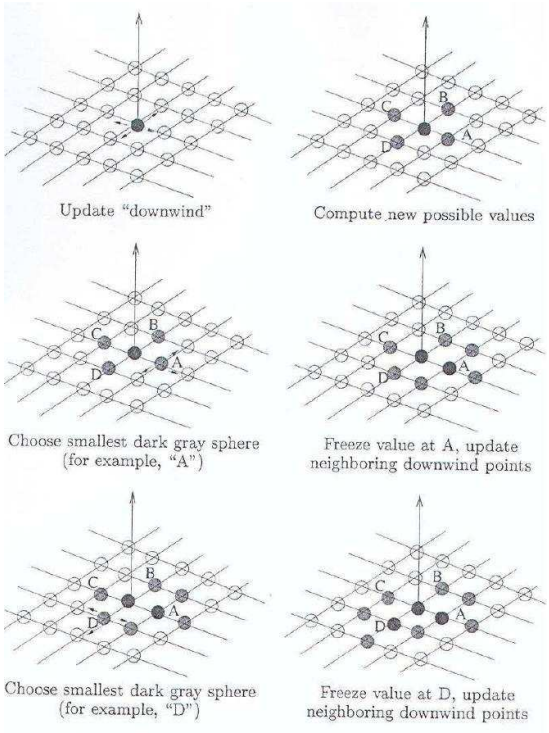

Figure 3.3: Update procedure for Fast Marching Method

where $\phi(x, y, 0)$ is the result of the FMM. The level set equation used in this phase is

$$\phi_t = g_I(x, y)(\kappa - c)|\nabla\phi| + \nabla\phi \cdot \nabla P \ . \tag{3.3.10}$$

g_I is the same as before, κ is twice the mean curvature, $c > 0$ a parameter used for faster convergence [51] and

$$P(x, y) = -|\nabla G_s * I(x, y)| \ . \tag{3.3.11}$$

This level set equation consists of three terms: $g_I\kappa|\nabla\phi|$ which acts as a smoothing term for the front away from the boundary under detection, $g_I(-c)|\nabla\phi|$ which is a driving expansion force and $\nabla\phi \cdot \nabla P$ which has a stabilizing effect, as P constantly attracts the front to the edges in the image [51, 46, 49]. Sapiro [49] and Antiga [4] derive analytically an equation similar to (3.3.10). The only differences between this and the object-detection model adopted by Sapiro [49] are parameter λ in (3.3.3) and the use of opposite signs for c. For a detailed proof of (3.3.10) for the 3D case, based on [4], see the Appendix B. Two other variational formulations of the LSM can be found in C. Li *et al.* [34] and Gelas *et al.* [26].

If we look at equation (3.3.10) from a strict mathematical view, with an initial condition $\phi = g$ in $\mathbb{R}^2 \times \{t = 0\}$, where $g(x)$ is a continuous function in $\mathbb{R}^2$, we can say that existence

and uniqueness of a viscosity solution ϕ can be proved under certain conditions (see [51]). Function ϕ found in the definition of $\Gamma(t)$ is exactly this viscosity solution and $\Gamma(t)$ is the generalized evolution of $\Gamma(0)$, which is the initial front. It can be proved that $\Gamma(0)$ is independent of the initial choice of the continuous function $g(x)$ that describes it (see [23]). For more about the relation between level set equations and viscosity solutions and for the numerical schemes used for convergence to the correct viscosity solution, see [51].

3.3.2.2 Numerical Schemes For The LSM

The scheme used for the numerical solution of equation (3.3.10) combines the forward Euler time discretization with high-order upwind differencing for the hyperbolic $\nabla\phi \cdot \nabla P$ term, Godunov's scheme for the hyperbolic $g_I(-c)|\nabla\phi|$ term and central differencing for the parabolic $g_I\kappa|\nabla\phi|$ term (see [46]). This scheme is consistent and stable using a combined CFL condition, which can be found in [46]. A more accurate approximation of the spatial derivatives can be made with the use of divided differences of high order and this provides first, second and third order schemes (called ENO) or a fifth order scheme (WENO). In addition, due to the existence of a motion in the normal direction ($g_I(-c)|\nabla\phi|$) and an externally generated velocity field ($\nabla\phi \cdot \nabla P$) in (3.3.10), it may be difficult to find the upwind direction. Godunov and Lax-Friedrichs are the most commonly used schemes for determining the correct direction. For more details about these remarks and about the numerical solution of (3.3.10), see [46].

3.3.2.3 Detection Of Leakage Region Method (DLR Method)

The main problem of the LSM in segmenting the outer aortic boundary is the leakage of the moving front (which is the thrombus initialization) into surrounding tissue in regions with similar image intensity to that of the aortic wall (see the yellow curve in Fig. 3.4(d)). Before addressing this issue, we describe a method which can optionally be used to detect the regions where the leakage takes place (see Fig. 3.4(a)). The method is called Detection of Leakage Region (DLR) method. We first split the interior of the thrombus initialization curve into sectors, using radials starting from its center of mass, which are equally spaced by a user-defined sector angle ϕ. The initialization is evolving with the level set equation and a reinitialization as a signed distance function takes place every ten iterations. A calculation of the area of each sector is also made every ten iterations. We then calculate the relative change of its area by comparing it with the sector area at the end of the previous ten iterations. The evolution is interrupted when a local minimum of the relative area change has appeared for all the sectors. When the curve stops, we select the sectors for which the relative area change is of order r for all iterations, to be the ones that give the leakage region in the image. For the choice of the value of r, see Sec. 3.5.1.

The use of the area change as a leakage detection has been previously used [62]. However, herein we adopt a local approach, which allows the detection of even small, localized leakages and also the precise identification of the regions where the leakage occurs.

3.3.2.4 Three Stopping Criteria

The DLR method as described in Sec. 3.3.2.3 provides a stopping criterion which we will call Sector Criterion (SC) (see Fig. 3.4(b)). The second stopping criterion, called Length Difference Rate Criterion (LDRC), stops the curve when the first minimum of the absolute value of the length difference rate of the curve appears. Here, as length difference rate we consider the difference of the total length of the curve every ten iterations. A sudden increase of this rate is due to the leakage, so the curve has to stop (see Figs. 3.4(c,d)).

In the third stopping criterion, called Internal-External Contact Criterion (IECC), we consider an inner and an outer (to the aortic wall) initialization which move towards each other simultaneously; this is achieved by applying the level set equation (3.3.10), with parameter c positive in the case of the inner initialization and negative in the case of the outer initialization (with the same absolute value). The evolution is interrupted as soon as the two evolving curves come into contact. As an inner initialization we take the result of the FMM. As an outer initialization we consider the smallest circle containing the inner initialization, extended by a proper number of pixels p. For the value of p see Sec. 3.5.1. The final result is the inner curve at the time of contact of the two curves (see Figs. 3.4(e,f)).

A comparison of these three stopping criteria, in terms of the speed of their response to a leakage, is presented in Sec. 3.5.6. The resulting curve is then used for the reconstruction of the outer wall boundary (Sec. 3.4.2).

3.4 Geometrical Methods For The Reconstruction Of Thrombus And Outer Wall Boundaries

3.4.1 Thrombus Boundary Reconstruction In The Presence Of Calcifications

The presence of calcified deposits which are located within the AAA wall and the reduced contrast between thrombus and outer wall result in a "toothed" thrombus boundary, as the evolving curve enters the regions between the calcifications (see Fig. 3.5, that describes the method). To eliminate these regions, we consider the inversion mapping with respect to the curve Γ obtained by the LSM. The inversion mapping is the usual transformation $T(z) = 1/(z - z_0)$ in the complex plane, where $z_0 = (x_0, y_0)$ is the center of mass of the domain bounded by Γ. We consider the domain bounded by $T(\Gamma)$ in the image plane under T, and we find the points of its convex hull. To obtain the thrombus boundary we take the image under T^{-1} of the boundary of the constructed convex hull and we apply the LSM for a few iterations. For the matlab code written to apply this method, see the Appendix D.2.

By using the inversion mapping, the possible existence of leakage does not affect the reconstruction of thrombus. So, the final result is not sensitive to the initialization of the method. Note that the stopping criteria are not used (they are used, however, for the reconstruction of the outer wall boundary, as we will explain in the following section).

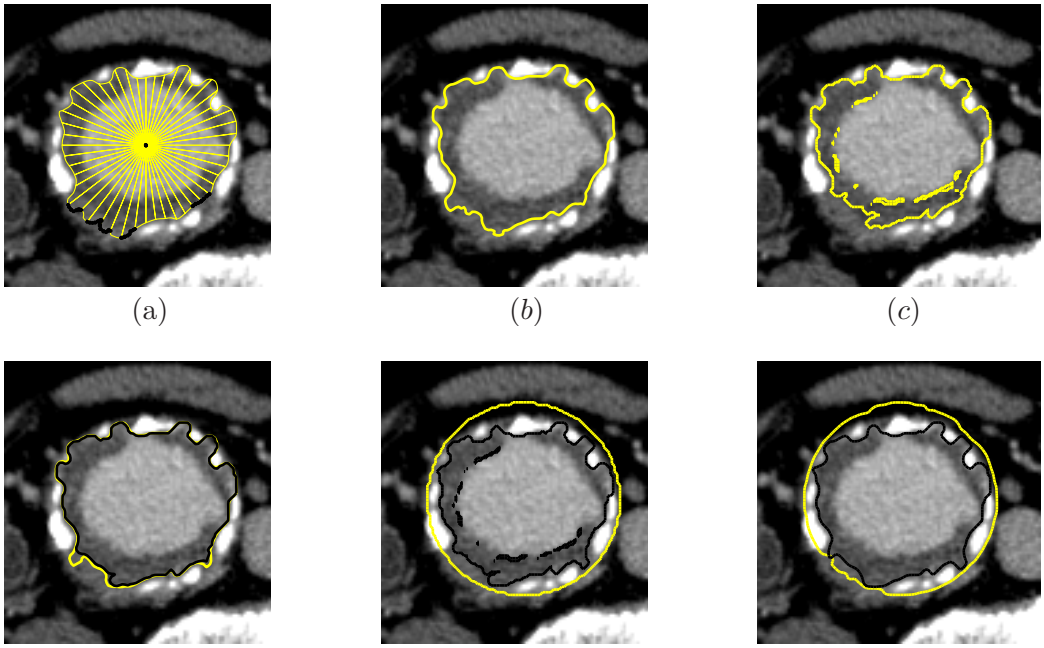

(a) (b) (c)

(d) (e) (f)

Figure 3.4: Results of the DLR method and the three stopping criteria for the same cross section: (a) The leakage regions detected by the DLR method are shown in black ($r = 10^{-2}$). The angle of the sectors is $\frac{\pi}{24}$. (b) The result of SC which stops the curve after 80 iterations. (c) The initial curve used for LDRC obtained by the FMM. (d) The black curve is the result of LDRC (40 iterations) and the yellow curve the result after 100 iterations, showing the leakage if LDRC had not been used. (e) The outer and the inner initialization used for IECC. (f) The final outer and inner curves, where the latter is the IECC result (60 iterations).

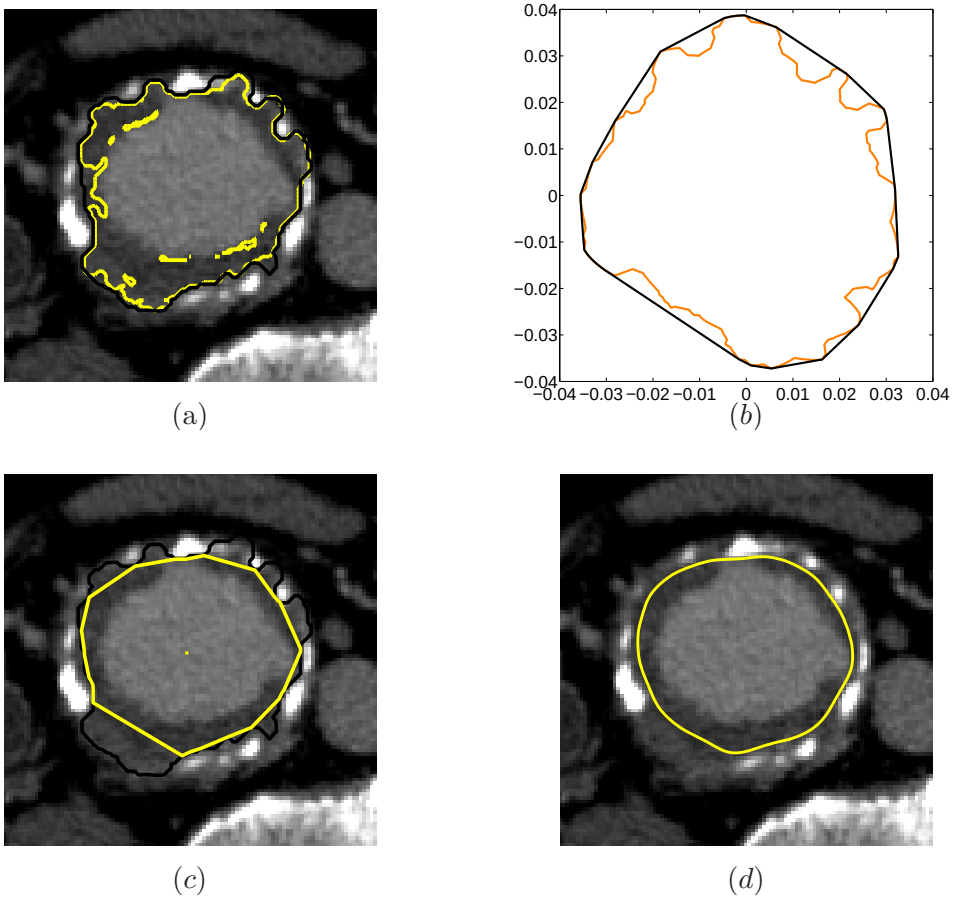

Figure 3.5: The steps for the reconstruction of the thrombus boundary of the cross section of Fig. 3.4: (a) The yellow curve is the thrombus initialization obtained by the FMM and the black curve the result of the LSM (200 iterations). (b) The image of the black curve under the inversion mapping with respect to its centroid (in orange) and the boundary of its convex hull (in black) are depicted. (c) The preimages of the points of the convex hull under the inversion mapping form a domain, whose boundary is the yellow curve. (d) The yellow curve is the final result, after applying the level set equation for 20 iterations.

3.4.2 Reconstruction Of The Outer Wall Boundary In The Presence Of Calcifications

The circumferential distribution of calcifications in the AAA wall can be exploited to segment both the outer wall and thrombus boundaries. The first step in the procedure for the reconstruction of the outer wall boundary is a thresholding of the image to extract the calcification regions (Fig. 3.6(a)). The total area of the pixels above the threshold is computed and displayed and the user selects an upper and lower bound for the threshold. Then an iterative process seeks within this range the threshold value that minimizes the derivative of calcification area with respect to threshold value. If the result is satisfactory (i.e. the SNR of the final thresholded image is high, where calcifications are the signal and all the other parts constitute noise, and also judging from the grayscale image) it is accepted by the user. Otherwise a new threshold range is specified and the process is repeated until a satisfactory result is obtained.

Following the application of a stopping criterion to the evolution of the thrombus initialization with the LSM, we consider the extracted curve and the smallest circle containing this curve. At least one point of each calcification will be interior to this circle (see Fig. 3.6(b)). We then apply the region growing method with each calcification pixel interior to the circle acting as a seed and we use the threshold extracted in the previous step as a rule of similarity to locate all the calcification pixels in the image (Fig. 3.6(c)). We then compute the convex hull of the union of all mid-edge points of the calcification pixels and the points of the curve which was the result of the LSM on the thrombus initialization curve. The boundary of the convex hull (the dashed black curve in Fig. 3.6(d)) will certainly contain all the calcifications. The procedure is concluded by applying the level set equation to this boundary, but taking an inward motion this time, aiming at a smoother result which is more biologically plausible (yellow curve in Fig. 3.6(d)). Figure 3.6(e) depicts both the thrombus and outer wall boundaries extracted by the methods presented in this and the previous section which exploit the presence of calcified deposits.

3.4.3 Case Of Few (Or No) Calcifications-Thrombus And Wall Boundaries Distance (TWBD) Method

In the case where there exist only few or no calcifications inside the AAA wall, regions might appear in the image, where the reconstructed thrombus and outer wall boundaries obtained using the methods of Sec. 3.4.1 and 3.4.2 almost coincide. In some regions, though, even when calcified deposits are absent, the two reconstructed boundaries may not coincide due to the use of the LSM, if sufficient intensity contrast between thrombus and outer wall exists. In general, regions where the two boundaries almost coincide are rare in a cross section with significant presence of calcifications. Moreover, such regions cover approximately 40% of the outer wall contour in the case of the cross sections with almost no calcifications taken from the patient data sets studied in Sec. 3.5. Assuming that wall thickness distribution should present a smooth continuity, interpolation can be applied to extract wall thickness in regions where thrombus and outer wall boundaries are too close to each other.

We consider many rays starting from the centroid of the thrombus, so that two suc-

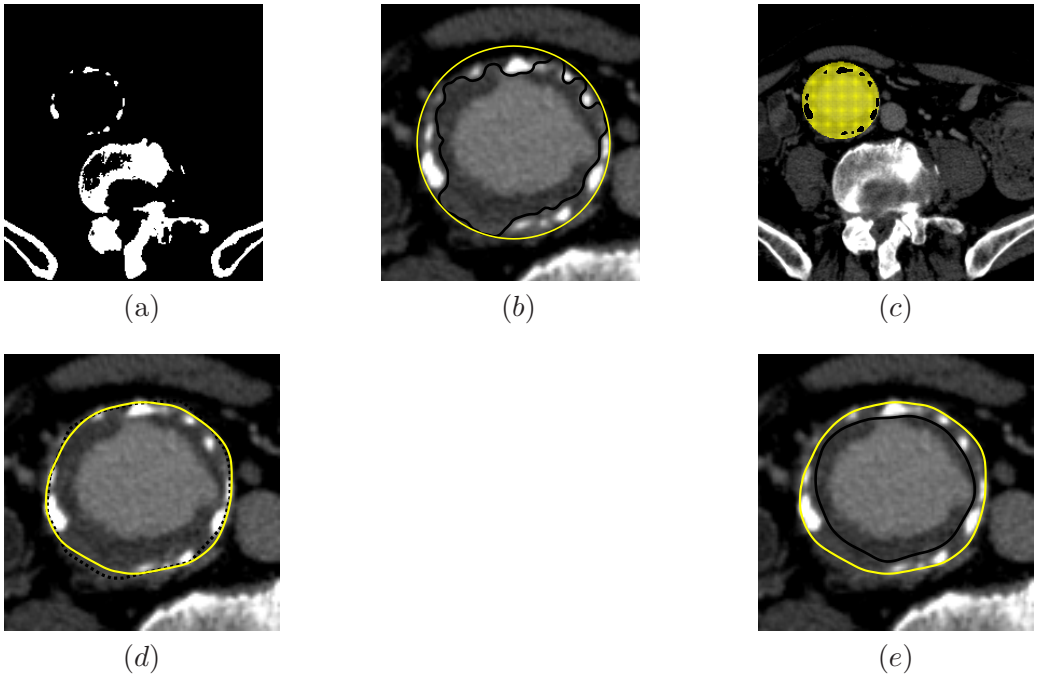

Figure 3.6: (a)-(d) The steps for the reconstruction of the outer wall boundary in the cross section of Fig. 3.4: (a) Appropriate thresholding to locate the calcifications. (b) The LSM extracted curve in black (using LDRC, 40 iterations) and the smallest circle containing this curve are depicted. (c) Detection of the calcification pixels (shown in black) using this circle. (d) The dashed curve is the boundary of the convex hull of the union of the mid-edge points of these pixels and of the black curve depicted in (b). The yellow curve is the final result, after applying the level set equation to this boundary for 20 iterations. (e) depicts the result of the methods (thrombus and outer wall boundaries in black and yellow, respectively) for the same cross section.

cessive rays form the same angle ϕ, and find the distance (wall thickness) between the two intersection points of each ray with the thrombus and outer wall curves. We find the thrombus points which are connected with distances of order $d/10$ mm. For the value of the parameter d, see Sec. 3.5.1. For each point, we find the nearest n thrombus points in the counterclockwise direction whose distances (wall thicknesses) are of order d mm and calculate the mean of these distances. Then, we find which of these n points has distance closer to this mean. We denote this distance as d_l and the distance found following the same procedure in the clockwise direction as d_r. Then a linear interpolation between d_l and d_r is made to obtain a new wall thickness (and a new thrombus point) for each point in the region with distances of order $d/10$ mm. Finally, we apply the level set equation to the so reconstructed thrombus boundary for a small number of iterations (e.g. 10) taking an outward motion, to obtain a smoother and physiologically more realistic result.

Numerical tests have shown that for $n \in \{4, 5, \ldots, 10\}$ the results are very similar, because of the very small angle ϕ. Figure 3.7 shows the result of the method for two cross sections, one with few calcifications, approximately 30% of the boundary parameter (Fig. 3.7(a)) and one with almost no calcifications, approximately 8% of the boundary parameter (Fig. 3.7(d)).

3.5 Experiments

3.5.1 Implementation Of The FMM And LSM

We applied the FMM using the MATLAB-based "Fast Marching Toolbox" [47] created by Gabriel Peyré to obtain a thrombus initialization for the LSM. We took $\lambda = 50$ for g_I and we used a 5×5 Gaussian filter with $s = 1$. In this Toolbox, the user typically gives a pair of points, a start and an end point (a point, here and in the rest of this Chapter, is the center of a pixel). The front is initialized with the start point inside the desired region and expands until the solution has almost reached the desired edge. It stops expanding when it meets the end point for the first time. These points are specified either by their coordinates or interactively by cursor positioning on the image.

It should be noted that a good initialization is important for a satisfactory final result. So, the initial curve: a) must be close to the contour we want to detect, b) must not have leaked out of it, and c) should not have been captured by the lumen in some region. In order to obtain an initialization with the above principles, some general rules are provided for the selection of the start and end points: the start point is chosen either near a conceivable center of mass of the thrombus or next to a region of high contrast, but end point should be chosen at a low contrast region, in order to avoid the leakage.

Unfortunately some images are rather difficult to segment and extract a proper thrombus initialization (due to many leakage problems or strong responses from neighboring objects, such as the spine, lumen and calcifications). To solve this problem we modified the aforementioned Toolbox to allow the user to select up to four pairs of points (this is the minimum number of pairs required to produce a good initial curve for the most difficult to segment cases and it was determined after extensive experimental work). In this case the initialization is the union of the results extracted for each pair. Another issue, which

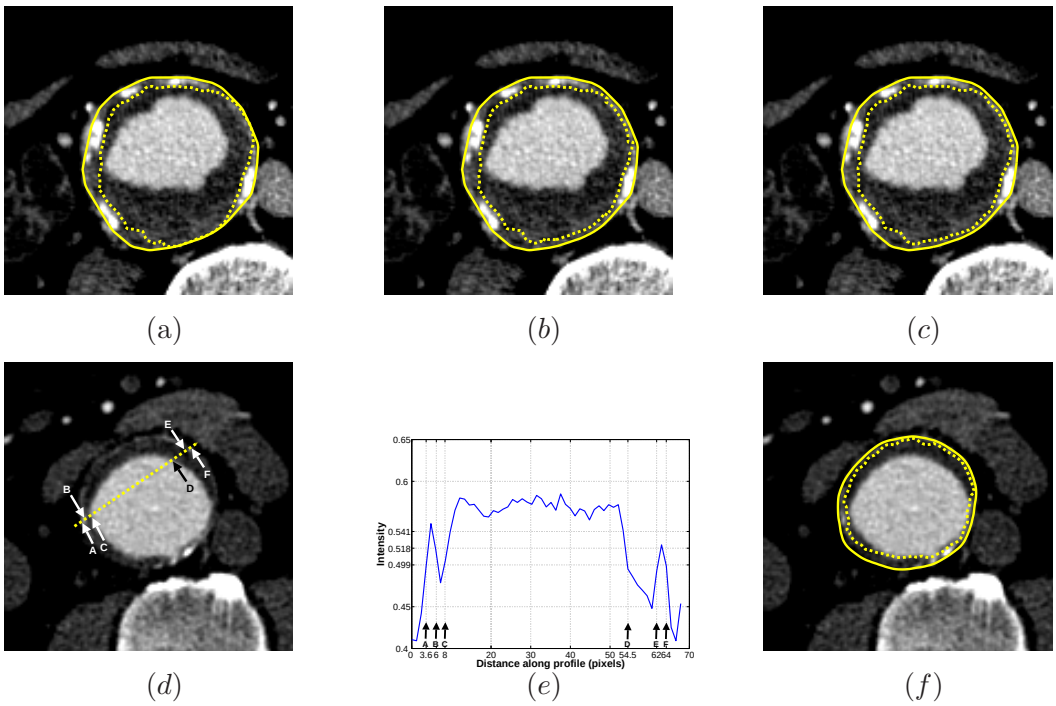

Figure 3.7: Application of the TWBD method for two cross sections with few (a) and no (d) calcifications ($d = 1$ mm, $n = 4$ and $\phi = \frac{\pi}{200}$). Thrombus and outer wall boundaries coincide in some regions in (a), due to the lack of calcifications. The result of the TWBD method is shown in (b) and the final result, after applying the LSM, in (c). A proper distance between the two boundaries has been settled. A cross section with very few calcifications is depicted in (d). (e) presents the intensity profile along the dashed line of (d). This shows that there is intensity difference inside the wall (regions A-B and E-F) compared to thrombus (regions B-C and D-E). The two boundaries may coincide in some regions but the existence of regions with distance between the boundaries due to this difference is exploited via the TWBD method. The final thrombus boundary (dashed line), after applying the TWBD method and the LSM, and the outer wall boundary (continuous line) are shown in (f).

is the only limitation of the method, is that the two selected points of each pair should belong to pixels of almost the same intensity and a path of pixels with similar intensity connecting these two points should also exist. This is a drawback of the method as far as reproducibility of the thrombus initialization is concerned, due to the wide range of intensities that may exist near the thrombus boundary or inside the thrombus. Another modification is introduced to fix this matter: Following the selection of the starting point, thresholding is applied so that all the pixels with intensity very close to the intensity of this point are shown in white and the rest of the pixels are shown in black. In this way, the possible ending points that the user can select from are presented and the existing paths joining some of these points with the starting point are also shown. For the 2D version of the Toolbox the code is in C++ which makes the application of the method very fast.

For the implementation of the LSM we used the MATLAB-based "Level Set Toolbox" [59] created by Baris Sumengen. In this Toolbox there are two basic routines. The first one is for the reinitialization of the level set function ϕ as a signed distance function (usually every five or ten iterations) so that ϕ remains smooth as it evolves. The choice of a signed distance function for this purpose is not accidental: these functions are the best candidates for implicit curve/surface representations because of their smoothness (they are smooth everywhere except from equidistant to the curve points, which are located far away from the zero level set), simplicity (they satisfy equation $|\nabla\phi| = 1$, which simplifies the other equations) and stability. The frequent reinitialization takes place due to the fact that ϕ may present steep gradients, which should be avoided to obtain high order approximations of the spatial derivatives and high quality numerical results. The numerical techniques, then, need to be efficient only for the zero level set, as the difficulties away from it can be ignored due to the periodic correction of the rest of the points of ϕ, which happens because of the reinitialization. The reinitialization technique used in this Toolbox is connected with the following reinitialization equation

$$\phi_t + S(\phi_0)(|\nabla\phi| - 1) = 0,$$

where $S(\phi_0)$ is equal to 1 outside the curve, -1 inside the curve and 0 at the points of the curve, where we want ϕ to stay equal to zero. Numerical tests showed that the results get better if $S(\phi_0)$ is numerically smoothed, so the expression

$$S(\phi_0) = \frac{\phi_0}{\sqrt{{\phi_0}^2 + (\Delta x)^2}} \tag{3.5.1}$$

can be used for its calculation, as a numerical approximation. For more about this technique, see Chapter 7 of [46].

The second routine of the Toolbox is for the evolution of the curve where all three types of motion are applied (motion in the normal direction, motion involving mean curvature and motion in an externally generated velocity field). We took $\lambda = 0.1$, $c = 5000$ and a 5×5 Gaussian filter with $s = 1$. Moreover, we took $r = 10^{-2}$ as the order of the relative area change in the DLR method, $p = 1.5$ pixels in the IECC and $d = 1mm$ as the order used in the TWBD method. For an explanation of the values of all the parameters used and for a sensitivity analysis, see Sec. 3.6.

Remark 3.5.1. Instead of using a 2D (5×5) Gaussian filter, a 1D filter, in a dimension-by-dimension fashion, can also be used: A comparison between the two filters showed that the resulting images obtained are exactly the same. This means that the second technique can be used instead, saving time and computational cost. The profit is bigger if a 3D (or higher dimension) filter is replaced in this way: A comparison between a $5 \times 5 \times 5$ Gaussian filter and a 1D (dimension 5) filter which scans the whole 3D image three times (taking each time the filter parallel to each of the three axis) provided a 100% similarity of the resulting images, even for large values of s. The computational cost is significantly reduced in this way (for an image with N^3 pixels, order $O(N^3)$ is changed to $O(N^2)$).

To perform the thrombus boundary segmentation, the LSM is applied to the thrombus initialization for 200 iterations before the boundary is reconstructed with the method described in Sec. 3.4.1. The above number of iterations has been obtained after experimentation with various values and it is parameter-independent. In contrast to that, the number of iterations of the LSM (applied again to the thrombus initialization) for the outer wall segmentation is determined by a stopping criterion.

3.5.2 Results For Artificial Images

We created some artificial images (Fig. 3.8) to test the versatility of our methods and the two major problems that CTA images of an AAA present: difficulty in distinguishing the thrombus and the outer wall and leakage outside the outer wall. Figure 3.8(a) shows five areas of different intensity, with constant intensity in each of them. The contrast ratio is 1138:1 and, assuming that the intensity value for black (background) is 0, "lumen", "thrombus", "outer wall" and the four "calcifications" have constant intensity values of 209, 116, 162 and 1137, respectively. There is also a region in which "thrombus" and "outer wall" have similar intensity (right side). Noise was not added to the image since noise was quite low in the data sets of our experiments and the Gaussian filter used properly diminishes its effects.

Figure 3.8(d) shows a different test image, where we have taken the (extreme) case of exactly the same intensity for "thrombus" and "outer wall". There are also two outer leakage regions and eight "calcifications". Contrast ratio and intensity values are the same as in Fig. 3.8(a). The intensity value inside "thrombus", "outer wall" and leakage regions is 116. No noise was added to this image, as well. In Fig. 3.8(f) the maximum error in the two leakage regions is about six pixels, while the borders of these regions are placed 15 pixels outside the "outer wall". In these artificial images the pixel size is approximately equal to 0.265mm, so this maximum error is about 1.59mm. This shows the effectiveness of LDRC. In addition, due to the presence of the eight "calcifications" a satisfactory result is extracted, although there is no intensity difference between the two areas.

3.5.3 Manual And Semi-Automatic Segmentation

A quantitative validation of our algorithm was performed using ten CTA scans acquired from ten different patients at the University Hospital of Heraklion. All the slices consist of 512×512 pixels and the pixel size varies in these data sets from 0.639mm to 0.898mm.

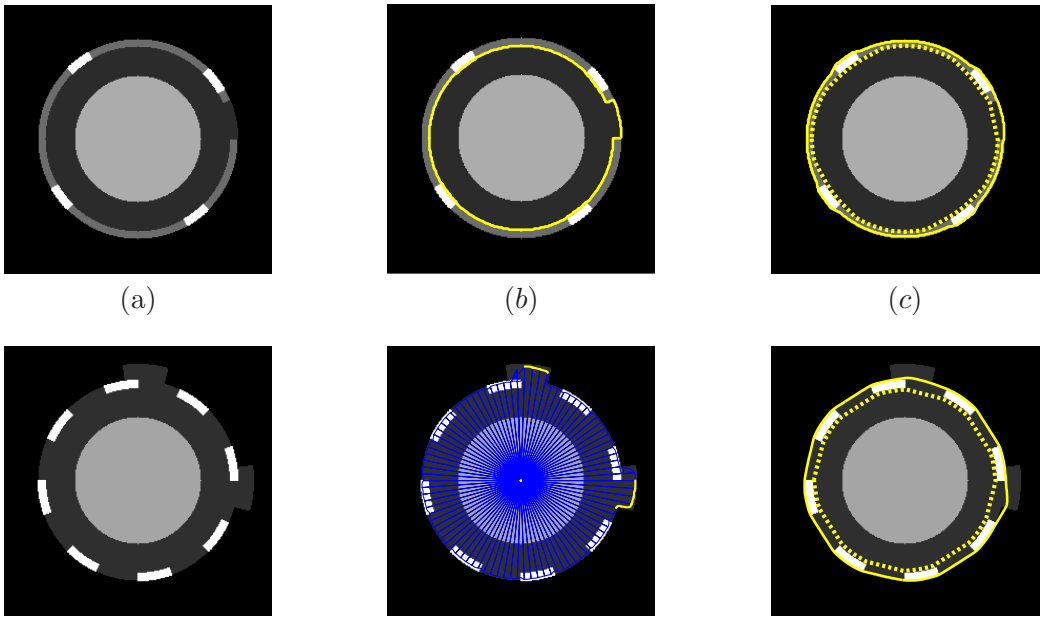

(a) (b) (c)

(d) (e) (f)

Figure 3.8: Artificial images ((a) and (d)) used to test the flexibility of the methods. (a) is characterized by a region with similar intensity between "thrombus" and "outer wall". (b) shows the thrombus initialization from the FMM and (c) depicts the result of our methods for the two boundaries. In artificial image (d), the same intensity between "thrombus" and "outer wall" has been set and there are two outer leakage regions. The DLR method result is shown in (e), where the leakage regions are in yellow (angle $\frac{\pi}{45}$). (f) shows the final result (LDRC is used, 30 iterations).

The number of slices that contained aneurysmal tissue in each data set varies from 29 to 56.

A vascular surgeon made a selection of the slices of interest, between the proximal and distal ends of the aneurysm and selected points for the outer wall boundary for each slice. The number of the points was large enough so that details of the shape of the boundaries could be captured. The contours were then obtained by linear interpolation of the selected points. For the thrombus, the aforementioned difficulty of similar intensity with the surrounding tissue is presented in many CTA slices and makes the task of selecting points which will provide a closed curve as its boundary rather difficult or even impossible if a guess is not allowed. To avoid this (such a guess) and use the manual segmentation result as our "gold standard" to validate our methods, the expert was requested to provide for each slice only the points of the thrombus boundary that he was certain of their position.

The manual segmentation was performed by a point selection tool of the medical image processing software ImageJ [1]. We then applied our segmentation method to all these slices of the ten data sets, tracing the thrombus and outer wall boundaries for each slice. A suitable cropping of each slice was made beforehand, selecting the region of interest, to decrease segmentation time as much as possible. We used parameter values mentioned in Sec. 3.5.1 and LDRC as the stopping criterion of choice.

3.5.4 Validation For The Outer Wall Boundary

The quantities used to evaluate segmentation error for the outer wall boundary for a slice were: Absolute and Relative Area Error (AAE and RAE), Mean Distance (MEDIS), Hausdorff Distance (HADIS) and Area Overlap (AO). We also extracted the Absolute and Relative Volume Errors (AVE and RVE) for each patient. AAE and RAE are given by

$$AAE = |A(M) - A(A)| \quad \text{and} \quad RAE = \frac{AAE}{A(M)}, \tag{3.5.2}$$

where $A(M)$ and $A(A)$ are the areas of the manual and automatic contours, respectively, measured in cm^2.

Mean and Hausdorff distances are used to quantify the similarity of the two curves. They are defined for the point clusters A and B as

$$MEDIS(A,B) = \max\{m(A,B), m(B,A)\}, \tag{3.5.3}$$

$$HADIS(A,B) = \max\{h(A,B), h(B,A)\}, \tag{3.5.4}$$

where

$$m(A,B) = mean_{a\in A}\{\min_{b\in B}\{d(a,b)\}\}, \tag{3.5.5}$$

$$h(A,B) = \max_{a\in A}\{\min_{b\in B}\{d(a,b)\}\}, \tag{3.5.6}$$

where $d(a,b)$ is a $L2$ norm for the points a and b. The main issue regarding these distances is that they only take into account the sets of points on both curves and do not reflect the course of the curve. We overcome this problem by finding 400 points on each of the two contours. These points are taken as the intersections of the curve with rays which start

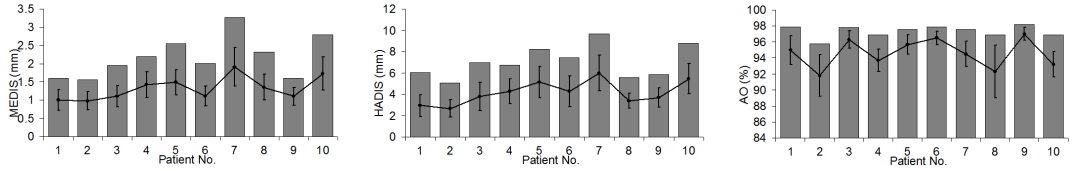

(a) (b) (c)

Figure 3.9: Evaluation of the segmentation error for the outer wall boundary: Mean Distance (MEDIS) in (a), Hausdorff Distance (HADIS) in (b) and Area Overlap (AO) in (c) for each of the ten data sets. Mean and Maximum values are depicted by the dots and the bars, respectively. Standard deviation is indicated by the error bars.

at the centroid of the contour and each two successive ones form an angle equal to $\frac{\pi}{200}$. In this way, we consider a large amount of points which are uniformly distributed along these convex or, in the worst case, star-shaped curves. We then calculate their MEDIS and HADIS (in mm), making these quantities together a very reliable measure of the resemblance of the two contours. Mean Distance denotes how close they really are and Hausdorff Distance identifies any outliers, which may be hidden in the averaging process of the Mean Distance, by providing the worst possible disagreement between the curves.

Area Overlap is defined as

$$AO = 2\frac{A(A \cap M)}{A(A) + A(M)}, \tag{3.5.7}$$

where $A(A \cap M)$ is the area of the intersection of the manual and automatic contours. For the per patient results, Absolute and Relative Volume Errors are defined as follows:

$$AVE = |V(M) - V(A)| \quad \text{and} \quad RVE = \frac{AVE}{V(M)}, \tag{3.5.8}$$

where $V(M)$ and $V(A)$ are the volumes of the manual and the semi-automatic segmentation, respectively. Volume for a data set is calculated as the product of the sum of the areas of the curves for all the slices of the set and the slice thickness [52]. Let us note that we do not present these volume errors as an error indication of the actual 3D volume. Given the fact that the in-slice distance is the same for all slices, the volume errors could be considered as a weighted error of all slices for each patient.

Table 3.1 summarizes the average results for the outer wall over the ten patient data sets. The mean of a quantity in these tables is the mean of the ten M_i's, $i = 1, \ldots, 10$, where M_i is the mean of this quantity over the slices of the i_{th} data set. Minimum and maximum values are also referring to these ten M_i's. Figure 3.9 presents analytically the results for each of the data sets for three of the above quantities used for evaluating the outer wall boundary segmentation error, namely the Mean Distance, the Hausdorff Distance and the Area Overlap. For the detailed results for all quantities, see the Appendix C, Tables C.1 and C.2. In Fig. 3.10 there are two slices with the manual and automatic outer wall contours superimposed ((a) and (b)).

Table 3.1: Summarized results for the outer wall: Mean, standard deviation, minimum and maximum values over ten patient data sets are provided for the quantities used to evaluate the segmentation error.

	mean±s.d.	[min,max]
No. of slices	45 ± 7	$[29, 56]$
Absolute Area Error (AAE, cm^2)	1.147 ± 0.355	$[0.654, 1.729]$
Relative Area Error (RAE, %)	6.0 ± 3.3	$[2.5, 13.1]$
Absolute Volume Error (AVE, cm^3)	4.563 ± 2.083	$[0.237, 7.079]$
Relative Volume Error (RVE, %)	4.0 ± 3.7	$[0.3, 12.4]$
Mean Distance (MEDIS, mm)	1.320 ± 0.318	$[0.978, 1.910]$
Hausdorff Distance (HADIS, mm)	4.160 ± 1.096	$[2.656, 5.999]$
Area Overlap (AO, %)	94.6 ± 1.8	$[91.8, 97.0]$

3.5.5 Validation For The Thrombus Boundary-Comparing Wall Thickness

The fact that the manual segmentation for the thrombus after the linear interpolation of the selected points includes only segments and not a closed curve for some slices is due to our desire of comparing only the points that the expert is certain of their position (see Sec. 3.5.3). We introduce a method for approximating the mean wall thickness of an AAA in a slice-by-slice fashion, which is used as a thrombus boundary validation. Following proper alignment of the thrombus and outer wall curves, we draw rays from the centroid of the wall, so that every two successive rays form the same angle ϕ. Six successive rays define a sector, so there are $\frac{2\pi}{5\phi}$ sectors (the angle of each sector is 5ϕ and ϕ should be chosen so that $\frac{2\pi}{5\phi} \in \mathbb{N}$). For a ray which intersects both the thrombus and outer wall curves, we define Ray Wall Thickness (RWT) to be the distance between these two intersection points. For a sector we define Sector Wall Thickness (SWT) to be the mean of the existent RWT over the rays of the sector. The mean SWT over all the sectors of all the slices of an AAA scan provides an evaluation of the mean wall thickness of the AAA.

One of the advantages of this method for estimating the wall thickness is that since we can increase the number of the sectors by reducing angle ϕ, we can have a detailed analysis of the wall thickness along the thrombus boundary. In addition, the result is independent of the number of points of the thrombus and outer wall curves. In Fig. 3.10(c) there is a slice which shows the manual and automatic thrombus and outer wall boundaries.

SWT is not calculated for all the sectors in the manual segmentation. For a sector that SWT is calculated, we define the Absolute Error of the Sector Wall Thickness (AESWT) as

$$AESWT = |MANSWT - AUTSWT|, \tag{3.5.9}$$

where MANSWT is the SWT of this sector for the manual segmentation and AUTSWT is the SWT of the corresponding sector for the semi-automatic segmentation. Corresponding sectors are the ones which possess the same order when they are sorted by moving clockwise starting from the first sector shown in Fig. 3.10(c) in magenta. The mean AUTSWT and mean MANSWT for each patient (which is the mean over all sectors) give a good

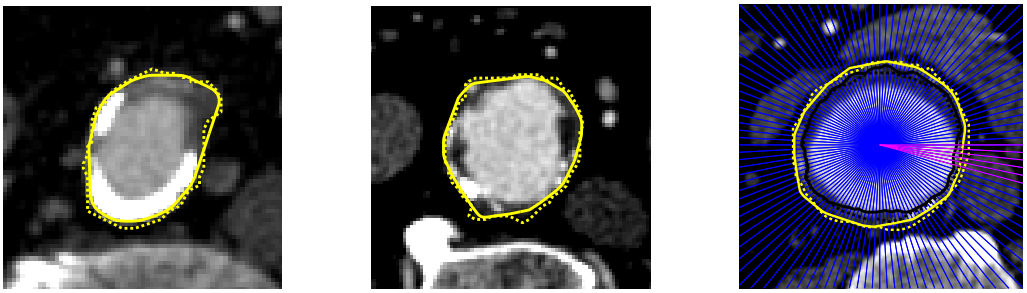

(a) (b) (c)

Figure 3.10: Examples of semi-automatic (continuous line) and manual (dashed line) segmentations for some slices, for the outer wall ((a) and (b)) and for the wall thickness ((c)). In (c) the method for evaluating mean wall thickness is depicted, with manual and automatic thrombus in black and manual and automatic wall in yellow. The angle ϕ of the rays is $\frac{\pi}{60}$. The first sector is shown in magenta.

approximation of the mean wall thickness of the AAAs that the two methods produce. For each patient we calculated the Absolute and Relative Errors of the Mean Sector Wall Thickness (AEMSWT, REMSWT), defined as

$$AEMSWT = |meanAUTSWT - meanMANSWT| \tag{3.5.10}$$

and

$$REMSWT = \frac{AEMSWT}{meanMANSWT}. \tag{3.5.11}$$

Table 3.2 includes the average results of all these quantities for the ten data sets we used. The mean of a quantity in these tables is the mean of the ten M_i's, $i = 1, \ldots, 10$, where M_i is the mean of this quantity over the slices of the i_{th} data set. Minimum and maximum values are also referring to these ten M_i's. Figure 3.11 presents analytically the results for each of the data sets for AESWT, AUTSWT and MANSWT. For all the details of the results for all the quantities, see the Appendix C, Tables C.3 and C.4.

The mean wall thickness for the ten patients is 2.575 ± 0.393mm and 2.993 ± 0.545mm for the semi-automatic and the manual segmentation, respectively. These results are close to the results of Di Martino *et al.* [21] where twenty six rectangular, circumferentially oriented AAA wall specimens were obtained fresh from the operating room from 16 patients undergoing elective repair of their AAA and the wall thickness measured was 2.5 ± 0.1mm, while 13 specimens were resected from nine patients during repair of their ruptured AAA and the measurement for wall thickness was 3.6 ± 0.3mm. This shows the effectiveness of this method. The difference between the manual thickness and the result of Di Martino *et al.* [21] can be explained: Our results are obtained from cross sections only, contrary to the referenced work where specimens were measured (that is why we presented this method basically for thrombus boundary validation and then for evaluating the mean wall thickness, not as a new method for a very accurate wall thickness measurement). In addition, the large manual wall thickness of the 3rd, 6th and 7th data sets (see Fig.

3.11(c)) which contribute to the large average manual mean wall thickness over the ten data sets, are due to the existence of quite a lot of large calcifications situated all around the circumference of the AAA wall.

Table 3.2: Summarized results for the wall thickness, which is used as evaluation of the thrombus boundary segmentation error: Mean, standard deviation, minimum and maximum values over ten patient data sets are provided for all the quantities. Angle $\phi = \frac{\pi}{60}$.

	mean±s.d.	[min,max]
No. of slices	45 ± 7	$[29, 56]$
Absolute Error of the Sector Wall Thickness (AESWT, mm)	1.127 ± 0.292	$[0.742, 1.683]$
Automatic (segmentation) Sector Wall Thickness (AUTSWT, mm)	2.575 ± 0.393	$[1.992, 3.129]$
Manual (segmentation) Sector Wall Thickness (MANSWT, mm)	2.993 ± 0.545	$[2.192, 3.814]$
Absolute Error of the Mean Sector Wall Thickness (AEMSWT, mm)	0.510 ± 0.411	$[0.017, 1.115]$
Relative Error of the Mean Sector Wall Thickness (REMSWT, %)	15.84 ± 11.38	$[0.66, 29.23]$

The mean AEMSWT and REMSWT for the ten data sets are 0.510mm and 15.84%, respectively. In absolute terms this relative error may be considered large. Martufi *et al.* [41] reports an average relative difference in AAA wall thickness of 7.8% after validating a wall thickness estimation algorithm by comparing with discrete point measurements taken from a cadaver tissue model. However, as no other similar result (i.e. using a manual segmentation) is available in the literature, we cannot deduce that our result is indeed large. In addition, the absolute error can be considered acceptable as it corresponds approximately to 0.68 pixels, taking into consideration the mean pixel width for the ten data sets. This shows that the thrombus boundary segmentation, using our methods, is fairly accurate. Tests showed that these results are not sensitive to the choice of angle ϕ and for every angle smaller than $\frac{\pi}{60}$ the differences of the errors of Table 3.2 are very small. Some difficult to handle case-slices, which provide some of the worst results as shown in Fig. 3.11, are presented in Sec. 3.7.1 and highlight the limitations of our methods.

3.5.6 Comparison Of The Three Stopping Criteria

We will now compare the three stopping criteria introduced in this Chapter (Fig. 3.12 shows the final outcome for the outer wall for a cross section, using the three stopping criteria). The most preferable stopping criterion is the one that allows the fewest iterations for the LSM in outer wall segmentation. To compare the three criteria, we applied them on three out of the ten data sets. We used 131 slices for this comparison (see Fig. 3.13). LDRC gave the best results in 68% of these slices, IECC in 37% and SC in 5%. The performance of the SC is due to the fact that there might be the case of even a single sector for which the relative area change is continuously reducing (so the curve delays to

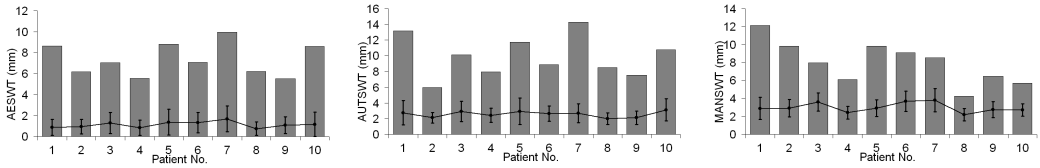

(a) (b) (c)

Figure 3.11: Evaluation of the segmentation error for the thrombus boundary: Absolute Error of the Sector Wall Thickness (AESWT) in (a), Automatic (segmentation) Sector Wall Thickness (AUTSWT) in (b) and Manual (segmentation) Sector Wall Thickness (MANSWT) in (c) for each of the ten data sets. Mean and Maximum values are depicted by the dots and the bars, respectively. Standard deviation is indicated by the error bars.

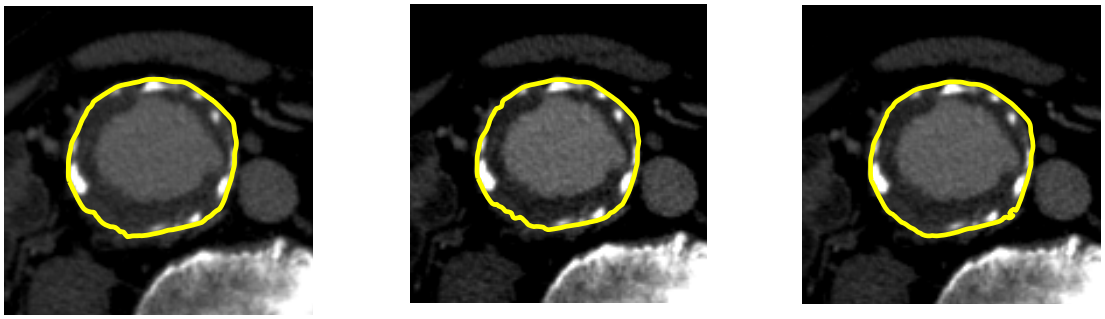

(a) (b) (c)

Figure 3.12: Results for the outer wall for a cross section, using SC (image (a), sector angle $\frac{\pi}{8}$, 70 iterations), LDRC (image (b), 40 iterations) and IECC (image (c), 130 iterations).

stop). On the other hand in IECC, since the motion of the two curves is produced by applying the level set equation, there might be a delay of their contact. The types of leakage regions in a slice (large or small, many or few) do not prohibit the use of any of the three criteria. However, IECC allows more iterations than the other two when there is a narrow leakage region, as the inner curve delays to enter the leakage region and intersect the outer curve. LDRC generally detects leakage earlier than the other two but not always: IECC can be more preferable (see Fig. 3.13(c)) if leakage regions are large and wide. On the other hand, if there are a lot of small leakage regions, SC will have a faster response. Ideally, one would apply all three criteria and select the one which allows the fewest iterations, but this is time consuming. In our experiments we used the LDRC.

3.6 Sensitivity Analysis-Reproducibility-Segmentation Time

The parameters used are quite a few (see Table 3.3) and we performed experiments to test the sensitivity of the results to the parameter settings. As far as the gaussian filter is concerned, a small change to the size of the filter or to the width s does not

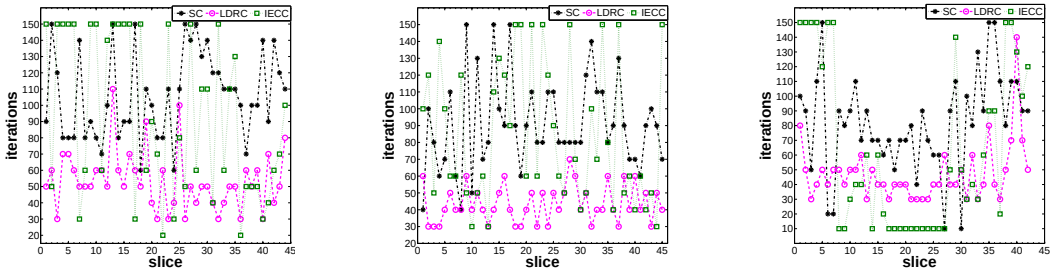

(a) (b) (c)

Figure 3.13: Comparison of the performance of the three stopping criteria (SC, LDRC and IECC) for three data sets. The most preferable stopping criterion (the one which detects the leakage earlier than the others) is: LDRC in 73% of the slices in (a), LDRC in 84% in (b) and IECC in 52% in (c).

Table 3.3: Parameters used in our model and their values in the experiments.

Fast Marching Method (Section 3.3.1.1)		
λ	50	weight of the intensity modulus (Eqs. (3.3.2), (3.3.3))
s	1	width of the 5×5 Gaussian filter (Eq. (3.3.4))
Level Set Method (Section 3.3.2.1)		
λ	0.1	weight of the intensity modulus (Eqs. (3.3.10), (3.3.3))
s	1	width of the 5×5 Gaussian filter (Eq. (3.3.4))
c	5000	parameter used in Eq. (3.3.10) for faster convergence

affect the accuracy of the method. Parameter c (chosen equal to 5000) makes the curve to move faster and increases the rate of convergence. Other values of the same order of magnitude for c provide very similar results at almost the same segmentation time. The quality of the results is slightly more sensitive to the parameter λ, which is the weight of the squared modulus of the convolution of the intensity with the gaussian. From our experiments we concluded that, for the LSM, λ should be of order of magnitude 10^{-2} when $\sigma = |\max I - \min I|$ is of order 10^3 (where $I(x, y)$ is the intensity of the point (x, y) in the 2D image). For every decrease of order of magnitude for σ (something which usually happens after cropping the image) there should be a similar increase in the order of magnitude for λ. Image cropping for almost all the cases of the experiments resulted in a σ of order 10^2, therefore we set $\lambda = 0.1$. With this choice, g_I is approximately equal to 1 away from the image boundary (so the front moves fast in these regions) and approximately equal to 0 near the target boundary. If λ is larger, the front motion away from the target boundary will be rather slow and if it is smaller the front will not stop at the boundary being tracked, as leakages will occur. This choice of the order for λ is not necessary in the FMM due to the speed of this method, so, setting a large value to λ ($\lambda = 50$) is sufficient. In conclusion, a slight change in the value of a parameter does not influence the results of the method, thus verifying its robustness.

The value for the order of magnitude of the relative area change in the DLR method

($r = 10^{-2}$ or greater) does not depend on any factors due to the local nature of this method and has been obtained after experimentation. Sectors characterized by a lower order than that refer to the parts of the curve which tend to stop, so they are not taken into account. The extension of the smallest circle containing the inner initialization by $p = 1.5$ pixels in the IECC is the same for every case and with this choice (which is the result of experiments) we make sure that the inner and outer curves do not, initially, intersect and that they are in proximity to each other. This will allow the inner curve to evolve so that a more accurate (due to the LSM) result is obtained. Finally, in the TWBD method, the order $d = 1mm$ is the obvious choice, given the popular mean wall thickness of approximately $2mm$, so that a proper distance is set in regions where thrombus and outer wall boundaries are too close to each other.

We will now refer to the sensitivity of the result to the user intervention which amounts to the choice of the start and end points of the FMM. A small perturbation of the start or end point placed for the thrombus initialization may lead to an unsatisfactory result. This is due to the non-uniform intensity distribution that exists near the thrombus boundary or within the thrombus region and the fact that the user must select points of similar intensity for each pair, with a similar intensity path existing between them (as mentioned in Sec. 3.5.1). These issues have been addressed with the modifications of the FMM presented in Sec. 3.5.1, in order to establish the reproducibility of the results in a more efficient way.

Time is another important factor in an AAA segmentation, as in a clinical setting it becomes a time-critical application. Table 3.4 presents execution time results of the methods for the initialization and segmentation of thrombus and outer wall boundaries in five data sets (patients 6 to 10), following appropriate cropping of the initial image. Results are given as mean±s.d.(min,max) and they include delays caused by the user, such as the time required to make a correct decision regarding the start and end points in the FMM. In addition, the direct user involvement is about 24% of the total processing time. The results in Table 3.4 show that the mean initialization, thrombus, outer wall and total processing times per slice for the five data sets were 1.30, 1.56, 2.69 and 5.96 minutes, respectively. The total processing time for a slice is the sum of the initialization, thrombus and outer wall times increased by 25 seconds, which is the typical execution time of the TWBD method that was used in almost all cases. LDRC has been used for these results, as well. These execution times can be considered satisfactory, provided that the codes are in MATLAB(we used a Pentium 4 with CPU 3 GHz and 1 GB of RAM). The wall-clock time for each run of the code implementing the DLR method is about five minutes. Some apparently long execution times are due to the reinitialization routine which is used every ten iterations, in which the level set function becomes a signed-distance function by solving a computationally expensive level set reinitialization equation [46]. Suggestions for reducing segmentation time are made in Sec. 3.7.1.

Table 3.4: Execution time of the methods (per slice) in five data sets, given as mean±s.d.(min,max). In each column, the values of the last four rows have been extracted from the five mean values of the previous five rows.

Patient No.	No. of slices	Initialization time (min)	Thrombus time (min)	Outer wall time (min)	Total time (min)
1	44	$1.47 \pm 0.41(0.71, 2.55)$	$1.20 \pm 0.30(0.39, 1.94)$	$3.34 \pm 0.93(2.08, 7.84)$	$6.42 \pm 0.99(5.17, 11.19)$
2	45	$1.75 \pm 0.47(0.90, 3.07)$	$1.60 \pm 0.46(0.70, 2.91)$	$2.72 \pm 0.67(1.80, 4.79)$	$6.48 \pm 0.95(4.86, 8.68)$
3	42	$0.99 \pm 0.28(0.50, 1.89)$	$1.76 \pm 0.80(0.85, 4.01)$	$2.56 \pm 0.86(1.55, 5.59)$	$5.73 \pm 0.86(3.93, 8.40)$
4	52	$1.18 \pm 0.29(0.53, 1.97)$	$1.66 \pm 0.44(1.07, 3.00)$	$2.57 \pm 0.60(1.75, 5.08)$	$5.82 \pm 0.95(4.51, 9.07)$
5	51	$1.11 \pm 0.29(0.59, 1.91)$	$1.58 \pm 0.46(0.95, 3.03)$	$2.27 \pm 0.54(1.50, 3.72)$	$5.37 \pm 0.74(4.11, 7.17)$
mean	47	1.30	1.56	2.69	5.96
s.d.	4	0.31	0.21	0.40	0.48
min	42	0.99	1.20	2.27	5.37
max	52	1.75	1.76	3.34	6.48

3.7 Discussion

3.7.1 Limitations

The method proposed to segment the AAA outer wall and thrombus boundaries relies on the LSM which is an intensity gradient based technique. As a result the method relies on the presence of an intensity gradient in the vicinity of the boundary that is strong enough to attract the LSM front. Such intensity gradient can be either due to the contrast produced by the imaging method at the interface between tissue of different composition such as the arterial wall and the intraluminal thrombus and / or the existence of calcified deposits in the arterial wall. Our methods exploit the latter source of contrast by introducing various geometrical tools to overcome the insufficient presence of the former source of image contrast. Therefore for the method to be effective some source of image contrast should be present. This is depicted in Fig. 3.14(a), where one of the largest maximum HADIS of the ten data sets for the outer wall, equal to 8.192mm, appears (see Fig. 3.9(b), patient number 5).

As the basic information utilized is calcifications, a reference should be made regarding the frequency of their presence inside the AAA wall. In Siegel *et al.* [53] thin discontinuous calcifications were found in 27/52 cases in ruptured group and 23/56 in unruptured group. Unfortunately Siegel *et al.* [53] did not quantify their distribution. Lindholt *et al.* [36] recorded the circumferential distribution of calcifications at the maximal diameter cross section and reported 62/122 AAA patients having more than 50 % of that circumference covered by them. Li *et al.* [35] studied the effects of calcifications on the computed AAA wall stress distribution and reported for a group of 20 patients a mean value of 4.6 % calcification per total AAA volume ratio. Moreover, a careful study of the geometric characteristics of the AAA wall when calcifications are present is important as their presence may cause a significant alteration of the stress distribution, thus affecting rupture risk assessment [56, 35].

A further limitation is related to the presence of sources of high image contrast, such as the spine, very close to the outer wall, which attract the propagating LSM front away

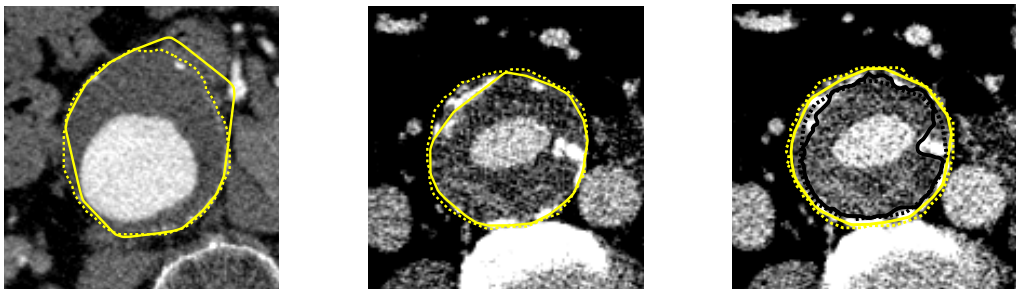

(a) (b) (c)

Figure 3.14: Examples of cross sections which are difficult to segment and show the limitations of the methods. Continuous lines depict the semi-automatic segmentation and dashed lines the manual one. The outer wall boundary is in yellow and the thrombus boundary (in (c)) is in black.

form the tracked boundary. In order to avoid considering the spine as a calcification from our method, due to thresholding, which would result in a large error in the wall boundary detection, we select a large threshold in the method we use for the reconstruction of the outer wall boundary. Inevitably with this choice, some calcifications are not detected and are thus excluded from the outer wall boundary created (see Fig. 3.14(b), where the maximum AAE among the slices of the third data set, equal to $2.821cm^2$, appears).

As the method is based on the assumption that calcified deposits are located within the arterial wall, in cases where this is not true and there are calcifications within the thrombus, incorrect thrombus boundary tracking may result. This is the main cause of the appearance of large values of AESWT in certain slices of the data sets. In Fig. 3.14(c) there is a slice where this internal calcifications issue is demonstrated and a large AESWT, equal to 7.03mm, appears (see Fig. 3.11(a), the maximum value of patient number 3). A final issue which is a limitation in terms of the clinical application of the method is the relatively long time required to complete the segmentation which was in this implementation approximately 6 minutes per slice (see Table 3.4). However, this issue can be resolved by taking measures such as using a narrow band LSM, avoiding the reinitialization step of the method by adding an extra term to (6) associated to an internal energy which penalizes the deviation from a signed distance function and by coding the methods in C++.

3.7.2 Comparison With Other Methods

We next compare quantitatively our results with that of related works. Subasic *et al.* [58] used a 3D level sets method, requiring minimal user intervention. They report an average relative error on a slice 12.35%. 11 real patient data sets were used for the validation (the mean RAE of our segmentation method for the outer wall is 6%, see Table 3.1). The method is not performing accurately where the AAA has significant concavities. Magee *et al.* [40] reported a total segmentation time of less than two hours. A comparison between the automatic method and an interactive segmentation was made by evaluating

the minimum distance slice by slice, and the mean was 0.57mm (four volumes were used). In Zhuge *et al.* [63] user intervention is not required beyond identifying the most proximal and distal slices concerning the aneurysm. The method assumes that the aneurysm is roughly circular in transaxial cross section. The mean segmentation time per patient is 7.4 ± 3.8min(s.d.), implying a very fast method. The results of a comparison with a manual tracing for the outer wall were 3.5% for the mean RVE and $0.8cm^2$ for the mean AAE (20 patient data sets were used). Our corresponding results are 4.0% and $1.147cm^2$, respectively (see Table 3.1).

In De Bruijne *et al.* [16] the time required for expert segmentation may be reduced by a factor of six, but manual intervention is required in one of six slices and the user must redraw the entire contours. Image data from 23 patients were used and the comparison with a manual segmentation provided an average RVE of 1.5% and an average volume overlap of 95.8% (the mean AO for the data sets we used is 94.6%, see Table 3.1). In De Bruijne *et al.* [15] obtained volume errors with respect to a manual segmentation are comparable to manual inter-observer errors in roughly 90% of the cases (the mean unsigned volume error is 4.0% and the average volume overlap is 94%, values very close to the corresponding ones in Table 3.1). In Olabarriaga *et al.* [45] the average per case deformation time for 17 scans was 41 ± 69.3secs. However, in ten (out of 17) cases, small and localized bumps into the bowels and vena cava were observed and would possibly require manual correction. In addition, the segmentation method's performance depends on the quality of training. A comparison of the results of the method with a manual segmentation for 17 patient scans provided a mean segmentation overlap of 95.0%, a mean volume error of 4.5%, a mean segmentation error of 1.3mm and a mean maximum distance of 5.5mm. The corresponding results as shown in Table 3.1 are 94.6%, 4.0%, 1.320mm and 4.160mm, respectively. Therefore our results are comparable with the results of most of these works which, however, offer no distinction between thrombus and outer wall or assume uniform wall thickness.

3.8 3D Results

As mentioned in the Introduction of this Chapter (Sec. 3.1), one way to obtain the 3D reconstruction of the AAA anatomy is through the application of a 3D surface reconstruction method to all the segmented 2D slices which constitute the structure of interest. Figure 3.15 presents 3D reconstructions of the thrombus and outer wall surfaces (excluding the common iliac arteries) created from the segmented 64 CTA images of the first data set we used, using the purpose-developed software found in [27]. The extracted boundaries from our methods are also shown in this figure.

Due to limitations of this reconstruction tactic, mainly concerning time and accuracy, extraction of the surfaces of interest in one step using a 3D segmentation approach with an application directly to 3D data is usually preferred. The FMM and Gabriel Peyré's Toolbox [47] were also used in the 3D case to obtain a good initialization for the LSM. We used speed g_I with $\lambda = 50$ and a $5 \times 5 \times 5$ Gaussian filter G_s with $s = 1$. Similar to the 2D case, the user typically gives a pair of points. The starting point is usually selected in the center of the 3D image, while the ending point is chosen at the bottom of the image

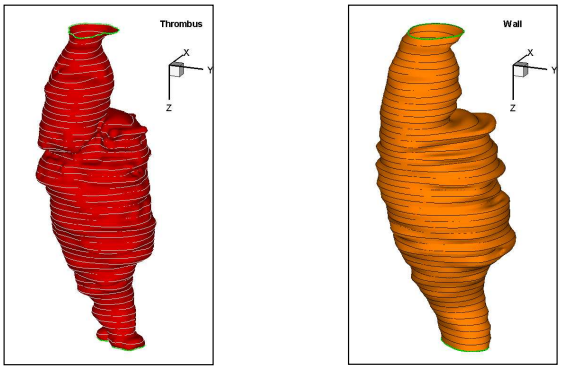

(a) (b)

Figure 3.15: The 3D thrombus in (a) and outer wall in (b) surfaces of a data set reconstructed from the segmented 2D images (the extracted boundaries are also shown) using purpose-developed software.

(on the last cross section), usually inside one of the common iliac arteries. But, as in the 2D case, we made a modification which allows to provide two pair of points. These are selected taking into consideration two things: Firstly, the union of the two surfaces (one for each pair) should provide almost the whole structure of interest, so that LSM, which will later fix all the segmentation details, does not take a very long time. Secondly, the cross sections of a starting point and of its corresponding ending point should be as close as they can be, so that the whole initialization surface stays inside the under detection surface. These two matters are of crucial importance for an accurate final result, so the FMM is always implemented in our 3D results providing two pair of points which satisfy them.

The 3D LSM was implemented using the "Toolbox of Level Set Methods" [44], created by Ian Mitchell in MATLAB. Proper adjustments were made to it so that the initial surface from the FMM and the medical image data can be used as input and so that (3.3.10) is implemented. Similar to the 2D case, we took $\lambda = 0.1$, $c = 5000$ and a 5×5 Gaussian filter with $s = 1$. The volume of interest is selected in the beginning, aiming to reduce segmentation time.

Figure 3.16 shows a result for the lumen, using 3D FMM for the initialization and 3D LSM for the final surface. The usually good contrast between lumen and its surroundings suggests that these two methods are by themselves appropriate for its segmentation, without needing any geometrical methods like the ones implemented for the 2D thrombus and outer wall segmentation. Segmentation time for this result, though, was approximately 1 hour 20 minutes.

As a first "validation" of the 3D lumen result, superimposition of transverse planes of the 3D surface to the related CT images was made. These transverse planes were taken using ParaView [29], which is an open-source, multi-platform data analysis and visualization application. Figure 3.17 shows two superimpositions ((a) and (c)), where the transverse planes of the initial surface are also shown. The corresponding 2D level set results are also depicted in this figure to make another useful comparison and conclude that the 3D lumen surface reconstructed with LSM is quite accurate. Development of

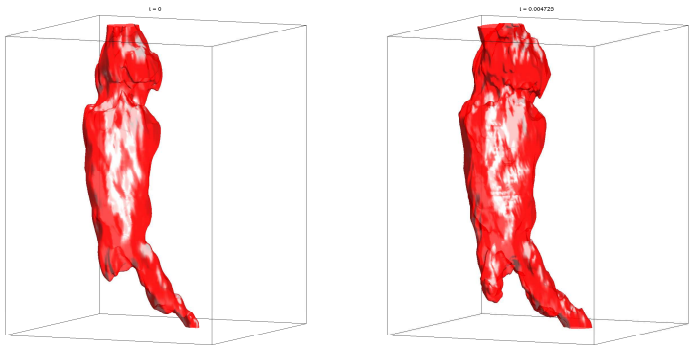

(a) (*b*)

Figure 3.16: A result for the lumen with 3D level sets. The result of the 3D FMM (initialization) is shown in (a) and the result of the 3D LSM (final surface) is shown in (b).

related to 2D stopping criteria and 3D boundary creation methods for the thrombus and outer wall are our next future plans.

3.9 Conclusion

Geometrical methods and tools for the LSM based segmentation of AAA thrombus and outer wall boundaries in CTA images exploiting the presence of calcifications in the arterial wall are presented. Stopping criteria were introduced to address the problem of leakage that intensity gradient based methods are susceptible to. Validation of the methods by comparison with manual segmentations from an expert showed a 4.0% relative volume error, a 1.32mm mean distance and a 94.6% area overlap for the outer wall boundary, averaged over ten patient data sets. Similarly the comparison for the mean wall thickness produced a mean absolute error of 0.51mm and a relative error of 15.84%. The robustness of the method was also assessed through sensitivity and reproducibility analyses. These results indicate that geometrically accurate 3D reconstructions of AAA anatomy and reliable measurements of the wall thickness distribution can be produced through LSM based segmentation of image data obtained from currently available imaging technology. Such information is important in estimating wall stress distribution which is required in obtaining a reliable patient specific measure of AAA rupture risk. Future work will include improvements in the model to reduce user intervention and accelerate the segmentation process and the extension of our model to three dimensions to avoid the 2D segmentation phase.

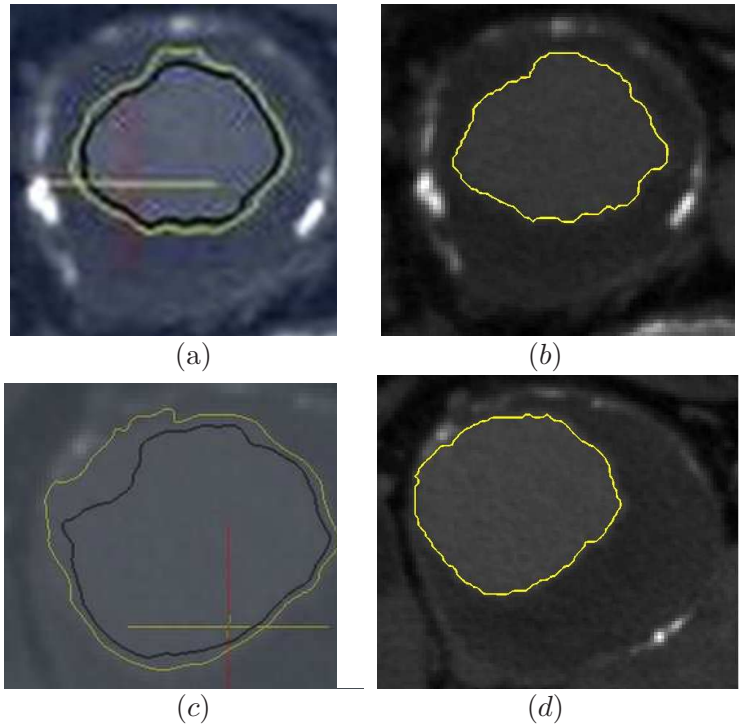

(a) (b) (c) (d)

Figure 3.17: Superimpositions of two transverse planes of the 3D lumen initialization and final surface of Fig. 3.16 to the two related CTA images are shown in (a) and (c). The initial surface is in black and the final surface in yellow. The 2D level set results for the corresponding cross sections are depicted in (b) and (d).

Chapter 4

Conclusion

Viscosity solutions, a class of weak solutions of nonlinear scalar partial differential equations, are a notion with great value due to the very general existence, uniqueness and stability results which characterize them for a wide class of equations. Their role is important in a great range of applications, two of which were analyzed in this thesis.

The first application was the Shallow Lake Problem. This is an optimal control problem derived from the combination of the two utilities of a shallow lake: agricultural activities and ecological services. Our basic result was the extraction of an optimal HJB (OHJB) equation that the value function of this problem satisfies in the viscosity sense. Many regularity results for the value (welfare) function were then extracted using this result. In addition, we approximated the viscosity solution with monotone numerical schemes, based on a finite difference space discretization. Finally, we used the Simple Shooting Method as a "gold standard" to compare with and validate our results. The accuracy of these numerical approximations was satisfactory, as the mean relative error was between 0.02% and 0.06%, depending on the number of the saddle points and the spatial step (Table 2.1). We can conclude that the extraction of (OHJB) is an important result and the fact that the value function is its viscosity solution can probably lead to many other future results which will help to investigate the Shallow Lake Problem deeper.

The second application, analyzed in Chapter 3, was the extraction of the thrombus and outer wall boundaries from cross sections of a 3D CTA AAA image data set, using the level set framework and new geometrical methods to address the basic problem of no sufficient contrast between thrombus and surrounding tissue. Adequate information, including calcifications, sufficient intensity contrast or information from neighboring regions, was essential to achieve this task. We introduced two new geometrical methods which exploit the presence of calcifications to reconstruct the thrombus and outer wall boundaries. We also introduced three novel stopping criteria to address the leakage problem that LSM's present and a method for detecting the leakage regions. A manual segmentation, created by a medical expert, was performed to compare with our results. Ten patient data sets (450 slices) were used for this validation. The relative volume error, mean distance and area overlap were three of the quantities used to evaluate outer wall segmentation error (Table 3.1). A method for approximating the mean wall thickness, created for validating the thrombus boundary segmentation, was introduced (see Table 3.2 for these results).

The results for the outer wall and for the mean wall thickness are comparable to those of other works in which, however, there is no segmentation of the thrombus boundary. Accurate 3D reconstructions created from the results of the 2D LSM-based segmentation will help to estimate the wall stress distribution and obtain a reliable measure of AAA rupture risk. Acceleration of the segmentation process and the extension of the model to three dimensions (developing related 3D geometrical methods and stopping criteria) are basic future plans on this work.

Appendix A

Proof Of Lemmas 2.2.1 and 2.2.2

A.1 Proof Of Lemma 2.2.1

Proof: We denote O.D.E system (2.2.7) as

$$\begin{cases} x'(t) = f_1(x, a) \\ a'(t) = f_2(x, a). \end{cases}$$

Solving system

$$\begin{cases} f_1(x, a) = 0 \\ f_2(x, a) = 0, \end{cases}$$

with respect to x, we deduce that

$$k(x) = 1.2x^6 - 2x^5 + (1.8 - \rho)x^4 - 2x^3 - 2\rho x^2 + 2x - (0.6 + \rho) = 0 \tag{A.1.1}$$

Giving ρ a specific value, the roots of $k(x)$ in $[0, 2]$ are the equilibrium points of O.D.E. system (2.2.7) in $[0, 2]$. We have that $k(0) = -(0.6 + \rho) < 0$ and $k(2) = 29 - 25\rho > 0$ for $\rho \in (0, 0.4]$, so $k(x)$ has 1 or 3 or 5 roots in $[0, 2]$. Supposing there are 5 roots there, then $k(x)$ would have 6 real roots. Taking its fourth derivative and applying Roll's Theorem successively for four times we deduce that $k^{(4)}(x) = 432x^2 - 240x + 43.2 - 24\rho$ has 2 roots in $\mathbb{R}$. Its discriminant is $D = -17049.6 + 41472\rho$ and for $\rho \in (0, 0.4]$ D is negative, which is a contradiction. We conclude that $k(x)$ has 1 or 3 roots in $[0, 2]$, which means that there are 1 or 3 equilibrium points of (2.2.7) in $[0, 2]$. □

A.2 Range Of The Discount Factor Values For One Or Three Equilibrium Points

We will now find (graphically) the range of ρ in which each of the above two cases described in Lemma 2.2.1 occur (we will need this approximation for the proof of Lemma 2.2.2). Solving (A.1.1) with respect to ρ, we take

$$\rho = \frac{1.2{x_{s0}}^6 - 2{x_{s0}}^5 + 1.8{x_{s0}}^4 - 2{x_{s0}}^3 + 2x_{s0} - 0.6}{({x_{s0}}^2 + 1)^2} \tag{A.2.1}$$

where x_{s0} is the abscissa of the equilibrium point. Graph $\rho - x_{s0}$ is depicted in Figs. A.1(a) and A.1(b). From these we see that, lines $\rho = 0.096$ and $\rho = 0.164$ cross the graph at one point but lines $\rho = 0.097$ and $\rho = 0.163$ cross the graph at three points.

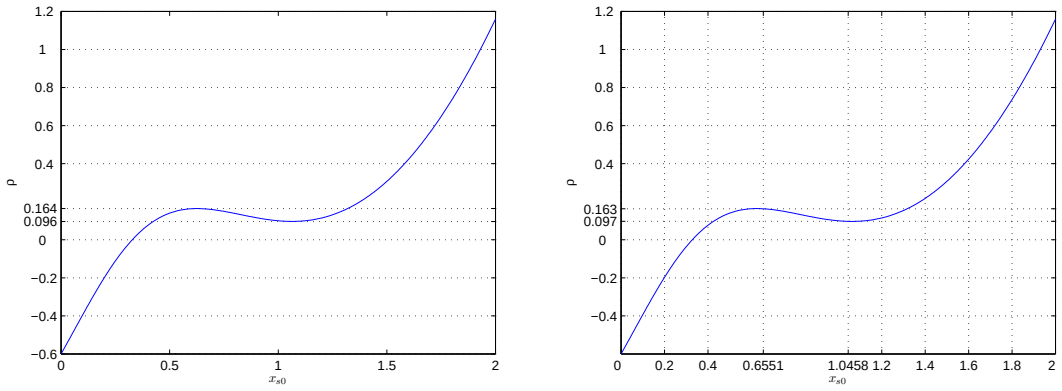

(a) (b)

Figure A.1: x_{s0} is the abscissa of the equilibrium point and ρ the discount factor. The two lines in (a) cross the graph at one point but the two lines in (b) cross the graph at three points.

Rounding ρ to the third decimal digit, we deduce that

- if $\rho \in (0, 0.096]$, then there is one equilibrium point
- if $\rho \in [0.097, 0.163]$, then there are three equilibrium points
- if $\rho \in [0.164, 0.4]$, then there is one equilibrium point.

Remark A.2.1. If ρ_m, ρ_M are the local minimum and local maximum for function

$$S(x_{s0}) = \frac{1.2{x_{s0}}^6 - 2{x_{s0}}^5 + 1.8{x_{s0}}^4 - 2{x_{s0}}^3 + 2x_{s0} - 0.6}{({x_{s0}}^2 + 1)^2}$$

in $[0, 2]$, respectively, then we can say that for $\rho \in (0, \rho_m) \cup (\rho_M, 0.4]$ there is one equilibrium point and for $\rho \in (\rho_m, \rho_M)$ there are three equilibrium points (for $\rho = \rho_m$ or $\rho = \rho_M$, (A.1.1) has one double and one single root. This is a degenerate case, appearing at the border of the two domains of ρ in which the two cases occur, which is not examined in this work).

A.3 Proof Of Lemma 2.2.2

Proof: We find a necessary and sufficient condition for equilibrium point (x_{s0}, a_{s0}) to be a saddle point. We calculate the stability matrix for system (2.2.7) at (x_{s0}, a_{s0}) and

then we try to find its eigenvalues λ. We finally find the following trinomial

$$\lambda^2 - \rho\lambda + 2a_{s0}\left(\frac{-0.6x_{s0}({x_{s0}}^2+1)^3 + 2{x_{s0}}^2({x_{s0}}^2+1) + 3{x_{s0}}^2 - 1}{({x_{s0}}^2+1)^3} - a_{s0}\right) = 0. \quad \text{(A.3.1)}$$

(x_{s0}, a_{s0}) is a saddle point if and only if this trinomial has two roots, one positive and one negative. Denoting $t(x_{s0}) = \frac{-0.6x_{s0}({x_{s0}}^2+1)^3+2{x_{s0}}^2({x_{s0}}^2+1)+3{x_{s0}}^2-1}{({x_{s0}}^2+1)^3}$ we have that, if λ_1, λ_2 are the roots of the trinomial, this is the case if and only if $2a_{s0}\left(t(x_{s0}) - a_{s0}\right) < 0$, using Vieta's formulae. We have that $a_{s0} > 0$, so we finally conclude that our necessary and sufficient saddle-point condition is $t(x_{s0}) < a_{s0}$. We also have that $f_1(x_{s0}, a_{s0}) = 0 \Rightarrow a_{s0} = 0.6x_{s0} - \frac{{x_{s0}}^2}{{x_{s0}}^2+1}$. So, denoting $w(x_{s0}) = 0.6x_{s0} - \frac{{x_{s0}}^2}{{x_{s0}}^2+1}$, the above condition is

$$w(x_{s0}) > t(x_{s0}).$$

The graphs of $w(x_{s0}), t(x_{s0})$ in $x_{s0} - a_{s0}$ diagram are depicted in Fig. A.2(a) and from it, rounding to the third decimal digit, we conclude that

$$(x_{s0}, a_{s0}) \text{ is saddle point} \Leftrightarrow x_{s0} \in [0, 0.626) \cup (1.063, 2].$$

Remark A.3.1. If x_1, x_2 are the roots of $w(x_{s0}) - t(x_{s0}) = 0$ in $[0, 2]$, $x_1 < x_2$, then (x_{s0}, a_{s0}) is saddle point $\Leftrightarrow x_{s0} \in [0, x_1) \cup (x_2, 2]$.

As mentioned in Lemma 2.2.1, we have the following cases :

- There is one equilibrium point. Then $\rho \leq 0.096$ or $\rho \geq 0.164$. We have that $k(0.626) = 0.3177 - 1.9373\rho$ and $k(1.063) = 0.4388 - 4.5363\rho$. We have shown that $k(0) < 0$ and $k(2) > 0$. If $\rho \leq 0.096$ then $k(0.626) > 0$, so $x_{s0} \in [0, 0.626]$ and we conclude that (x_{s0}, a_{s0}) is a saddle point. If $\rho \geq 0.164$ then $k(1.063) < 0$, so $x_{s0} \in (1.063, 2]$ and we make the same conclusion. So, (x_{s0}, a_{s0}) is always a saddle point.

  Remark A.3.2. If we don't want to make a rounding we must show that, if $\rho < \rho_m$ then $k(x_1) > 0$ and if $\rho > \rho_M$ then $k(x_2) < 0$.

- There are three equilibrium points. Then, $0.097 \leq \rho \leq 0.163$. For ρ at this range, we have that $k(0.626) > 0$ and $k(1.063) < 0$. So, if $(x_{s1}, a_1), (x_{s2}, a_2), (x_{s3}, a_3)$ are the three points, then $x_{s1} \in (0, 0.626)$,
  $x_{s2} \in (0.626, 1.063)$, $x_{s3} \in (1.063, 2)$ which means that the first and third points are saddle points but the second one is not. We focus on the second point. We find the discriminant D of trinomial (A.3.1) and (x_{s0}, a_{s0}) is a vortex (with outward direction) iff $D < 0$ (if $D < 0$, using Vieta's formulae, $2Re(\lambda_i) = -\frac{-\rho}{1} > 0 \Rightarrow Re(\lambda_i) > 0$ so (A.3.1) has two complex conjugate roots with positive real parts). This condition is the following:

$$\rho < \frac{\sqrt{8[0.6x_{s0}({x_{s0}}^2+1) - {x_{s0}}^2]}}{{x_{s0}}^2+1} \cdot \frac{\sqrt{[-1.2x_{s0}({x_{s0}}^2+1)^3 + 2{x_{s0}}^2({x_{s0}}^2+1) + {x_{s0}}^2({x_{s0}}^2+1)^2 + 3{x_{s0}}^2 - 1]}}{{x_{s0}}^2+1}$$

Denoting $y(x_{s0})$ the right part of this inequality and writing relation (A.2.1) as $\rho = z(x_{s0})$, we conclude that (x_{s0}, a_{s0}) is a vortex if and only if

$$y(x_{s0}) > z(x_{s0}).$$

The graphs of $y(x_{s0}), z(x_{s0})$ in $x_{s0} - \rho$ diagram are depicted in Fig. A.2(b) and from it, rounding to the third decimal digit, we conclude that

$$(x_{s0}, a_{s0}) \text{ is a vortex} \Leftrightarrow x_{s0} \in [0.658, 1.050].$$

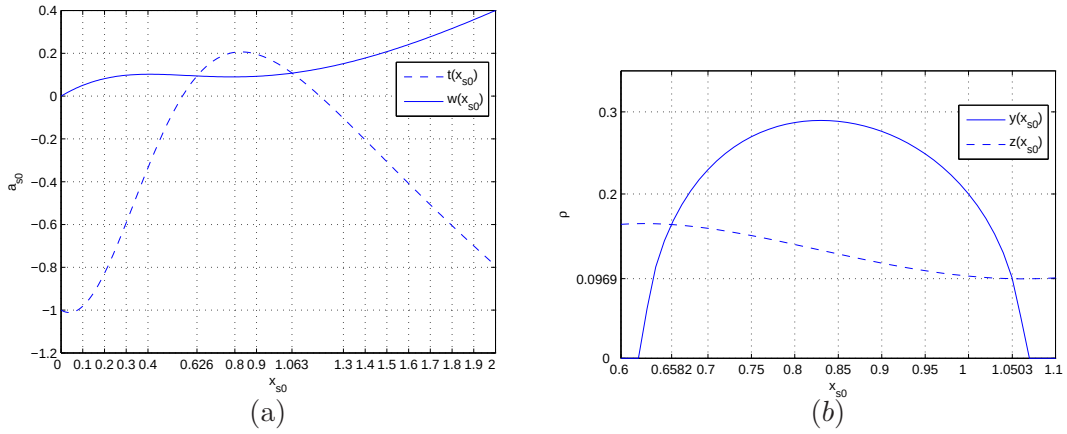

(a) (b)

Figure A.2: Graphs used in the proof of Lemma 2.2.2. x_{s0}, a_{s0} are the coordinates of the equilibrium point and ρ is the discount factor.

From Fig. A.1(b), approximating at the fourth decimal digit, we see that $x_{s2} \in [0.6551, 1.0458]$. So we conclude that (x_{s2}, a_2) is a vortex, except of some degeneracies (as it is also mentioned in [54], page 538) which we meet when $x_{s2} \in [0.6551, 0.658)$ (e.g. if $\rho = 0.163$, then $(x_{s2}, a_2) = (0.6551, 0.0928)$ and trinomial (A.3.1) has two positive real roots, so (x_{s2}, a_2) is an unstable node). □

Appendix B

Proof Of The Level Set Equation (3.3.10)

B.1 Active Contours (Snakes)

Equation (3.3.10) is derived from the classical model of active contours, also known as snakes. We will mention the basic characteristics of this model. Active contours constitute a commonly employed solution in the field of 2D image segmentation and shape retrieval. A snake is a parameterized curve evolving on the basis of image features and internal constraints. Its description can be given as a function

$$C : U \to \mathbb{R}^2$$

where $U \subset \mathbb{R}$ (e.g. $U = [0, 1]$) and $s \in U$, so we have that $C(s) = (x(s), y(s))$, where $x(s), y(s)$ are the coordinates along the contour. The evolution equation for snakes can be derived from the minimization of an energy functional

$$E_{snake}(C) = E_{smooth}(C) + E_{image}(C) \tag{B.1.1}$$

where

$$E_{smooth}(C) = \int_0^1 [w_1|C_s|^2 + w_2|C_{ss}|^2]ds \tag{B.1.2}$$

is internal deformation energy (the first term forces the snake to be continuous by minimizing the distance among its points, while the second term produces a smoothing effect by cutting off large values of curvature), and

$$E_{image}(C) = \int_0^1 w_3 P(C)ds \tag{B.1.3}$$

is driving energy, whose role is to attract the contour to the under detection item. $P(x)$ is a scalar potential function taking into account image intensity $I(x)$ (e.g. $P(x) = -|\nabla I(x)|$). So, E_{image} becomes very small when the active contour reaches near the edge that we want to detect. w_1, w_2, w_3 are constants.

In order to minimize the functional $E(C)$, the active contour $C(s)$ must satisfy the Euler-Lagrange equation. This equation is a fundamental result of calculus of variations and is derived as follows: Consider the following functional

$$J = \int_{\Omega} F\left(x_1, \ldots, x_n, y, \frac{\partial y}{\partial x_1}, \ldots, \frac{\partial y}{\partial x_n}\right) dx_1 \ldots dx_n,$$

where Ω is a $n-$dimensional domain. Suppose that J has to be minimized (maximized) over a set of admissible functions y with fixed boundary conditions $y|_{\partial\Omega} = \bar{y}$. Assume that y is piecewise C^1 on Ω. Then J has an extremum in y only if the Euler-Lagrange equation is satisfied

$$\frac{\partial F}{\partial y} - \sum_{j=1}^{n} \frac{\partial}{\partial x_j}\left(\frac{\partial F}{\partial p_j}\right) = 0,$$

where F is in the form $F\left(x_1, \ldots, x_n, y, p_1, \ldots, p_n\right)$ and $p_j = \frac{\partial y}{\partial x_j}$. For the proof of this, see the Appendix B of [4]. The generalization of the Euler-Lagrange equation to the cases in which function F depends on higher-order derivatives (up to the $m-$th order) takes the following form

$$\frac{\partial F}{\partial y} + \sum_{i=1}^{m}\sum_{j=1}^{n}\left[(-1)^i \frac{\partial^i}{\partial {x_j}^i}\left(\frac{\partial F}{\partial {p^{(i)}}_j}\right)\right] = 0, \tag{B.1.4}$$

where ${p^{(i)}}_j = \frac{\partial^i y}{\partial {x_j}^i}$. So, a necessary condition for the minimization of $E(C)$ in (B.1.1) is, according to (B.1.4) (here we have $J(C) = \int_0^1 F(s, C, C_s, C_{ss})ds$, where $F(s, C, C_s, C_{ss}) = w_1|C_s|^2 + w_2|C_{ss}|^2 + w_3 P(C)$), the following:

$$\begin{aligned}
& \frac{\partial F}{\partial C} - \frac{\partial}{\partial s}\left(\frac{\partial F}{\partial (C_s)}\right) + \frac{\partial^2}{\partial s^2}\left(\frac{\partial F}{\partial (C_{ss})}\right) = 0 \\
\Rightarrow \quad & w_3 \nabla P(C) - \frac{\partial}{\partial s}\left(2w_1|C_s|\frac{C_s}{|C_s|}\right) + \frac{\partial^2}{\partial s^2}\left(2w_2|C_{ss}|\frac{C_{ss}}{|C_{ss}|}\right) = 0 \\
\Rightarrow \quad & -2w_1\frac{\partial C_s}{\partial_s} + 2w_2\frac{\partial^2 C_{ss}}{\partial s^2} + w_3\nabla P(C) = 0.
\end{aligned} \tag{B.1.5}$$

Instead of using an energy gradient descent algorithm to find a configuration which minimizes E_{snake}, it is possible to adopt the equivalent strategy of making the snake evolve in time toward a configuration (from now on C also depends on time t), satisfying the Euler-Lagrange equation. So, the following evolution equation results:

$$\frac{\partial C}{\partial t} = 2w_1 C_{ss} - 2w_2 C_{ssss} - w_3 \nabla P(C). \tag{B.1.6}$$

This means that, whenever the Euler-Lagrange equation is satisfied, the active contour is in a steady state ($C_t = 0$). It is worth to note that if we consider only the energy term $E_{image}(C)$ in (B.1.1), the associated Euler-Lagrange equation states that the snake stops on stationary points of the scalar field $P(x)$ (i.e. on the possible local extremum points of $P(x)$). We now consider a special class of active contour models in which the coefficient

related to the smoothing term (the one connected with the curvature) is equal to zero ($w_2 = 0$). This selection is motivated by two facts: Firstly, it allows us to connect these energy-based active contours with the level set equations, which is our next goal. Secondly, the smoothing result in active contours comes from curve flows based on curvature, which result only from the other terms of equation (B.1.1). So, the smoothing of the curve will take place even if $w_2 = 0$. Taking into account only the first term of E_{smooth}, (B.1.6) becomes

$$\frac{\partial C}{\partial t} = 2w_1 C_{ss} - w_3 \nabla P(C). \tag{B.1.7}$$

Since in 2D any closed curve shrinking under the effect of its curvature evolves into a circle before collapsing into one point, snakes are usually initialized as closed lines surrounding regions of interest. They then move by shrinking until driving energy makes them approach and stop on desired features. Depending on problem requirements, snakes can also be initialized as small circles located inside the areas of interest and inflated until image features are encountered (this strategy is more popular in blood vessel modeling).

B.2 Balloons

The 3D counterparts of snakes are commonly known as balloons, which are parametric deformable surfaces which can be represented as

$$S : U \times U \to \mathbb{R}^3$$

where $U \subset \mathbb{R}$, so $S(r, s) = (x(r, s), y(r, s), z(r, s))$. We will also assume that this surface parametrization is orthonormal, so we have

$$|S_r| = |S_s| = 1,$$

$$S_r \cdot S_s = 0.$$

In 3D, conversely to 2D case, it is not true that a surface shrinking under the effect of its curvature always evolves into a sphere before collapsing into one point. The lack of such a result on the regularity of surface evolution under curvature makes it usually more convenient to inflate the 3D surface making use of an internal pressure term rather than making it shrink under curvature. This approach is also convenient for 3D initialization, since it only requires the specification of the center and the radius of a sphere located inside the 3D object to reconstruct.

The corresponding (to the 2D case) energy functional in the 3D case is

$$\begin{aligned} E(S) &= \int_\Omega \left[\alpha_1 \left| \frac{\partial S}{\partial r} \right|^2 + \alpha_2 \left| \frac{\partial S}{\partial s} \right|^2 + 2\alpha_3 \left| \frac{\partial^2 S}{\partial r \partial s} \right|^2 \right] dr ds \\ &+ \int_\Omega \left[\alpha_4 \left| \frac{\partial^2 S}{\partial r^2} \right|^2 + \alpha_5 \left| \frac{\partial^2 S}{\partial s^2} \right|^2 + \alpha_6 P(S) \right] dr ds, \end{aligned}$$

where $P := -||\nabla G_s * I||^2$ and α_i, $1 \le i \le 6$, are constants. Setting the coefficients of the first derivatives of $E(S)$ equal to the term $g(x) = \frac{1}{1+\lambda|\nabla G_s * I(x)|^2}$ (which is the inflation

(deflation) speed and is used as the final stopping criterion of the active contours, where $\lambda > 0$ is a constant), setting the coefficients of the second derivatives equal to zero (similar to the 2D case, where we put $w_2 = 0$) and, finally, setting $\alpha_6 = 1$, $E(S)$ becomes

$$E(S) = \int_\Omega \left[g|S_r|^2 + g|S_s|^2 + P(S) \right] drds. \tag{B.2.1}$$

From (B.1.4) we have that, a necessary condition for the minimization of $E(S)$ in (B.2.1) (here $J(S) = \int_\Omega G(s, r, S, S_r, S_s)drds$, with $G(s, r, S, S_r, S_s) = g|S_r|^2 + g|S_s|^2 + P(S)$) is the following:

$$\begin{aligned}
& \frac{\partial G}{\partial S} - \frac{\partial}{\partial r}\left(\frac{\partial G}{\partial\left(\frac{\partial S}{\partial r}\right)}\right) - \frac{\partial}{\partial s}\left(\frac{\partial G}{\partial\left(\frac{\partial S}{\partial s}\right)}\right) = 0 \\
\Rightarrow \quad & \nabla P(S) - \frac{\partial}{\partial r}\left(2g|S_r|\frac{S_r}{|S_r|}\right) - \frac{\partial}{\partial s}\left(2g|S_s|\frac{S_s}{|S_s|}\right) = 0 \\
\Rightarrow \quad & \nabla P(S) - 2g(S_{rr} + S_{ss}) = 0.
\end{aligned}$$

So, similar to the two-dimensional case, assuming from now on that S also depends on time t, we take the corresponding evolution equation:

$$\frac{\partial S}{\partial t} = 2g(S_{rr} + S_{ss}) - \nabla P(S). \tag{B.2.2}$$

B.3 The Level Set Equation

A surface evolving in time, $S : \mathbb{R}^2 \times \mathbb{R}^+ \to \mathbb{R}^3$, can be represented as the λ level set of a time-dependent scalar function $F : \mathbb{R}^3 \times \mathbb{R}^+ \to \mathbb{R}$, so that

$$S(t) = \{x | F(x, t) = \lambda\}.$$

Since S remains the λ level set of F over time, we have that $F(S(t), t) = \lambda$, so

$$\begin{aligned}
& \frac{dF(S(t), t)}{dt} = 0 \\
\Rightarrow \quad & \frac{\partial F}{\partial S} \cdot \frac{\partial S}{\partial t} + \frac{\partial F}{\partial t} = 0 \\
\Rightarrow \quad & \frac{\partial F(S, t)}{\partial t} = -\nabla F(S, t) \cdot \frac{\partial S}{\partial t} \\
\Rightarrow \quad & \frac{\partial F(S, t)}{\partial t} = -|\nabla F(S, t)| \cdot \frac{\partial S}{\partial t} \cdot N
\end{aligned} \tag{B.3.1}$$

where $N = \frac{\nabla F}{|\nabla F|}$ is the outward normal to level sets, supposing that the embedding function has lower values inside and higher values outside the model. F, here, is a 4D function and S is its 3D level set. From (B.3.1) using (B.2.2) we have

$$\frac{\partial F(S, t)}{\partial t} = -|\nabla F(S, t)| 2g(S_{rr} + S_{ss})N + |\nabla F(S, t)| \nabla P(S) \cdot N. \tag{B.3.2}$$

So, the last step required to prove the level set equation (3.3.10) is to express the terms of the right-hand side of equation (B.2.2) in terms of differential expression $F(x,t)$. We have $F(S(r,s,t),t) = \lambda$, so $\frac{\partial F}{\partial r} = \nabla F(S,t) \cdot S_r = 0$ and

$$\frac{\partial^2 F}{\partial r^2} = [H_F(x) \cdot S_r] \cdot S_r + \nabla F \cdot S_{rr} = F_{uu} + \nabla F \cdot S_{rr} = 0, \tag{B.3.3}$$

where $H_F(x)$ is the Hessian matrix of F and F_{uu} is the second directional derivative of F in direction S_r. The same expression can be written for $\frac{\partial^2 F}{\partial s^2}$, so similarly we have

$$\frac{\partial^2 F}{\partial s^2} = [H_F(x) \cdot S_s] \cdot S_s + \nabla F \cdot S_{ss} = F_{vv} + \nabla F \cdot S_{ss} = 0, \tag{B.3.4}$$

where F_{vv} is the second directional derivative of F in direction S_s. So,

$$\begin{aligned} |\nabla F| 2g(S_{rr} + S_{ss})N &= |\nabla F| 2g(S_{rr} + S_{ss}) \cdot \frac{\nabla F}{|\nabla F|} \\ &= -2g(F_{uu} + F_{vv}) \end{aligned} \tag{B.3.5}$$

using (B.3.3) and (B.3.4). We assumed surface parametrization to be orthonormal, so $S_r \cdot S_s = 0$. We have created a correspondence of S_r and S_s with u and v, respectively. So, x, y, z is a generic orthonormal reference frame and u, v, w is the reference frame relative to the plane tangent to the level sets of surface S (S_r and S_s are both vectors tangent to S). F_w is also the directional derivative in the direction of w, which is the direction of $N = \frac{\nabla F}{|\nabla F|}$, so

$$F_w = \nabla F \cdot \frac{\nabla F}{|\nabla F|} = \frac{|\nabla F|^2}{|\nabla F|} = |\nabla F|. \tag{B.3.6}$$

In addition, in the reference frame u, v, w we have $N = (0,0,1)$, so, in this frame,

$$\nabla F_w \cdot N = (F_{wu}, F_{wv}, F_{ww}) \cdot (0,0,1) = F_{ww}. \tag{B.3.7}$$

So, using the definition of mean curvature H, we have:

$$\begin{aligned} H(x) &= \nabla \cdot \left(\frac{\nabla F}{|\nabla F|} \right) = div \left(\frac{\nabla F}{|\nabla F|} \right) = \frac{1}{|\nabla F|} div(\nabla F) + \nabla F \cdot \nabla \left(\frac{1}{|\nabla F|} \right) \\ &= \frac{F_{xx} + F_{yy} + F_{zz}}{|\nabla F|} + \nabla F \cdot \left(-\frac{\nabla (|\nabla F|)}{|\nabla F|^2} \right) \\ &= \frac{(F_{xx} + F_{yy} + F_{zz})|\nabla F| - \nabla F \cdot \nabla (|\nabla F|)}{|\nabla F|^2} \\ &\overset{(B.3.6)}{=} \frac{(F_{xx} + F_{yy} + F_{zz})|\nabla F| - (|\nabla F| \cdot N) \cdot \nabla F_w}{|\nabla F|^2} \\ &= \frac{(F_{xx} + F_{yy} + F_{zz})|\nabla F| - (\nabla F_w \cdot N) \cdot |\nabla F|}{|\nabla F|^2} \\ &\overset{(B.3.7)}{=} \frac{\nabla(\nabla F) - F_{ww}}{|\nabla F|} = \frac{F_{uu} + F_{vv} + F_{ww} - F_{ww}}{|\nabla F|} \\ &= \frac{1}{|\nabla F|}(F_{uu} + F_{vv}). \end{aligned} \tag{B.3.8}$$

The pre-last equality in (B.3.8) is explained by the fact that $H(x)$ can be computed from the second order differential structure of F, $H = div\left(\frac{\nabla F}{|\nabla F|}\right)$, regardless of the particular coordinate system adopted (coordinate system u, v, w is used in this equality). From (B.3.5) using (B.3.8) we have:

$$|\nabla F| 2g(S_{rr} + S_{ss})N = -2gH|\nabla F|. \tag{B.3.9}$$

We also have

$$|\nabla F|\nabla P(x)N = \nabla P(x)\nabla F. \tag{B.3.10}$$

So, (B.3.2) due to (B.3.9) and (B.3.10) becomes

$$\begin{aligned} & \frac{\partial F(x,t)}{\partial t} = 2gH|\nabla F| + \nabla P(x)\nabla F \\ \Rightarrow \quad & \frac{\partial F(x,t)}{\partial t} = g(x)K|\nabla F| + \nabla F \cdot \nabla P, \end{aligned} \tag{B.3.11}$$

where K is twice the mean curvature. We can add an extra parameter in the above equation, aiming at the inflation of the balloon (the initial balloon is deflated in (B.3.11)) and to increase the convergence speed. This occurs in (B.1.1) if we add another term, E_{infl}, which is connected with the inflation, driven by the image intensity. So, (B.1.1) becomes

$$E_{balloon}(S) = E_{infl}(S) + E_{smooth}(S) + E_{image}(S). \tag{B.3.12}$$

Then, a new velocity is added to the movement of the level sets of S, which has vertical direction to S (the direction of N). This velocity is $cg(S)N$, so term $cg(S)N$ is added to the right-hand side of evolution equation (B.2.2), where $c > 0$ is a constant and g is a weight of this term, too. From this we have that term $-|\nabla F(S,t)|cg(S)N \cdot N = -cg(S)|\nabla F|$ is added to (B.3.2) and this is the term which is finally added to the right-hand side of (B.3.11) to get equation

$$\frac{\partial F(x,t)}{\partial t} = g(x)(K - c)|\nabla F| + \nabla F \cdot \nabla P. \tag{B.3.13}$$

This is the level set equation (3.3.10) we used in our work, with a slightly different notation (in (3.3.10) we have ϕ instead of F, g_I instead of g and κ instead of K).

As mentioned in Sec. 3.3.2.1, similar proofs with the above can be found in [49] and [4]. The main difference compared with them is the different term g that we have chosen, to provide greater weight to the image intensity gradient (by adopting parameter $\lambda > 0$ and by taking the square of term $|\nabla G_s * I|$).

Appendix C

The Results Of The Ten Patient Data Sets

C.1 Detailed Results For The Outer Wall And For The Wall Thickness

Tables C.1 and C.2 present the results for each of the ten data sets for all the quantities used for evaluating the outer wall boundary segmentation error (Sec. 3.5.4). AAE, RAE, MEDIS, HADIS and AO are given as M±s.d.(min,max), where M is the mean over the slices of each data set. The last four rows of these two Tables for these quantities, which are the results presented in Table 3.1, refer to the ten M's.

Tables C.3 and C.4 include the results for the wall thickness, which is used as evaluation of the thrombus boundary segmentation error. All the quantities used for this purpose (Sec. 3.5.5) are presented for the ten data sets we used, taking $\phi = \frac{\pi}{60}$ (24 sectors of angle $\frac{\pi}{12}$). AESWT, AUTSWT and MANSWT are given as M±s.d.(min,max), where M is the mean over the slices of each data set. The last four rows of Tables C.3 and C.4 for these quantities, which are the results presented in Table 3.2, refer to the ten M's.

Table C.1: Results for the outer wall for the ten patient data sets. AAE and RAE are given as mean±s.d.(min,max).

Patient No.	No. of slices	AAE (cm^2)	RAE (%)	AVE (cm^3)	RVE (%)
1	47	$0.916 \pm 0.503(0.013, 2.203)$	$7.1 \pm 4.6(0.2, 16.8)$	7.079	4.8
2	43	$0.654 \pm 0.224(0.193, 1.024)$	$13.1 \pm 5.4(3.1, 25.9)$	4.230	12.4
3	41	$1.079 \pm 0.739(0.007, 2.821)$	$4.0 \pm 3.1(0.0, 11.6)$	4.336	2.4
4	29	$0.784 \pm 0.550(0.045, 1.992)$	$4.5 \pm 2.9(0.3, 10.3)$	1.844	2.5
5	56	$1.606 \pm 1.024(0.126, 4.820)$	$4.4 \pm 2.9(0.3, 11.6)$	5.211	1.6
6	44	$1.505 \pm 0.964(0.039, 4.226)$	$4.5 \pm 2.8(0.1, 11.3)$	6.344	4.3
7	45	$1.729 \pm 1.338(0.010, 5.887)$	$4.5 \pm 3.4(0.0, 13.0)$	5.192	1.9
8	42	$1.060 \pm 0.571(0.019, 2.162)$	$10.2 \pm 6.7(0.1, 29.8)$	6.028	8.3
9	52	$1.037 \pm 0.712(0.001, 3.422)$	$2.5 \pm 1.7(0.0, 7.8)$	5.129	1.6
10	51	$1.096 \pm 0.790(0.006, 2.876)$	$5.2 \pm 3.5(0.0, 12.3)$	0.237	0.3
mean	45	1.147	6.0	4.563	4.0
s.d.	7	0.355	3.3	2.083	3.7
min	29	0.654	2.5	0.237	0.3
max	56	1.729	13.1	7.079	12.4

Table C.2: Results for the outer wall for the ten patient data sets. MEDIS, HADIS and AO are given as mean±s.d.(min,max).

Patient No.	No. of slices	MEDIS (mm)	HADIS (mm)	AO (%)
1	47	$1.005 \pm 0.281(0.477, 1.600)$	$2.944 \pm 1.024(1.535, 6.037)$	$95.0 \pm 1.8(90.8, 97.9)$
2	43	$0.978 \pm 0.252(0.539, 1.565)$	$2.656 \pm 0.829(1.303, 5.089)$	$91.8 \pm 2.6(85.1, 95.8)$
3	41	$1.104 \pm 0.292(0.602, 1.943)$	$3.778 \pm 1.318(1.542, 6.966)$	$96.3 \pm 1.1(93.6, 97.8)$
4	29	$1.429 \pm 0.349(0.740, 2.206)$	$4.268 \pm 1.143(2.137, 6.736)$	$93.7 \pm 1.4(90.8, 96.9)$
5	56	$1.488 \pm 0.353(0.910, 2.561)$	$5.156 \pm 1.468(2.884, 8.192)$	$95.7 \pm 1.2(92.4, 97.6)$
6	44	$1.110 \pm 0.265(0.638, 2.010)$	$4.285 \pm 1.439(1.999, 7.455)$	$96.5 \pm 0.8(94.0, 97.9)$
7	45	$1.910 \pm 0.529(0.931, 3.263)$	$5.999 \pm 1.674(3.100, 9.681)$	$94.5 \pm 1.6(90.2, 97.6)$
8	42	$1.354 \pm 0.353(0.634, 2.323)$	$3.369 \pm 0.693(2.100, 5.615)$	$92.3 \pm 3.3(81.7, 96.9)$
9	52	$1.101 \pm 0.253(0.623, 1.603)$	$3.689 \pm 0.906(2.050, 5.869)$	$97.0 \pm 0.8(94.7, 98.2)$
10	51	$1.726 \pm 0.456(0.635, 2.785)$	$5.455 \pm 1.418(2.588, 8.811)$	$93.2 \pm 1.6(89.5, 96.9)$
mean	45	1.320	4.160	94.6
s.d.	7	0.318	1.096	1.8
min	29	0.978	2.656	91.8
max	56	1.910	5.999	97.0

Table C.3: Results for the wall thickness for the ten patient data sets. AESWT, AUTSWT and MANSWT are given as mean±s.d.(min,max). Angle $\phi = \frac{\pi}{60}$.

Patient No.	No. of slices	AESWT (mm)	AUTSWT (mm)	MANSWT (mm)
1	47	$0.869 \pm 0.779(0.001, 8.636)$	$2.759 \pm 1.569(0.500, 13.181)$	$2.900 \pm 1.246(0.129, 12.141)$
2	43	$0.940 \pm 0.691(0.002, 6.172)$	$2.121 \pm 0.684(1.157, 5.968)$	$2.928 \pm 0.963(0.312, 9.827)$
3	41	$1.289 \pm 1.023(0.005, 7.030)$	$2.919 \pm 1.296(0.872, 10.131)$	$3.607 \pm 1.014(0.465, 7.948)$
4	29	$0.833 \pm 0.736(0.000, 5.523)$	$2.433 \pm 0.886(1.159, 7.917)$	$2.416 \pm 0.703(0.228, 6.112)$
5	56	$1.365 \pm 1.234(0.005, 8.813)$	$2.940 \pm 1.700(0.251, 11.721)$	$2.921 \pm 0.916(0.218, 9.832)$
6	44	$1.314 \pm 0.981(0.001, 7.051)$	$2.642 \pm 0.955(1.240, 8.845)$	$3.695 \pm 1.128(0.432, 9.103)$
7	45	$1.683 \pm 1.236(0.001, 9.961)$	$2.699 \pm 1.213(1.188, 14.302)$	$3.814 \pm 1.306(0.260, 8.516)$
8	42	$0.742 \pm 0.640(0.001, 6.199)$	$1.992 \pm 0.757(0.799, 8.483)$	$2.192 \pm 0.671(0.225, 4.256)$
9	52	$1.077 \pm 0.808(0.001, 5.497)$	$2.116 \pm 0.863(0.997, 7.495)$	$2.752 \pm 0.882(0.239, 6.436)$
10	51	$1.159 \pm 1.161(0.002, 8.601)$	$3.129 \pm 1.423(1.244, 10.769)$	$2.707 \pm 0.682(0.771, 5.712)$
mean	45	1.127	2.575	2.993
s.d.	7	0.292	0.393	0.545
min	29	0.742	1.992	2.192
max	56	1.683	3.129	3.814

Table C.4: Results for the wall thickness (AEMSWT and REMSWT) for the ten patient data sets. Angle $\phi = \frac{\pi}{60}$.

Patient No.	No. of slices	AEMSWT (mm)	REMSWT (%)
1	47	0.141	4.87
2	43	0.806	27.55
3	41	0.688	19.08
4	29	0.017	0.70
5	56	0.019	0.66
6	44	1.053	28.50
7	45	1.115	29.23
8	42	0.201	9.15
9	52	0.637	23.14
10	51	0.422	15.57
mean	45	0.510	15.84
s.d.	7	0.411	11.38
min	29	0.017	0.66
max	56	1.115	29.23

Appendix D

Details About The Software Created For The Methods Of The Third Chapter

D.1 A Short Description Of The Software

A brief manual for the software created in Matlab, which incorporates all the methods introduced in the third Chapter of this thesis, will now be given. The only input is a 3D array with the image intensity values of the 3D AAA image data set. This array is extracted from the DICOM images with "loaddcm(loaddcmdir)" command of Matlab 7.0.1 service pack 1 (other versions of Matlab present a problem with this convertion). The output contains the points of the lumen, thrombus and outer wall (for all three stopping criteria) boundaries for the 2D cross section chosen, as well as the leakage region if there is a leakage.

In the beginning, the 3D data set can be visualized with "orthogonalslicer" to select either the volume of interest, if we want to create a 3D reconstruction from the 2D results, or just a cross section. A suitable cropping of the 2D image can then be made (with "imcrop" command) either interactively or manually, to extract the region of interest and reduce segmentation time. The FMM is then applied using "Fast Marching Toolbox" [47] created by Gabriel Peyré. The user can interactively enter up to four points of starting and ending points to extract an optimized initialization for the lumen or for the thrombus-outer wall segmentations. Detailed instructions for providing the proper points are shown and the initialization is the union of the results extracted from each pair of points. Before proceeding to the LSM, the initialization is visualized on the selected image and, if it is not a proper one, the possibility of repeating the FMM is provided.

For the LSM, the "Level Set Toolbox" [59] created by Baris Sumengen is used (and more specifically, routine "evolve2D"). Input for the LSM are the input level set function ϕ (whose zero level set is the initialization from the FMM), the resolution of the grid, a constant for calculating the euler step (dt), the number of iterations, the scheme for calculating the derivative of ϕ and the components of the LSM equation (force in the

normal direction, vector field and curvature). The level set function is reinitialized into a signed distance function while preserving the zero level set, every few iterations (with "reinitSD" routine).

For the lumen, 100 iterations are sufficient and, after visualizing the result, the possibility of obtaining a smoother and more exact result is provided: the LSM with curvature only or with all its components, in an outward or inward fashion, can be applied for a few iterations (this possibility is provided every time the LSM is applied for the thrombus and outer wall boundaries, too). For the thrombus boundary, the thrombus boundary reconstruction method (see the code in the next section) is applied after the LSM. Possibilities of detecting the possible leakage region (with the DLR method) and of choosing one (or all three) of the stopping criteria are then provided. Leakage region is then shown in red and the detection of the outer wall boundary using the LSM to the thrombus initialization and the chosen stopping criterion begins. The LSM result is then visualized and the outer wall boundary reconstruction method follows. The possibility of leaving some steps of this method out is provided, based on the frequently visualized result. Finally, the image is shown with all three boundaries extracted, but if thrombus and outer wall boundaries coincide or are too close to each other in some regions, the TWBD method for the thrombus boundary is applied. The final three boundaries are then shown in one to three figures, depending on the number of the stopping criteria chosen.

D.2 Matlab Code For The Thrombus Boundary Reconstruction Method

The Matlab code for the method used to reconstruct the thrombus boundary in the presence of calcifications (Sec. 3.4.1) is presented below. This is only a very small sample of the codes written for applying the methods described in this thesis, as it would be impossible to include them all here. Comments for each part of this code are included inside.

```
% CODE FOR THE THROMBUS BOUNDARY RECONSTRUCTION

% INPUT :
% z: the intensity of the cropped image (nxn array)
% S_thrombou: the thrombus initialization obtained by the FMM (nxn array)


% OUTPUT :
% cont_tel2: the thrombus boundary after applying the thrombus boundary
% reconstruction method, described in Sec. 3.4.1.

disp('THE THROMBUS BOUNDARY RECONSTRUCTION HAS NOW BEGUN')

tic;

phi2=S_thrombou;

```

```
% External vector field
a=fspecial('gaussian',[5 5],1);
[w,q]=gradient(a);
s=double(z);
f1=imfilter(s,w);
f2=imfilter(s,q);

P=sqrt(f1.^2+f2.^2);

[u,v]=gradient(P);
%u is the x component of the vector field
%v is the y component of the vector field

% b: weighting for curvature-based force. b needs to be positive

gI_me_fft2=1./(1+0.1*(f1.^2+f2.^2));

b = 2*gI_me_fft2;

% Vn: force in the normal direction
Vn = 5000.*gI_me_fft2;

dx=1;
dy=1;

% Evolution using bwdist for reinitialization every "iter" iterations
% for 200 iterations. "sum_iter" has the same value with iter
% (sum_iter<=200). The "Level Set Toolbox" created by Baris Sumengen and,
% more specifically, its routine "evolve2D" is used for the LSM

iter=10;
sum_iter=10;
while sum_iter<=200
phi2 = double((phi2 > 0).*(bwdist(phi2 < 0)-0.5) - (phi2 < 0).* ...
      (bwdist(phi2 >0)-0.5));
%phi2= reinit_SD(phi2, dx, dy, 0.5, 'WENO', 200);
phi2 = evolve2D(phi2,dx,dy,0.5,iter,'ENO3',1,1,Vn,1,u,v,1,b);
clear ARITHMOS_EPANALHPSEWN
ARITHMOS_EPANALHPSEWN=sprintf('%i ITERATIONS UNTIL NOW',sum_iter)
sum_iter=sum_iter+iter;
end

% "cont2" is the zero level set of "phi2", i.e. the resulting curve
% after the LSM
clear cont2
cont2=contour(phi2,[0 0],'b');
close all

clear tam
tamhden=1;
for i=1:length(cont2)
    if (cont2(1,i)==0)
     tam(tamhden)=cont2(2,i);
     tamhden=tamhden+1;
```

```
    end
end

for i=1:length(cont2)
    if (cont2(1,i)==0) && (cont2(2,i)==max(tam))
        j=i;
        break
    end
end

for k=1:2
    for i=j+1:length(cont2)
        if (cont2(1,i)≠0)
            cont_help(k,i-j)=cont2(k,i);
        else
            break
        end
    end
end

disp('THROMBUS IS IN FIGURE 1')
    imshow(mat2gray(z))
    hold on;
    plot(cont_help(1,:),cont_help(2,:),'b')
    display('If thrombus has entered regions between the calcifications,')
    asbest=input('press 1. If not, press 2: \n');

while (asbest≠1) && (asbest≠2)
       asbest=input('Wrong number, please repeat:\n');
end

if (asbest==1)
close all
disp('CORRECTION OF THROMBUS BOUNDARY HAS NOW BEGUN')

% Routine "polycenter" provides the centroid of cont_help

i=1:length(cont_help);
[AREA,CX,CY] = polycenter(cont_help(1,i),cont_help(2,i));
kentro(1)=CX;
kentro(2)=CY;

% Function "antistrofh" is used to obtain the image of the curve
% under the inversion mapping with respect to its centroid

for i=1:1:length(cont_help)
    [xant(i),yant(i)]=antistrofh(cont_help(1,i),cont_help(2,i), ...
        kentro(1),kentro(2));
end

%figure
%i=1:length(xant);
%plot(xant(i),yant(i),'g')
%hold
```

```
126
127 % The boundary of the convex hull of the inversion mapping of the curve
128 % is found using "convhull"
129 dkir=convhull(xant(:),yant(:));
130 kir=[xant(dkir);yant(dkir)];
131
132 %i=1:length(kir);
133 %plot(kir(1,i),kir(2,i),'b')
134
135 % The preimages of the points of the convex hull under the inversion
136 % mapping form a domain, whose boundary is "thromb"
137
138 thromb=[cont_help(1,dkir);cont_help(2,dkir)];
139
140 %i=1:length(thromb);
141 %plot(thromb(1,i),thromb(2,i),'g')
142
143 % TECHNIQUES FOR SMOOTHNESS OR FOR A MORE ACCURATE RESULT:
144 disp('THROMBUS IS IN FIGURE 1')
145     imshow(mat2gray(z))
146     hold on;
147     plot(thromb(1,:),thromb(2,:),'b')
148 end
149 if (asbest==2)
150     thromb=cont_help;
151 end
152 display('For smoothing with curvature-only evolution, press 1.')
153 display('For a smoother and more accurate result applying the LSM,')
154 display('press 2 for an outward direction, or press 3 for inward.')
155 texn=input('For nothing of the above, press 0:  \n');
156 while (texn≠0) && (texn≠1) && (texn≠2) && (texn≠3)
157 texn=input('Wrong number, please provide the correct one:\n');
158 end
159
160 if (texn==0)
161     cont_tel2=thromb;
162     close all
163 end
164 if (texn==1) || (texn==2) || (texn==3)
165 iteromal=input('Provide the number of iterations (around 20-40)\n');
166
167 close all
168 clear pts testpts xy in ff inn ww phi2
169
170 % The thrombus boundary result up to now must be placed as the
171 % initialization of the LSM:
172 k=0;
173 for i=1:1:siz(2)
174     for j=1:1:siz(1)
175         pts(siz(1).*k+j,1)=i;
176         pts(siz(1).*k+j,2)=j;
177     end
178     k=k+1;
179 end
```

```
testpts=pts;
xy=thromb';
in=inpoly(testpts,xy);
ff=1;
for i=1:1:length(in)
    if (in(i)==1)
        inn(ff)=i;
        ff=ff+1;
    end
end
for i=1:1:length(inn)
    if (mod(inn(i),siz(1))≠0)
        ww(i,1)=fix(inn(i)/siz(1))+1;
        ww(i,2)=mod(inn(i),siz(1));
    elseif (mod(inn(i),siz(1))==0)
        ww(i,1)=inn(i)/siz(1);
        ww(i,2)=siz(1);
    end
end
clear phi2
phi2=ones(siz(1),siz(2));

for j=1:1:length(ww)
    phi2(ww(j,2),ww(j,1))=-1;
end

% Evolution with curvature-only, for a few iterations
if(texn==1)

b = 0.3*ones(siz(1), siz(2));

dx=1;
dy=1;

phi2 = evolve2D(phi2,dx,dy,0.5,50,[],[],0,[],0,[],[],1,b);

cont_help2=contour(phi2,[0 0],'b');
close all

clear tam
tamhden=1;
for i=1:length(cont_help2)
    if (cont_help2(1,i)==0)
     tam(tamhden)=cont_help2(2,i);
     tamhden=tamhden+1;
    end
end

for i=1:length(cont_help2)
    if (cont_help2(1,i)==0) && (cont_help2(2,i)==max(tam))
        j=i;
        break
    end
end
```

```
234
235 for k=1:2
236     for i=j+1:length(cont_help2)
237         if (cont_help2(1,i)≠0)
238             cont_tel2(k,i-j)=cont_help2(k,i);
239         else
240             break
241         end
242     end
243 end
244
245
246 elseif (texn==2)
247
248 % Evolution with LSM in an outward direction, for a few iterations
249
250 % Evolution using REINIT (another routine of the "Level Set Toolbox") for
251 % reinitialization every "iter" iterations for "iteromal" iterations.
252 % "sum_iter" has the same value with iter (sum_iter≤iteromal).
253
254 iter=10;
255 sum_iter=10;
256 disp('EVOLUTION WITH LSM IN AN OUTWARD DIRECTION, FOR A FEW ITERATIONS')
257 disp('TO GET A MORE ACCURATE RESULT (REINITIALIZATION EVERY 10)')
258 while sum_iter≤iteromal
259 phi2= reinit_SD(phi2, dx, dy, 0.5, 'WENO', 50);
260 phi2 = evolve2D(phi2,dx,dy,0.5,iter,'ENO3',1,1,Vn,1,u,v,1,b);
261 clear ARITHMOS_EPANALHPSEWN
262 ARITHMOS_EPANALHPSEWN=sprintf('%i ITERATIONS',sum_iter)
263 sum_iter=sum_iter+iter;
264 end
265 cont_help2=contour(phi2,[0 0],'b');
266 close all
267
268 clear tam
269 tamhden=1;
270 for i=1:length(cont_help2)
271     if (cont_help2(1,i)==0)
272      tam(tamhden)=cont_help2(2,i);
273      tamhden=tamhden+1;
274     end
275 end
276
277 for i=1:length(cont_help2)
278     if (cont_help2(1,i)==0) && (cont_help2(2,i)==max(tam))
279         j=i;
280         break
281     end
282 end
283
284 for k=1:2
285     for i=j+1:length(cont_help2)
286         if (cont_help2(1,i)≠0)
287             cont_tel2(k,i-j)=cont_help2(k,i);
```

```
        else
            break
        end
    end
end

elseif (texn==3)

% Evolution with LSM in an inward direction, for a few iterations

iter=10;
sum_iter=10;
disp('EVOLUTION WITH LSM IN AN INWARD DIRECTION, FOR A FEW ITERATIONS')
disp('TO GET A MORE ACCURATE RESULT (REINITIALIZATION EVERY 10)')
while sum_iter≤iteromal
phi2= reinit_SD(phi2, dx, dy, 0.5, 'WENO', 50);
phi2 = evolve2D(phi2,dx,dy,0.5,iter,'ENO3',1,1,-Vn,1,u,v,1,b);
clear ARITHMOS_EPANALHPSEWN
ARITHMOS_EPANALHPSEWN=sprintf('%i ITERATIONS',sum_iter)
sum_iter=sum_iter+iter;
end
cont_help2=contour(phi2,[0 0],'b');
close all
clear tam
tamhden=1;
for i=1:length(cont_help2)
    if (cont_help2(1,i)==0)
     tam(tamhden)=cont_help2(2,i);
     tamhden=tamhden+1;
    end
end

for i=1:length(cont_help2)
    if (cont_help2(1,i)==0) && (cont_help2(2,i)==max(tam))
        j=i;
        break
    end
end

for k=1:2
    for i=j+1:length(cont_help2)
        if (cont_help2(1,i)≠0)
            cont_tel2(k,i-j)=cont_help2(k,i);
        else
            break
        end
    end
end

end
end

    disp('THE THROMBUS BOUNDARY IS DEPICTED IN THIS FIGURE')
    imshow(mat2gray(z))
```

```
342     hold on;
343     plot(cont_tel2(1,:),cont_tel2(2,:),'blue')
344     disp('PRESS ANY KEY TO CONTINUE')
345     pause
346     close all
347
348 % Execution time for the thrombus boundary reconstruction
349 ethrombus_time=toc./60;
350 fprintf('THROMBUS TIME: %g MINUTES \n',ethrombus_time);
```

Bibliography

[1] M. D. Abramoff, P. J. Magelhaes, and S. J. Ram, *Image Processing with ImageJ*, Biophotonics International **11** (2004), no. 7, 36–42.

[2] L. Alvarez, F. Guichard, P. L. Lions, and J. M. Morel, *Axioms and fundamental equations of image processing*, Arch. Rat. Mech. Anal. **123** (1993), 199–257.

[3] L. Ambrosio, P. Cannarsa, and H. M. Soner, *On the propagation of singularities of semi-convex functions*, Annali Scu. norm. sup. Pisa **20** (1993), no. 4, 597–616.

[4] L. Antiga, *Patient-Specific Modelling of Geometry and Blood-Flow in Large Arteries*, Ph.D. thesis, Politecnico di Milano, 2003.

[5] M. Bardi and I. Capuzzo-Dolcetta, *Optimal Control and Viscosity Solutions of Hamilton-Jacobi-Bellman Equations*, Birkhäuser, Boston, 1997.

[6] O. Bodur, L. Grady, A. Stillman, G. Setser, R. Funka-Lea, and T. O'Donnell, *Semi-automatic aortic aneurysm analysis*, Medical Imaging 2007: Physiology, function and structure from medical images. Proceedings of SPIE-Int'l. Society for Optical Engineering **6511** (2007).

[7] A. Borghi, N. B. Wood, R. H. Mohiaddin, and X. Yun Xu, *3D geometric reconstruction of thoracic aortic aneurysms*, BioMedical Engineering OnLine 2006 **5** (2006), no. 59.

[8] P. Cannarsa and C. Sinestrari, *Semiconcave Functions, Hamilton-Jacobi Equations, and Optimal Control*, Progress in Nonlinear Differential Equations and Their Applications V. 58, Birkhäuser Boston Inc., Boston, MA, 2004.

[9] P. Cannarsa and H. M. Soner, *On the singularities of the viscosity solutions to Hamilton-Jacobi-Bellman equations*, Indiana Univ. Math. J. **36** (1987), no. 3, 501–524.

[10] I. Capuzzo-Dolcetta and P. L. Lions, *Viscosity solutions and applications (Montecatini, 1995)*, volume 1660 of Lecture Notes in Mathematics, Berlin, 1997. Springer.

[11] T. Cootes, C. Taylor, D. Cooper, and J. Graham, *Active shape models-their training and application*, Computer Vision and Image Understanding **61** (1995), no. 1, 38–59.

[12] M. G. Crandall, L. C. Evans, and P. L. Lions, *Some Properties of Viscosity Solutions of Hamilton-Jacobi Equations*, Trans. Amer. Math. Soc. **282** (1984), no. 2, 487–502.

[13] M. G. Crandall and P. L. Lions, *Condition d' unicité pour les solutions généralisées des équations de Hamilton-Jacobi du premier ordre*, C. R. Acad. Sci. Paris Sér. A-B **292** (1981), 183–186.

[14] ———, *Viscosity Solutions of Hamilton-Jacobi equations*, Trans. Amer. Math. Soc. **277** (1983), 1–42.

[15] M. de Bruijne, B. van Ginneken, W. Bartels, M. J. van der Laan, J. D. Blankensteijn, W. J. Niessen, and M. A. Viergever, *Automated segmentation of abdominal aortic aneurysms in multi-spectral MR images*, Medical Image Computing and Computer-Assisted Intervention, Lecture Notes in Computer Science, Springer **2879** (2003), 538–545.

[16] M. de Bruijne, B. van Ginneken, M. A. Viergever, and W. J. Niessen, *Interactive segmentation of abdominal aortic aneurysms in CTA images*, Med. Image Anal. **8** (2004), no. 2, 127–138.

[17] S. de Putter, M. Breeuwer, U. Kose, F. Laffargue, J. M. Rouet, R. Hoogeveen, H. van den Bosch, J. Buth, F. van de Vosse, and F. Gerritsen, *Automatic determination of the dynamic geometry of abdominal aortic aneurysm from MR with application to wall stress simulation*, International Congress Series **1281** (2005), 339–344.

[18] W. D. Dechert and S. I. O'Donnell, *The Stochastic Lake Game: A Numerical Solution*, Journal of Economic Dynamics and Control **30** (2006), no. 9-10, 1569–1587.

[19] E. DeGiorgi, A. Marino, and M. Tosques, *Problemi di evoluzione in spazi metrici e curve di massima pendenza*, Rend. Classe Sci. Fis. Mat. Nat. Accad. Naz. Lincei **68** (1980), 180–187.

[20] T. Deschamps, *Curve and Shape Extraction with Minimal Path and Level-Sets Technique. Applications to 3D Medical Imaging*, Ph.D. thesis, Université Paris-IX Dauphine, 2001.

[21] E. S. Di Martino, A. Bohra, J. P. Vande Geest, N. Gupta, M. S. Makaroun, and D. A. Vorp, *Biomechanical properties of ruptured versus electively repaired abdominal aortic aneurysm wall tissue*, J. Vasc. Surg. **43** (2006), no. 3, 570–576.

[22] L. C. Evans, *On solving certain nonlinear partial differential equations by accretive operator methods*, Israel J. Math. **36** (1981), 235–247.

[23] L. C. Evans and J. Spruck, *Motion of level sets by mean curvature I*, J. Differential Geometry **33** (1991), 635–681.

[24] ———, *Motion of level sets by mean curvature IV*, J. Geom. Anal. **5** (1995), 77–114.

[25] B. Güneralp and Y. Barlas, *Dynamic modelling of a shallow freshwater lake for ecological and economic sustainability*, Ecological Modelling **167** (2003), 115–138.

[26] A. Gelas, J. Schaerer, O. Bernard, D. Friboulet, P. Clarysse, I. E. Magnin, and R. Prost, *Radial Basis Functions Collocation Methods for Model Based Level-Set Segmentation*, IEEE International Conference on Image Processing **2** (2007), 237–240.

[27] S. Giordana, S. J. Sherwin, J. Peiro, D. J. Doorly, Y. Papaharilaou, C. G. Caro, N. Watkins, N. Cheshire, M. Jackson, C. Bicknall, and V. Zervas, *Automated classification of peripheral distal by-pass geometries reconstructed from medical data*, J. Biomech. **38** (2005), no. 1, 47–62.

[28] L. Grüne, M. Kato, and W. Semmler, *Solving Ecological Management Problems Using Dynamic Programming*, Journal of Economic Behavior & Organization **57** (2005), no. 4, 448–473.

[29] A. Henderson, *ParaView Guide, A Parallel Visualization Application*, Kitware Inc. (2007).

[30] R. Jensen and P. E. Souganidis, *A regularity result for viscosity solutions of Hamilton-Jacobi equations in one space dimension*, Trans. Amer. Math. Soc. **301** (1987), no. 1, 137–147.

[31] K. Kawaguchi, *Optimal Control of Pollution Accumulation with Long- Run Average Welfare*, Environmental and Resource Economics **26** (2003), no. 3, 457–468.

[32] G. Kossioris, Y. Papaharilaou, and C. Zohios, *Detection of Lumen, Thrombus and Outer Wall Boundaries of an Abdominal Aortic Aneurysm from 2D Medical Images Using Level Set Methods*, Proceedings of the ASME 2008 Summer Bioengineering Conference (SBC2008), June 25-29, Marriott Resort, Marco Island, Florida, USA, SBC2008-192804 (2008).

[33] G. Kossioris and C. Zohios, *The Value Function of the Shallow Lake Problem as a Viscosity Solution of a HJB Equation*, Quarterly of Applied Mathematics, to appear.

[34] C. Li, C. Xu, C. Gui, and M. D. Fox, *Level set evolution without re-initialization: a new variational formulation*, CVPR 2005 **1** (2005), 430–436.

[35] Z. Y. Li, J. U-King-Im, T. Y. Tang, E. Soh, T. C. See, and J. H. Gillard, *Impact of calcification and intraluminal thrombus on the computed wall stresses of abdominal aortic aneurysm*, J. Vasc. Surg. **47** (2008), no. 5, 928–935.

[36] J. S. Lindholt, *Aneurysmal wall calcification predicts natural history of small abdominal aortic aneurysms*, Atherosclerosis **197** (2008), no. 2, 673–678.

[37] P. L. Lions, *Generalized solutions of Hamilton-Jacobi equations*, Pitman, London, 1982.

[38] S. Loncaric, M. Subasic, and E. Sorantin, *3-D Deformable Model for Abdominal Aortic Aneurysm Segmentation from CT Images*, First Int'l Workshop on Image and Signal Processing and Analysis (2000), 139–144.

[39] Q. Long, X. Y. Xu, M. W. Collins, M. Bourne, and T. M. Griffith, *Magnetic resonance image processing and structured grid generation of a human abdominal bifurcation*, Computer Methods and Programs in Biomedicine **56** (1998), 249–259.

[40] D. Magee, A. Bulpitt, and E. Berry, *Combining 3D Deformable Models and Level Set Methods for the Segmentation of Abdominal Aortic Aneurysms*, Proceedings of the British Machine Vision Conference, the British Machine Vision Association (2001), 119–126.

[41] G. Martufi, E. S. Di Martino, C. H. Amon, S. C. Muluk, and E. A. Finol, *Three-Dimensional Geometrical Characterization of Abdominal Aortic Aneurysms: Image-Based Wall Thickness Distribution*, J. Biomech. Eng. **131** (2009), no. 6, 061015 (11 pages).

[42] K-G. Mäler, *Development, ecological resources and their management: A study of complex dynamic systems*, European Economic Review **44** (2000), 645–665.

[43] K-G. Mäler, A. Xepapadeas, and A. de Zeeuw, *The Economics of Shallow Lakes*, Environmental and Resource Economics **26** (2003), no. 4, 603–624.

[44] I. M. Mitchell, *The Flexible, Extensible and Efficient Toolbox of Level Set Methods*, Journal of Scientific Computing **35** (2008), no. 2-3, 300–329.

[45] S. D. Olabarriaga, J. M. Rouet, M. Fradkin, M. Breeuwer, and W. J. Niessen, *Segmentation of thrombus in abdominal aortic aneurysms from CTA with nonparametric statistical grey level appearance modeling*, IEEE Trans. Med. Imaging **24** (2005), no. 4, 477–485.

[46] S. Osher and R. Fedkiw, *Level Set Methods and Dynamic Implicit Surfaces*, Applied Mathematical Sciences, no. 153, Springer, New York, 2002.

[47] G. Peyré, *Matlab Toolboxes*, `http://www.ceremade.dauphine.fr/~peyre/download/`.

[48] E. Rouy, *Numerical approximation of viscosity solutions of first-order Hamilton-Jacobi equations with Neumann type boundary conditions*, Math. Models Methods Appl. Sci. **2** (1992), no. 3, 357–374.

[49] G. Sapiro, *Geometric Partial Differential Equations and Image Analysis*, Cambridge University Press, 2001.

[50] A. Seierstad and K. Sydsæter, *Optimal control theory with economic applications*, Advanced Textbooks in Economics V. 24, 1987.

[51] J. A. Sethian, *Level Set Methods and Fast Marching Methods (2nd edition)*, Cambridge University Press, 1999.

[52] S. Shindo, H. Matsumoto, K. Kubota, A. Kojima, M. Matsumoto, K. Satoh, and Y. Ozaki, *Is the Size of an Abdominal Aortic Aneurysm Associated with Coagulopathy?*, World J. Surg. **29** (2005), no. 7, 925–929.

[53] C. L. Siegel, R. H. Cohan, M. Korobkin, M. B. Alpern, D. L. Courneya, and R. A. Leder, *Abdominal Aortic Aneurysm Morphology: Ct Features in Patients with Ruptured and Nonruptured Aneurysms*, AJR Am. J. Roentgenol. **163** (1994), 1123–1129.

[54] A. K. Skiba, *Optimal growth with a convex-concave production function*, Econometrica **46** (1978), no. 3, 527–539.

[55] M. Sonka, F. Zhao, H. Zhang, A. Wahle, A. Stolpen, and T. Scholz, *Early Detection of Aortic Aneurysm Risk from 4-D MR Image Data.*, Computers in Cardiology 2006, Valencia, IEEE Press **33** (2006), 69–72.

[56] L. Speelman, A. Bohra, E. M. H. Bosboom, G. W. H. Schurink, F. N. van de Vosse, M. S. Makaroun, and D. A. Vorp, *Effects of Wall Calcifications in Patient-Specific Wall Stress Analyses of Abdominal Aortic Aneurysms*, J. Biomech. Eng. **129** (2007), 1–5.

[57] J. Stoer and R. Bulirsch, *Introduction to Numerical Analysis (3rd edition)*, New York: Springer-Verlag, 2002.

[58] M. Subasic, S. Loncaric, and E. Sorantin, *3-D image analysis of abdominal aortic aneurysm*, Proc. SPIE Med. Imag. **4684** (2002), 1681–1689.

[59] B. Sumengen, *A Matlab toolbox implementing Level Set Methods*, `http://barissumengen.com/level_set_methods/index.html`.

[60] R. C. Tam, C. G. Healey, B. Flak, and P. Cahoon, *Volume rendering of abdominal aortic aneurysms*, Proceedings IEEE Visualization '97 (1997), 136–145.

[61] F. O. O. Wagener, *Skiba points and heteroclinic bifurcations, with applications to the shallow lake system*, J. Econom. Dynam. Control **27** (2003), no. 9, 1533–1561.

[62] H. Zhang, H. Shen, and D. Huichuan, *An Automatic and Robust Algorithm for Segmentation of Three-dimensional Medical Images*, PDCAT 2005, 1044–1048.

[63] F. Zhuge, G. D. Rubin, S. Sun, and S. Napel, *An abdominal aortic aneurysm segmentation method: level set with region and statistical information*, Med. Phys. **33** (2006), no. 5, 1440–53.

[64] C. Zohios, G. Kossioris, and Y. Papaharilaou, *Geometrical methods for level set based abdominal aortic aneurysm thrombus and outer wall 2D image segmentation exploiting the presence of calcifications*, preprint (2010).